

The Pennsylvania State University
The Graduate School
Department of Astronomy and Astrophysics

DIGGING FOR SUBSTELLAR OBJECTS
IN THE STELLAR GRAVEYARD

A Thesis in
Astronomy and Astrophysics

by

John H. Debes, IV

© 2005 John H. Debes, IV

Submitted in Partial Fulfillment
of the Requirements
for the Degree of

Doctor of Philosophy

August 2005

We approve* the thesis of John H. Debes, IV.

Steinn Sigurdsson
Associate Professor of Astronomy and Astrophysics
Thesis Adviser
Co-Chair of Committee

Michael Eracleous
Associate Professor of Astronomy and Astrophysics
Co-Chair of Committee

James Kasting
Professor of Geosciences

Alexander Wolszczan
Evan Pugh Professor of Astronomy and Astrophysics

Lawrence Ramsey
Professor of Astronomy and Astrophysics
Head of the Department of Astronomy and Astrophysics

*Signatures are on file in the Graduate School

Abstract

White dwarfs, the endpoint of stellar evolution for stars with mass $< 8 M_{\odot}$, possess several attributes favorable for studying planet and brown dwarf formation around stars with primordial masses $> 1 M_{\odot}$. This thesis explores the consequences of post-main-sequence evolution on the dynamics of a planetary system and the observational signatures that arise from such evolution. These signatures are then specifically tested with a direct imaging survey of nearby white dwarfs. Finally, new techniques for high contrast imaging are discussed and placed in the context of further searches for planets and brown dwarfs in the stellar graveyard.

While planets closer than ~ 5 AU will most likely not survive the post-main sequence evolution of its parent star, any planet with semimajor axis > 5 AU will survive, and its semimajor axis will increase as the central star loses mass. The stability of adjacent orbits to mutual planet-planet perturbations depends on the ratio of the planet mass to the central star's mass, and I demonstrate that some planets in previously stable orbits around a star undergoing mass loss will become unstable. I show that when mass loss is slow, systems of two planets that are marginally stable can become unstable to close encounters with each other, while for three planets the timescale for close encounters decreases significantly with increasing mass ratio. Close encounters can lead to collisions of planets and new orbits that perturb surviving planetesimals into white dwarf grazing orbits. Perturbed planetesimals can create pollution of the white dwarf's surface and circumstellar dust disks which can be observational signatures of planetary systems

If pollution of a white dwarf's atmosphere is caused by relic planetary systems, any white dwarf with photospheric absorption due to metals can be searched for substellar companions. Hydrogen white dwarfs with metal absorption, so called DAZ white dwarfs, are hard to explain by simple ISM accretion, and present an opportunity to test the observational signatures of unstable planetary systems. Additionally, field white dwarfs can be searched for substellar companions as well. I conducted a Hubble Space Telescope (HST) and Canada France Hawaii Telescope survey of nearby white dwarfs for substellar objects. A total of 8 DAZ white dwarfs and a total of 12 field dwarfs with distances of < 50 pc had high contrast and high spatial resolution images taken with a combination of ground based and space based observations to search for candidate substellar objects at separations $\lesssim 10''$ away. Limits to unresolved companions are derived through analysis of 2MASS photometry of the white dwarfs compared to expected fluxes based on the WDs effective temperature, distance, and gravity. From my survey I find several candidate companions, which have been or will be followed up with second epoch observations. I find that my observations are sensitive to planetary companions around some targets with $M \gtrsim 6 M_{Jup}$, and sensitive to companions with $M > 18 M_{Jup}$ for all but two of my targets. The lack of significant near infrared excesses for my targets limits any kind of unresolved companions present to be substellar. In light of these results I make several comments on the possibility of determining the origin of metals in the atmospheres of white dwarfs and the frequency of substellar objects in orbit around intermediate mass stars.

The search for planetary companions to stars requires further development of high contrast imaging techniques. This thesis studies Gaussian aperture pupil masks (GAPMs) which in theory can achieve the contrast requisite for directly imaging an extrasolar planet around a nearby solar type star. I outline the process of designing, fabricating, and testing a GAPM for use on current telescopes and specifically the Penn State near-IR Imager and Spectrograph (PIRIS) at the Mt. Wilson 100'' telescope. I find that observations with a prototype are quite successful, achieving a contrast similar to a traditional Lyot coronagraph without blocking any light from a central object and useful for finding faint companions to nearby young solar analogues. In the lab I can reproduce the expected PSF reasonably well and with a single aperture design which achieves $\sim 4 \times 10^{-5}$ contrast at $10\lambda/D$. I find that small inaccuracies in the mask fabrication process and insufficient correction of the atmosphere contribute the most degradation to contrast at these levels. Additionally I present the first laboratory experiments using a notch-filter mask, a coronagraphic image mask that can produce infinite dynamic range in an ideal Lyot coronagraph according to scalar diffraction theory. I fabricated the first notch-filter mask prototype with $0.25 \mu\text{m}$ precision using an e-beam lithography machine. My initial optical tests show that the prototype masks generate contrast levels of 10^{-5} at $3\lambda/D$ and 10^{-6} at $\sim 8\lambda/D$, with a throughput of 27%. I speculate on the “as-is” performance of such a mask in the Hubble Space Telescope and for white dwarf targets.

Table of Contents

List of Tables	vii
List of Figures	viii
Acknowledgments	xii
Chapter 1. Introduction	1
1.1 The Dynamical Evolution of Planetary Systems During Post-Main Sequence Evolution	4
1.2 White Dwarfs as Targets for Planet Searches	5
1.3 Developing New Imaging Techniques for the Future	7
Chapter 2. The Dynamical Evolution of Planetary Systems Around White Dwarfs	9
2.1 Introduction	10
2.2 Stability for Planetary Systems Under Mass Evolution	11
2.2.1 Two Planet Systems	11
2.2.2 Multiple Planet Systems	12
2.2.3 When is Mass Evolution Adiabatic?	13
2.3 Numerical Methods	14
2.4 Results	16
2.4.1 Two Planets	16
2.4.2 Multiple Planets	16
2.4.3 Observational Implications	19
2.4.3.1 Cometary dynamics	24
2.5 Discussion	29
Chapter 3. Limits to Substellar Companions Around DAZs	31
3.1 Introduction	32
3.2 Observations	32
3.2.1 Observational Strategy	32
3.3 Data Analysis	36
3.4 Candidate Companions and Extragalactic Objects	37
3.4.1 WD 2326+049	38
3.4.1.1 A Candidate Planetary Companion	38
3.4.2 WD 0208+395	40
3.4.3 WD 0245+541	43
3.4.4 WD 1620-391	43
3.5 Limits to Companions	46
3.5.1 Limits from 2MASS Photometry	48
3.5.2 Imaging	52
3.5.3 Limits from Pulsational Studies	56

Chapter 4. Limits to Substellar Objects Around Nearby White Dwarfs	60
4.1 Introduction	61
4.2 Observations	61
4.3 Data Analysis	62
4.4 Candidate Companions and Background Objects	65
4.4.1 WD 2341+321	65
4.4.2 WD 1121+216	66
4.4.3 WD 1213+528	66
4.4.4 WD 1953-011	67
4.4.5 WD 2140+207	67
4.4.6 WD 0208+396	68
4.5 Limits to Companions	69
4.5.1 Imaging	69
4.5.2 Near-IR Photometry	71
Chapter 5. Future Directions for High Contrast Imaging	73
5.1 Gaussian Aperture Pupil Masks	74
5.1.1 Introduction	74
5.1.2 Designing a GAPM for current telescopes	78
5.1.2.1 Multiple Apertures	78
5.1.2.2 Minimizing Support Structure	79
5.1.2.3 Final Design of the Prototype	80
5.1.3 Fabricating a GAPM	80
5.1.4 Testing the Prototype	83
5.1.4.1 First Light and Lab tests	83
5.1.4.2 Modeling the Degradation in Contrast	85
5.1.4.3 Lessons for AO observers	85
5.2 Notch-Filter Masks	87
5.2.1 Introduction	87
5.2.2 Mask Design and Fabrication	90
5.2.3 Modeling the Performance of the Mask	91
5.2.4 Experiments and Results	92
Chapter 6. Conclusions	97
6.1 The Scenario of Post Main Sequence Evolution for Planetary Systems	98
6.2 The Prospects for Finding Cool Companions in the Stellar Graveyard	98
6.2.1 DAZ White Dwarfs	99
6.2.2 Field White Dwarfs	102
6.2.3 Upper Limits to the Presence of Substellar Objects for the Whole Sample	102
6.3 Future Technologies for High Contrast Imaging	103
Bibliography	106

List of Tables

2.1	Coefficients for Equation 2.2	19
3.1	Table of Target White Dwarfs	34
3.2	Table of HST Observations	35
3.3	Table of Extragalactic Objects	38
3.4	Photometry and Significance of Detections	40
3.5	Candidates around WD1620-391	46
3.6	2MASS Photometry of PG WDs	49
3.7	Magnitudes and Spectral Types of Excess Candidates	51
3.8	Comparison of Predicted vs. 2MASS Photometry	51
3.9	Upper limits to Companions	56
4.1	List of WD Targets	61
4.2	Observations	63
4.3	Extragalactic Objects	65
4.4	Sensitivities	72
5.1	Table of Design Parameters	80
5.2	Experimental Fluxes and Peak Count Rates	96

List of Figures

2.1	Results of several simulations of instability after mass loss. The dashed line corresponds to the original stability criterion of Equation 2.1. The solid line corresponds to the criterion with $\mu = 2\mu_i$	15
2.2	Close-up of Figure 2.1 in the range of $10^{-3.5}$ - 10^{-3} . Open diamonds represent simulations that did not suffer any close approaches over 10^5 orbits. Filled diamonds represent simulations that did suffer a close approach, while the solid curve represents the predicted Δ_c with mass loss. The horizontal solid line shows the relative separation that corresponds to the 3:2 resonance. A region of stability where instability is expected surrounds this resonance.	17
2.3	Orbits around the 3:2 resonance for two planet stability. The top and bottom lines correspond to orbits that end in a close approach while the middle line shows an orbit that was stable over the length of the simulations.	18
2.4	Comparison of the timescale to the first close approach for a system of three $\mu=10^{-7}$ planets with and without mass loss, where asterisks represent static masses and open diamonds represent the presence of mass loss. The top line is given by least-squares fitting a line of slope b and intercept c for no mass loss. The bottom line is given by Equation 2.5.	20
2.5	The $\mu = 10^{-5}$ case, symbols the same as in Figure 2.4. The slope and intercept of the top line was derived by fitting the numerical simulations without mass loss. The slope of the bottom line is the predicted change due to mass loss.	21
2.6	The $\mu=10^{-3}$ case, symbols the same as in Figure 2.4. The arrows indicate separations at which my simulations remained stable for 10^7 orbits. The slope and intercept of the top line was derived by fitting the numerical simulations without mass loss. The presence of strong resonances is particularly noticeable as enhanced stability around $\delta=5.2$ for the mass loss case, which corresponds to the 2:1 resonance.	22
2.7	Comparison of Δ_c with and without mass loss as a function of the central star's original mass. The right panel shows the fractional change of Δ_c when mass loss occurs. For both panels the fractional change in mass is calculated using the M_i - M_f relation of Weidemann (2000).	28
3.1	Image of WD 2326+049 in the F160W filter before (left) and after (right) PSF subtraction. The right panel has been smoothed with a Gaussian filter to show a candidate companion (C1) and two extragalactic objects (DSW 3,4).	33

3.2	(left) Discovery image of a candidate planetary companion in the HST F160W filter. (right) Second epoch image with Gemini, along with the predicted positions of co-moving (square) and non co-moving (circle) objects. The object is non co-moving and therefore in the background.	39
3.3	Field of WD 0208+395 with its candidates. Candidates are circled, and the WD is masked to hide the systematic subtraction errors. A galaxy is detected in the lower right of the image.	41
3.4	Field of WD 0245+541 with its candidates circled.	42
3.5	Field of WD 1620-391 with its candidates. Each candidate that is circled is within $4''$ and has colors, consistent within the photometric errors, for a candidate planetary object.	44
3.6	Distribution of point sources as a function of distance around the white dwarf WD 1620-391.	45
3.7	Color magnitude diagram of sources near the white dwarf WD 1620-391. Overplotted is an isochrone of 1 Gyr substellar models from Burrows et al. (2003) convolved with HST filters at 12 pc. Thick crosses are sources $<4''$ away.	47
3.8	Sample sensitivity test image. WD 2326+049 has an implanted artificial companion at a separation of $1.9''$ and a PA of 204° with respect to North in the image. North is rotated 43° counterclockwise from up in the image. The implant has an F160W magnitude of 22.2 with a S/N of 9 for a 4 pixel diameter photometric aperture.	53
3.9	The final azimuthally averaged 5σ sensitivity curve of my HST and Gemini images. At separations $<1''$, the Gemini PSF still had significant flux. To ensure that my sensitivity reflected actual detectability, I used a 10σ limit in the inner regions.	54
3.10	Isochrones of substellar objects with a total age of between 1 and 3 Gyr in NICMOS filters. Small numbers correspond to masses in units of M_{Jup} . I used the spectral models of Burrows et al. (2003) and convolved them with the NICMOS filters.	55
3.11	Sensitivity at 5σ to point sources in F110W around WD 0208+395. The WD's F110W magnitude is ~ 13.8 , giving a contrast of 10 magnitudes at $1''$. Overplotted is the magnitude of a $10 M_{Jup}$ planet 3.2 Gyr old at the distance of WD 0208+395 from the models of Burrows et al. (2003).	57
3.12	Combined limits to substellar objects around WD 2326+049 from a combination of 2MASS photometry, pulsation studies, and my high contrast imaging. The solid and dashed lines show the limits to the age of WD 2326+049 and the triangle shows the expected minimum mass of a companion tentatively discovered by pulsational studies.	58
4.1	Two azimuthally averaged PSFs for WD 1953-011, before subtraction (solid line) and after subtraction (dashed line). This WD had a contemporaneous PSF reference in the field which was used for subtraction purposes.	64

4.2	Candidate companion (C1) at a separation of $2.25''$. If this object is physically associated it would be an $11M_{Jup}$ object.	66
4.3	These images show extended emission discovered around WD 1121+216 before (left panel) and after (right panel) PSF subtraction. Second epoch POSS images show that it is a background galaxy. The scale bar in the left panel represents $2''$	67
4.4	Images of a nearby background star near WD 1953-011 that show a companion with $\Delta H=7.6$ with a separation of $1.08''$ before (left panel) and after (right panel) PSF subtraction. This detection demonstrates the study's sensitivity to point sources close to my targets.	68
4.5	A comparison between the HST and CFHT fields for WD 0208+395. The HST field is on the left and the CFHT field is on the right. The images are about $9''$ long on a side and shows one of the candidates due South of WD 0208+396 which is masked.	69
4.6	Sample 5σ sensitivity curve of WD 2246+223. Overplotted is the H magnitude of an $8 M_{Jup}$ companion at the age and distance of the target.	70
5.1	The resulting monochromatic diffraction pattern for a single aperture GAPM with $a = 1.$ and $\alpha = 2.5.$ The image is logarithmically scaled.	75
5.2	The top half of the fabricated mask used for observing on the Mt. Wilson telescope at 5x optical magnification. The twelve apertures allow $\sim 25\%$ throughput, while avoiding the support structure of the telescope. This picture shows the imperfections in the fabrication process.	81
5.3	Comparison of the theoretical J band diffraction pattern (right) compared with lab results with PIRIS (left). Both are on the same logarithmic scale. The model used included the imperfect shape of the mask that was fabricated and the model was integrated over the transmission function of a typical J filter.	82
5.4	Azimuthally averaged PSF profiles for the GAPM multiaperture design tested at Mt. Wilson, along with results of a lab test in the J band and two different models. Model 1 represents a model with perfect apertures, while Model 2 is the simulated results based on the actual shape of the apertures.	84
5.5	Azimuthally averaged PSF of the single aperture design in the J band. I achieved 4×10^{-5} contrast at $10\lambda/D$. Truncation of the mask during fabrication is the main degradation of contrast with what would be theoretically possible.	86
5.6	A comparison between the J band PSF and a model based on the truncation of the Gaussian contour's wings described in Equation 5.16. For the model I used $\beta=13$ and the parameters listed in Table 5.1 for the Mt. Wilson design. Both the model and the lab data were azimuthally averaged for 20° about the high contrast axis.	88
5.7	Optical microscope images of the final mask design.	89

5.8	A model of the light distribution in the pupil plane prior to a Lyot stop of a notch-filter mask design with an $\epsilon=0.46$, at the working wavelength of $0.633 \mu\text{m}$	91
5.9	A comparison between pupil images of the testbed with no mask (left) and with a mask centered (right).	92
5.10	(top) 10 second image of the laser point source without the mask in place. (bottom) Image with same intensity stretch with the mask in place. The peak pixel value of the bottom image is 2.8×10^5 ADU.	94
5.11	Comparison between the unblocked point source, the notch-filter mask, and mask transmissivity. Each image was azimuthally averaged to within 20° of the notch filter mask axis.	95

Acknowledgments

In the Hitchhiker's Guide to the Galaxy books, the character Arthur Dent trips over a rock and learns to fly by forgetting to hit the ground. Life itself seems to be like that—if you forget about all the reasons you should fail at something hard, it becomes remarkably possible to achieve what you hope. I want to take this opportunity to thank all those people who helped me forget the ground, thus allowing me to fly. Specifically, I want to thank my adviser Steinn Sigurdsson, without whom this could not be possible. He provided an environment where I could come in with crazy ideas and he would tell me which ones sounded good and added some crazy ideas of his own. His instincts for finding fun, unique, and important science are unparalleled. I would also like to thank Jian Ge for providing me excellent opportunities to do experimental and observational work, the results of which make two chapters in this thesis possible. My gratitude goes especially to my wife, Alexandra Surcel, whose tireless support and love dwarf whatever fame or fortune I may accrue in this life. The origin of all my endeavors can be traced to the values and attitudes of my parents, who instilled in me a desire for knowledge, and the work ethic to achieve it. I would like to take time to thank my committee as well, for their helpful suggestions for making this the best thesis it could be. I want to thank many members, past and present, of the Department of Astronomy & Astrophysics who provide a place that feels like home—when you are in such a place you do not need to spend time worrying about anything but being your best. I'd especially like to thank Karen Lewis, Michele Stark, Jie Ding, Avi Mandell, Michael Sipior, Sarah Gallagher, and Jon Feldmeier, who have gone the extra distance in various ways to support and teach me.

There have been hundreds, if not thousands of people who have come in contact with me throughout my life, some with large impact and some with small. Yet in every instance, they have imperceptibly changed my course, not unlike a star that comes into contact with a myriad of others in a galaxy. My path is unique, sometime solitary, but always ever helped by others to form a larger, more beautiful pattern. I wouldn't want it any other way.

Always two there are, no more, no less: a master and an apprentice.

–Master Yoda

Keep away from those who try to belittle your ambitions. Small people always do that, but the really great make you believe that you too can become great.

–Mark Twain

Chapter 1

Introduction

The last ten years have shown a surge of new discoveries about objects of substellar mass. Radial velocity surveys of main sequence K-F stars have found few brown dwarf companions at separations of <3 AU, but a profusion of planetary mass companions (Marcy & Butler 2000). Large all-sky surveys, such as 2MASS and SDSS have found large numbers of free floating brown dwarfs (Burgasser et al. 2003; Hawley et al. 2002). Low mass substellar objects down to planetary mass have been discovered in young clusters such as σ Orionis, although it is a controversial result (Lada & Lada 2003; Burgasser et al. 2004, and references therein).

At the same time, imaging surveys of nearby main sequence stars have found several substellar companions thanks to high contrast imaging (e.g. Forveille et al. 2004). Intermediate mass stars with masses between $1.5\text{-}8 M_{\odot}$ are a population of stars which still has little data. There are many reasons for the dearth of information around intermediate mass stars. Firstly, it is partly due to the fact that the bulk of the search for planetary systems focuses on Solar System analogues. Additionally, there are technical reasons which limit the opportunity to search for planets and brown dwarfs around main sequence F-B stars. Radial velocity surveys rely on a large number of narrow absorption lines in the stellar spectrum to achieve high precision velocity measurements (Delfosse et al. 1998; Griffin et al. 2000). As the effective temperature of a star increases, metal line strengths decrease and there are fewer lines for measurement. Radial velocity surveys are less sensitive to planets around more massive stars since the star has a smaller reflex motion. Radial velocity surveys of G giant stars probe higher mass stars, with only one planetary companion published to date (Sato et al. 2003). As a star's mass increases, its luminosity increases as well, making high contrast imaging more limited in its effectiveness if one is looking for the thermal emission from a companion rather than its reflected light. Reflected light is most useful within a few AU of a star and is negligible at larger distances (Burrows et al. 2004). For example, high contrast imaging can achieve $\Delta H \sim 10$ at $1''$ on the NICMOS coronagraph with PSF subtraction, allowing $45 M_{Jup}$ mass companions to be detected around a 1 Gyr solar mass star. For an A star with a mass of $2 M_{\odot}$ at 1 Gyr, a $90 M_{Jup}$ companion can be detected. Finally, more massive stars are rarer in local space, forcing observations of young star forming regions at larger distances.

Recent images of several young HAe/Be stars with circumstellar disks such as HD 141569, HR 4796A, and AB Aurigae, motivate a search for planets around higher mass stars (Weinberger et al. 1999; Jayawardhana et al. 1998; Grady et al. 1999). Sub-mm observations of warped and clumpy disks, such as Vega and Formalhut, show that planet formation may be vigorous for higher mass central stars (Holland et al. 1998). What is still unclear is how planet formation efficiency varies with stellar mass and whether the brown dwarf desert is present over the same orbital separations for higher mass stars.

While the discoveries of 145 or so planets by radial velocity surveys have told us much about planet formation, the detection of planets in orbit around post main sequence objects challenge the basic understanding of planet formation. For example, the first extrasolar planets ever discovered were around a pulsar (Wolszczan & Frail 1992). The oldest Jovian planet discovered in the M4 globular cluster in orbit around a white dwarf demonstrates that relatively Solar System-like Jovian planet formation can occur in metal poor systems, contrary to the indication given by radial velocity surveys,

which find planet formation more likely to occur in metal enriched systems (Sigurdsson et al. 2003).

The next step in these endeavors for learning more about substellar objects is to directly image them in orbit around host stars. A host of technological challenges faces such work. Firstly, any companion would not only have to be resolved from the host star, but detected in the sidelobes of the star's point spread function (PSF) with a sufficient signal-to-noise ratio. The PSF of an object is dependent entirely on the shape of the aperture; for a circular aperture the PSF's intensity declines as $(\theta/\theta_o)^{-3}$, where $\theta_o \sim \lambda/D$. For the intensity of the sidelobe to equal the relative intensity of the planetary companion to the host star, the PSF's amplitude must be at a level of $\sim 10^{-9}$ compared to the peak or $10^3 \lambda/D$. At the distance of 51 Peg, this corresponds to the requirement of a telescope with a 270 km diameter, assuming a search wavelength of $0.5 \mu\text{m}$. If instead one wished to detect any companions at 5 AU, more in keeping with planets like Jupiter, the requirement would merely be 1.6 km. With 30 m telescopes as the next generation of large ground based telescopes and a 6-8 m space telescope, this approach is unlikely to garner a direct detection of an extrasolar planet in the near future.

Given these monumental technological difficulties, other approaches must be developed that can be achieved in a relatively short time with existing telescopes. There are many options which break down into three categories:

- Indirectly detect the presence of planets without imaging.
- Suppress the sidelobes of the host star's PSF to allow imaging.
- Search for host stars/objects where the contrast requirements are less stringent.

This thesis explores a combination of all three of these approaches to determine a population of objects that afford less stringent contrast requirements for directly detecting extrasolar planetary objects around stars more massive than the Sun. Studying the dynamical effects of post main sequence evolution on planetary systems aids in the identification of a population of white dwarfs that may show markers of planetary systems.

White dwarfs represent an intriguing population of stars to observe in order to discover extrasolar planets and brown dwarfs. Given their intrinsic dimness, they allow high contrast searches to probe interesting orbital separations (Burleigh et al. 2002). In addition, their higher effective temperature allows searches for unresolved excesses at larger wavelengths (Ignace 2001). A study of WDs probes a large range of initial stellar mass. Several studies have quantified the initial-to-final mass relationship of stars that evolve into white dwarfs (Weidemann 2000, and references therein). These calculations are based both on models of post-main-sequence stellar core evolution and observations of stellar clusters. This approach is limited by the small number of target stars to study, which introduces uncertainty to the calculations. However, recent cluster studies of white dwarfs have doubled the number of data points and show that between 2.8 and $3.4 M_{\odot}$ the relationships put forth are accurate to within $1-2 M_{\odot}$ (Kalirai et al. 2005). Finally, an imaging search of WDs complements radial velocity and transit searches that are biased towards close companions. High spatial resolution and high contrast imaging in

the near infrared with the NICMOS camera on HST allows the best chance for detecting faint cool companions to nearby white dwarfs. Planetary mass objects that are less than 3 Gyr can be observed in the near-IR, specifically in the F110W (\sim J) and F160W (\sim H) filters. For example, a 3 Gyr old $10 M_{Jup}$ planet can be observed out to 20 pc with an HST observation of \sim 1200s.

White dwarfs that may show markers of planet formation, as well as other nearby field white dwarfs, are studied with an intensive direct imaging survey of 20 targets. In addition work has been done to create novel ways of suppressing the sidelobes of the host star PSF through the use of shaped apertures and coronagraphic techniques in order to achieve high contrast for future surveys.

1.1 The Dynamical Evolution of Planetary Systems During Post-Main Sequence Evolution

Searching a subset of white dwarfs that harbor markers for substellar objects can maximize the return of a survey. White dwarfs are generally classified by their atmospheric composition, which typically is either hydrogen or helium and most easily identified through constituent lines of either element in the WD atmosphere. Nearby hydrogen white dwarfs with metal line absorption are called DAZs and may be a population of WDS that have substellar companions. Three hypotheses have been put forth to explain the presence of DAZs—interstellar matter (ISM) accretion (Dupuis et al. 1992, 1993a,b), unseen companion wind accretion (Zuckerman et al. 2003), and accretion of volatile poor planetesimals (Alcock et al. 1986; Debes & Sigurdsson 2002; Jura 2003).

ISM accretion has a wealth of problems in predicting many aspects of DAZs such as the large accretion rates required for some objects, or the distribution of these objects with respect to known clouds of dense material (Aannestad et al. 1993; Zuckerman & Reid 1998; Zuckerman et al. 2003). Their quick atmospheric settling times require them to be in close proximity with accretionary material.

One explanation is that DAZs should have unseen companions that place material onto the WD surface through winds. The explanation is based upon seven DAZs found to have close dM companions in a survey of 80 WDs (Zuckerman et al. 2003). In that same survey 24 more WDs were found to be DAZs that did not have any known companions. Zuckerman et al. (2003) did not discuss how they chose their targets and so it is unclear what biases may be present in the sample. The wind accretion scenario requires companions that are in extremely close orbit, bringing into question why these objects have yet to be discovered through transits or radial velocity surveys of compact objects, or through observable excesses in NIR flux. In most cases the reflex motion of the white dwarf from such objects would be easily detectable (Zuckerman & Becklin 1992). This explanation is unable to account for objects such as WD 2326+049 (G 29-38) which has an infrared excess due to a dust disk at roughly the tidal disruption radius (Graham et al. 1990; Patterson et al. 1991; Jura 2003).

The invocation of cometary or asteroidal material as a method of polluting WD atmospheres was developed early to explain the discovery of metal lines in the DAZ WD 0208+395 (G 74-7) (Alcock et al. 1986). However, the plausible rates predicted by these original studies could not explain the highest accretion rates inferred for some

objects and could not easily reproduce the distribution of DAZs based on their effective temperatures (Zuckerman et al. 2003). However, mixing length theory predicts a drop-off of observability for accretion as a function of effective temperature which may swamp out the earlier prediction of Alcock et al. (1986), (Althaus & Benvenuto 1998). This drop-off removes one of the major objections to this hypothesis, but the largest accretion rates are still hard to explain. The effect non-axisymmetric mass loss could have on the fraction of comet clouds lost by their hosts during post main sequence evolution is also unclear (Parriott & Alcock 1998). Cometary clouds are, by hypothesis, the result of planet formation, so the long term evolution of planetary systems and their interaction with these comet clouds needs to be investigated (Tremaine 1993).

The problems of the Alcock et al. (1986) model can be overcome by studying the stability of planetary systems during the evolution of the central star as it loses mass while leaving the main sequence and evolving into a white dwarf. Most planetary systems are stable on timescales comparable to their current age. During adiabatic mass loss, companions expand their orbits in a homologous way, increasing their orbital semi-major axes by a factor M_i/M_f (Jeans 1924).

Mass loss has implications for the well known Hill stability criterion against close approaches for two comparable mass planets. The stability criterion is roughly described as $\Delta_c = (a_1 - a_2)/a_1 = 3\mu^{1/3}$ where a is the semi-major axis, μ is the mass ratio of the planets to the host star and Δ_c represents the critical separation at which the two planets become unstable to close approaches (Hill 1886; Gladman 1993). The critical separation grows as the relative separation of the two planets stays the same, resulting in marginally stable systems being tipped over the edge of stability. This instability can lead to orbital rearrangements, the ejection of one planet, and collisions (Ford et al. 2001). These three events dramatically change the dynamical state of the planetary system, leading to a fraction of systems that perturb the surviving comet cloud and send a shower of comets into the inner system where they are tidally disrupted, cause dust disks, and slowly settle onto the WD surface. This modification of the comet impact model can explain the accretion rates needed for the highest abundances of Ca observed and the presence of infrared excesses around WDs (Debes & Sigurdsson 2002). Chapter 2 documents the theory and observational consequences of the evolution of a planetary system during post main sequence evolution.

1.2 White Dwarfs as Targets for Planet Searches

The advantages of using WDs to study low mass objects have been recognized in the past. Studies of the low mass end of the stellar initial mass function used near-IR excesses around WDs to look for low mass M dwarfs (Probst & Oconnell 1982). Other searches for companions to WDs turned up one substellar companion to GD 165 and several other M dwarf companions Zuckerman & Becklin (1987, 1992). These ideas have been extended to the present with larger surveys of hot WDs or by using the 2MASS database (Green et al. 2000; Wachter et al. 2003). The idea of detecting the presence of planets around white dwarfs through their excess was reported by Ignace (2001), while Chu et al. (2000) pointed out that Jovian planets in close orbit around WDs will have stimulated H α emission that could be detectable.

Direct imaging searches for planets or brown dwarfs in orbit around white dwarfs have been proposed recently (Burleigh et al. 2002; Debes & Sigurdsson 2002; Friedrich et al. 2005; Farihi et al. 2003). This is primarily a sensitivity issue—any light comes from the planet’s thermal emission. Reflected light or insolation from the white dwarf do not contribute significantly. Recent theoretical models of isolated extrasolar planets have provided observers with a better idea of what substellar objects are detectable, allowing accurate estimates of what is possible given current technology (Burrows et al. 2003; Baraffe et al. 2003).

Even in the realm of direct imaging several strategies are being implemented. Direct non-AO imaging of young white dwarfs using large telescopes allows well separated companions to be detected, down to $\sim 5\text{-}10 M_{Jup}$ (Burleigh et al. 2002). Several co-eval white dwarfs have been searched with NICMOS in the Pleiades open cluster, where the young age of the WDs is offset by the larger distance to the stars. A search for widely separated companions was done with the Steward Observatory to look for common proper motion pairs between $2\text{-}90''$ (Farihi et al. 2003). Given the frequency of planets discovered with radial velocity surveys, one would expect that at least 100 white dwarfs would need to be surveyed before viable candidate planets could be discovered. However, by searching for markers of planetary systems before searching the white dwarfs directly, the efficiency of a planet search is increased. In addition, having high contrast with AO or space-based observing in the near-IR allows more sensitive searches to be conducted closer to the host star.

One DAZ in particular is interesting. WD 2328+049 (ZZ Psc, G 29-38, GJ 895.2) is a nearby ($d=13.6$ pc) pulsating hydrogen WD with photospheric absorption lines due to metals such as Mg and Ca (van Alena et al. 2001; Koester et al. 1997), also known as a DAZ type WD. WD 2326+049 has a measured gravity $\log g= 8.15$ and a $T_{eff}=11820$ K, placing its cooling age at 0.6 Gyr (Liebert et al. 2004).

WD 2326+049 possesses an infrared excess, originally attributed to a companion substellar object (Zuckerman & Becklin 1987). However, further infrared studies including pulsational studies in the near-IR are more consistent with a circumstellar disk at $1 R_{\odot}$, with a blackbody temperature of ~ 1000 K (Tokunaga et al. 1988, 1990; Telesco et al. 1990; Graham et al. 1990). The origin of the disk is unclear, though it could be caused by a tidally disrupted asteroid or comet, potentially sent to the inner system by a planetary system that suffered chaotic evolution after post main sequence evolution (Debes & Sigurdsson 2002; Jura 2003).

Long-term pulsational studies of WD 2326+049 have allowed several of the more stable pulsation modes to be monitored for timing delays due to an unseen companion (Kleinman et al. 1994; Kleinman 1998). No conclusive detections of a companion have been reported. Speckle imaging of WD 2326+049 furthermore could not detect any unresolved companions, although IR slit scans of WD 2326+049 appeared to show an extension in the N-S direction on scales of $0.4''$ (Kuchner et al. 1998; Haas & Leinert 1990).

The biggest question that remains is the origin of the dust disk present, which pollutes the white dwarf’s atmosphere with metals. Planets in inner regions most likely will be engulfed by the AGB phase of the star, with larger planets possibly “recycled” into brown dwarf companions (Siess & Livio 1999a,b). Remnant asteroids and comets

potentially could survive at distances where they would not be ablated from the AGB phase (Stern et al. 1990). However, if the primary star has asymmetric mass loss, objects such as comets can easily be lost from the system where the orbital timescale equals the timescale for mass loss (Parriott & Alcock 1998). Planets or brown dwarfs in orbits $\gtrsim 5$ AU will avoid engulfment and survive post main sequence evolution (Rasio et al. 1996; Duncan & Lissauer 1998). Massive white dwarfs may also contain planets that are formed from WD-WD mergers, allowing unseen companions in close orbits (Livio et al. 1992). I study this WD as part of a larger survey of nearby white dwarfs for planets and brown dwarfs.

Only ~ 30 DAZs are currently known, so a wider survey of nearby, young WDs is desirable as well. A wider survey requires additional observations from the ground. To achieve the highest contrast adaptive optics (AO) systems are required. These systems can have difficulties correcting the atmospheric wavefront for very dim objects, so any survey of WDs requires AO systems that can successfully correct the atmosphere for objects with $V < 15$. Curvature wavefront AO systems such as the PUEO system on the Canada France Hawaii Telescope (CFHT) and the Shack-Hartmann Altair AO system on Gemini can be used for high contrast imaging of WDs Rigaut et al. (1998); Hutchings et al. (2004) Chapters 3 and 4 describe the search I conducted for substellar objects both from space with the Hubble Space Telescope (HST) and from the ground.

1.3 Developing New Imaging Techniques for the Future

Currently the best way to diminish the Airy pattern of a telescope is to use a coronagraph by combining a stop in the focal plane that rejects a majority of the central bright object’s light and a Lyot stop in the pupil plane that rejects residual light diffracted to the edge (Lyot 1939). Several recent ideas explore the use of alternative “apodized” apertures for high contrast imaging in the optical or near-infrared (Nisenson & Papaliolios 2001; Spergel 2001; Ge 2002; Kuchner & Spergel 2003a). These designs revisit concepts first experimented with in the field of optics (Jacquinot & Roizen-Dossier 1964). In this case the light from the star is not blocked out, but the sidelobes of the PSF are diminished, allowing higher contrast to be achieved at closer separations.

Other designs use image-plane masks to absorb on-axis light and diffract it away (Malbet 1996; Sivaramakrishnan et al. 2001; Kuchner & Traub 2002). Image masks offer the advantages that they explicitly remove starlight from the beam and that they can provide high contrast at small angles from the optical axis, given sufficient control over low-spatial frequency modes.

Scattered light, wavefront errors, and mask construction errors can all degrade the contrast of a coronagraph. For example, for any coronagraphic image mask, mid-spatial frequency intensity errors near the center of the mask must be $\lesssim 10^{-9}$ (Kuchner & Traub 2002). Some of these errors can be controlled using active optics, but these corrections will apply only over a limited range of wavelengths.

In anticipation of developing new techniques for high contrast imaging around nearby white dwarfs or for future terrestrial planet searches, this thesis explores two different techniques for gaining high contrast. I look at them critically in the context of planet searches around white dwarfs. In Chapter 5 the properties and design

considerations for Gaussian aperture pupil masks (GAPMs) and notch-filter masks are investigated.

Chapter 2

The Dynamical Evolution of Planetary Systems Around White Dwarfs

The work in this chapter appeared in:

Debes, J. H. & Sigurdsson, S. 2002, ApJ, 572, 556

2.1 Introduction

The discovery of more than 145 planets, and counting, around solar-type stars suggests that successful planet formation is quite common. The wealth of systems vastly different than the Solar System leads one to conclude that many aspects of planetary system formation and dynamical evolution have yet to be fully explored. One particularly interesting area is the long-term evolution of planetary systems specifically in the presence of post-main-sequence evolution of the central star. Observations of planets around post-main-sequence stars may provide additional information about the formation and evolution of planetary systems around main-sequence stars and can inform us about the long-term future of the solar system.

While planets at distances similar to the outer planets in the solar system will persist through post-main-sequence evolution (Duncan & Lissauer 1998), it is unlikely that close Jovian companions to such stars survive. As the star evolves it expands, engulfing anything up to ~ 1 AU (Sackmann et al. 1993; Siess & Livio 1999a,b). Outwards of an AU, up to ~ 5 AU a planet's orbit will decay through tidal transfer of angular momentum and become consumed within the envelope of the star (Rasio et al. 1996). Anything with less mass than a brown dwarf will not survive in the stellar envelope (Livio & Soker 1984; Soker et al. 1984).

Planets may still be observed in close orbits around white dwarfs if their orbits are significantly changed by some process that occurs after the AGB phase. If planets become unstable to close approaches with each other, their interaction would result in a planet close to the central star. Such scenarios have been proposed for the formation of close Jovian planets around main sequence stars (Rasio & Ford 1996; Weidenschilling & Marzari 1996; Lin & Ida 1997). The results of close encounters between two Jovian planets have been studied in detail, with three possible outcomes: the two planets collide leaving a large planet, one planet is ejected, or both planets remain in a new stable configuration (Ford, Havlickova, & Rasio 2001). For planets starting out with semi-major axes > 5 AU, $\sim 8\%$ of unstable pairs will collide, the rest will not. Of the systems which avoid collision, roughly 40% will settle into a configuration with a planet in a significantly closer and more eccentric orbit than in the initial system. Thus the onset of instability after post-main-sequence mass loss may create white dwarf systems with planets at orbital radii scoured clear of the original inner planets during the star's giant phase.

Simulating the Uranian satellite system, Duncan & Lissauer (1997) found that Hill stable systems can become unstable with an increasing mass ratio for satellites orbiting a central massive object. This important work led to one of the few systematic studies of the post-main-sequence evolution of planetary systems dynamically similar to the Solar System (Duncan & Lissauer 1998). They also found that as an increasing fraction of mass was lost from the central star, the time to unstable close approaches for the planets followed a power-law relationship depending on the ratio of planetary mass to stellar mass. At the level of individual planetary orbits, resonances may also play an important role in an adiabatically changing system, enhancing stability or creating instability. In this Chapter I generalize the specific results of Duncan & Lissauer (1998) to a range

of system parameters applicable to a wider range of situations, such as those like the extrasolar multi-planet systems recently discovered.

Most likely, extrasolar planetary systems also possess Oort cloud analogues as a direct result of planet formation (Oort 1950; Weissman 1999). The orbital time scales of outer Oort cloud comets are comparable to the more rapid late stages of post-main-sequence evolution, and the mass loss of a star is not adiabatic in the context of AGB evolution. If the mass loss is fairly symmetric, many of these comets survive the evolution and can later provide a steady flow of comets which impact the white dwarf directly, or break up due to tidal strain and populate the inner system with dust, causing photospheric metal contamination (Stern et al. 1990; Alcock et al. 1986; Parriott & Alcock 1998). However, if the planet systems become unstable to close approaches after the AGB phase, the entire system becomes dynamically young and new collisions and encounters can occur between surviving comets and planets. Many scenarios lead to a period of enhanced “late bombardment” as cometary orbits are perturbed and the flow of comets into the inner system is enhanced. In this Chapter I will investigate whether this mechanism can explain the observed IR excess around the white dwarf WD 2326+049, attributed to a disk of dust whose extent is comparable to the tidal radius of the white dwarf (Graham et al. 1990; Zuckerman & Becklin 1987; Jura 2003). Graham et al. (1990) estimated that approximately 10^{15} g/yr of metal rich material would rain upon the white dwarf, if the infrared emission is due to a dust cloud at about half solar radius, requiring a steady and high rate of replenishment of the putative dust. My model may resolve the problem of those DAZ white dwarfs which cannot be easily explained by either isolated cometary impacts or ISM accretion (Zuckerman & Reid 1998; Zuckerman et al. 2003).

I will show that the mass lost from a central star is sufficient to destabilize systems of two or more planets in previously stable orbits and cause them to suffer close approaches, producing several observable signatures. In Section 2.2 I will develop the stability of planetary systems against close encounters in the presence of adiabatic mass loss, describe my numerical methods for testing my analytical estimates in Section 2.3, present my results and discuss relevant observational signatures in Section 2.4, and discuss the implications of these findings in Section 2.5

2.2 Stability for Planetary Systems Under Mass Evolution

2.2.1 Two Planet Systems

The stability of two planets against close approaches depends primarily on the masses of the planets relative to the central star and the separation of the two orbits. This separation is measured as $\Delta = (a_2 - a_1)/a_1$ where a_1 and a_2 are the inner and outer semi-major axes respectively. A critical Hill separation, Δ_c is then the minimum separation between two planets which ensures a lack of close approaches over all time (Hill 1886). A full treatment of the Hill stability of two planets in the case of static masses can be found in Gladman (1993). Several approximations can be made that simplify the full treatment, such as equal planetary masses and small eccentricities. The

criterion is then given by:

$$\Delta_c \simeq \sqrt{\frac{8}{3} (e_1^2 + e_2^2) + 9\mu^{2/3}} \quad (2.1)$$

where μ is the ratio of the planets' mass (M_{pl}) to the central star (M_\star), and e_1 and e_2 are the eccentricities of planet 1 and 2. The quantity Δ_c is in units of the inner planet's semi-major axis a_1 .

If either the mass of the planets or the mass of the star changes, the critical Hill radius will change as well. An increase in planet mass or a decrease in stellar mass will cause μ to become larger, increasing the width of the zone in which orbits are unstable to close approaches. During post main-sequence mass loss, the orbits of planets will widen as the central star loses mass. As long as this process is adiabatic, the planets will simply conserve their angular momentum and widen their semi-major axis proportionally to the mass lost: $a_{new} = a_{old}(M_i/M_f)$. However, since the orbits widen together by the same factor, Δ remains the same. Thus, while the critical separation at which the two planets will become unstable widens, their relative separation remains unchanged. Orbits that are initially marginally stable, or close to being unstable, will become unstable to close planet–planet approaches as a consequence of the mass loss from the central star. In the case of planetary mass accretion in a protoplanetary disk, the orbits of the two planets will remain the same while Δ_c increases, creating the same effect as if the star were losing mass.

The opposite case of stellar mass accretion or planetary mass loss works to make previously unstable regions more stable. However, since close approaches generally happen within a few tens of orbits, objects likely would be cleared out of an unstable region more quickly than the region could shrink.

2.2.2 Multiple Planet Systems

I expect that multiple planet systems should be common, e.g. the Solar System, PSR 1257+12, and v Andromedae (Wolszczan & Frail 1992; Butler et al. 1999). It is useful to develop an idea of how these systems remain stable. Chambers et al. (1996) found a relation between the separation of a system of planets and the time it would take for the system to suffer a close encounter:

$$\log t = b\delta + c \quad (2.2)$$

where b and c are constants derived through numerical simulations. The symbol δ is related to Δ but is defined in a slightly different way. Here, δ is the separation between two planets ($a_{i+1} - a_i$) in units of mutual Hill radii (R_i) defined as:

$$R_i = \left(\frac{1}{3}\mu\right)^{1/3} \frac{(a_{i+1} + a_i)}{2} \quad (2.3)$$

where i can be from 1 to $N_{planets} - 1$ and I assume the planets have equal masses and initially circular orbits. If the parameter δ is the same for each pair of adjacent planets the separations in units of AU will be different. For example, if I took three Jovian mass

planets ($\mu \sim 10^{-3}$) with $\delta = 6.5$ and the innermost Jovian at 5.2 AU from the central star, the next two planets would be at 9.4 and 16.7 AU. These separations can be compared to the actual orbital radii of 9.6 and 19.1 AU for Saturn and Uranus respectively. I add the obvious caveat that Saturn and Uranus are significantly less massive than Jupiter and have correspondingly weaker mutual interactions.

Adiabatic mass evolution will have the effect of shortening the time it takes for orbits to suffer close approaches. The knowledge of this has long been used to speed up numerical calculations (Duncan & Lissauer 1997, and references therein). However, this fact also leads to the hypothesis that planetary systems on the edge of stability for 10^{10} yr will be affected by mass loss. The new time to close approaches, t_f , for an initial δ with a change in mass is given by:

$$\log \frac{t_f}{t_i} = (b' - b)\delta + (c' - c). \quad (2.4)$$

I would expect c to have little or no change with a change of mass since it represents the timescale for two planets at $\delta \sim 0$ to suffer a close approach. Mass loss will increase the mutual Hill radii of the planets which in turn will change b to a new value I will define as b' :

$$b' = \left(\frac{\mu_i}{\mu_f} \right)^{\frac{1}{3}} b \quad (2.5)$$

where μ_f and μ_i are the final and initial mass ratios respectively. Such behavior suggests that bodies that are stable over the lifetime of a planetary system will become unstable over a timescale several orders of magnitude smaller than their original timescale for instability, when the central star becomes a white dwarf, assuming the relation of Equation 2.2 holds for large δ . It has been found that for the case of three planets with $\mu=10^{-7}$, the parameters are $b \simeq 1.176$ and $c \simeq -1.663$ (Chambers et al. 1996). If the three planets are each separated from their neighbor by $\delta=6$, they will experience close encounters after $\sim 10^5$ orbits of the inner planet. For comparison, three planets with the same mass ratio and separated by a $\delta = 8$ will experience close encounters after 6×10^7 orbits. Assuming the central star loses half of its mass, the timescale to close encounters will shorten by an order of magnitude for the first case and two orders of magnitude for the second.

2.2.3 When is Mass Evolution Adiabatic?

The question of whether mass evolution is adiabatic needs to be addressed. In the case of mass loss by solar mass stars, roughly half the central star's mass will be lost on the order of 10^8 yr. A majority of the mass is lost at the tip of the AGB branch during a period of $\sim 10^6$ yr. Even the highest rate of mass loss translates to a small percentage of total mass lost from the star over one orbital period for planets with semi-major axes inwards of 100 AU, the general region where planets are believed to have formed. Stars heavier than a solar mass probably have superwinds which will cause significant mass loss on the order of a few hundred or thousand years (Vassiliadis & Wood 1993; Schröder et al. 1999). Whether this is important or not will be the subject of further study. Objects very far away from the central star, such as Oort cloud object analogues,

have orbital timescales comparable to the mass loss timescale and will also not follow the adiabatic case. It should be noted that for Kuiper and Oort cloud distances the mass loss by the star would become adiabatic if the asymptotic wind velocity were orders of magnitude smaller than the escape velocity at the surface of the star since the crossing time of the wind would then be larger than the orbital timescale of the comets.

The timescale for mass gain by stars and planets is much slower than the orbital timescale of a planet. Accretion rates for protostars are on the order $10^{-6} M_{\odot} \text{ yr}^{-1}$ (Shu et al. 1987). The formation of giant planets through runaway gas accretion takes $\sim 10^7$ yr, the rough lifetime of gaseous protoplanetary disks (Pollack et al. 1996). If some giant planets are formed more quickly by more efficient runaway accretion, gravitational collapse (Boss 2000), or seeding through the formation of other planets (Armitage & Hansen 1999), they would not be described by the adiabatic case.

2.3 Numerical Methods

In order to test the hypothesis that adiabatic mass evolution should change the stability of planetary systems, I ran several numerical simulations of two planet and multi-planet systems in circular orbits around a central star losing mass. The equations of motion were integrated using a Bulirsch-Stoer routine (Stoer & Bulirsch 1980; Press et al. 1992). Since the case of mass loss of the central star and mass gain of the planet is the same, mass loss can be modeled in two ways. Either the star's mass can be decreased, or the planets' masses can be increased. If the planets' masses are increased, the time coordinate must be scaled to reflect the fact that the orbits are widening. To keep my investigations scalable, I chose the units of time to be orbits of the inner planet. I chose to increase the mass of the planets over a period of 1000 orbits. In the absence of mass evolution, energy and angular momentum were conserved to better than 1 part in 10^6 for 10^5 orbits. Since changing mass makes this a non-conservative system, energy and angular momentum could not be used as a test of accuracy. However, since the simulations were integrated until a close approach and then terminated, any error is similar to the case of no mass evolution. Several simulations without mass evolution were run with stable results. A close approach was defined by an encounter separated by a radius of $< 2\mu^{2/5}$ (Gladman 1993, and references therein). At smaller radii, the planet-planet system is dominant and the star becomes a perturbation. Other authors have chosen different criteria (Chambers et al. 1996), but the results are insensitive to the exact choice.

In the two planet case, I started simulations at the critical separation predicted by Equation 2.1 assuming no mass loss, and increased the separation between the two planets at regular intervals in Δ . I integrated the equations of motion until a close approach or for 10^5 orbits. I increased Δ until it was 25% greater than what would be predicted in the presence of mass loss. These simulations were run an order of magnitude longer than Gladman (1993), and in the no mass loss case were consistent with what was found by Gladman (1993). The two planets initially were started with true anomalies separated by 180° . My separations are lower limits for the critical separation and thus truly reflect the minimum possible separation between orbits that remain stable. For multiple planets, δ was started at 2.2 and raised until several consecutive separations

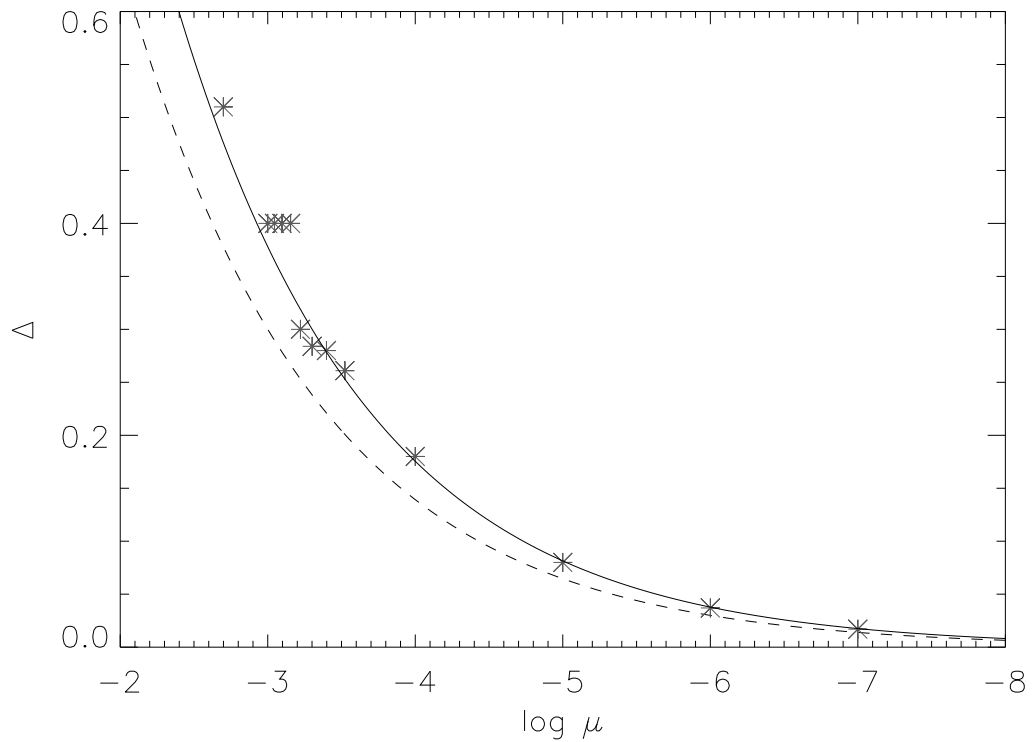


Fig. 2.1 Results of several simulations of instability after mass loss. The dashed line corresponds to the original stability criterion of Equation 2.1. The solid line corresponds to the criterion with $\mu = 2\mu_i$.

did not experience close encounters for 10^7 orbits. Here, random phases in the orbits were chosen with the restriction that adjacent orbits were separated by at least 40° . Three separate runs with different random initial phases were performed to improve the statistics for each mass, as there was significant scatter in the actual time to a close approach for each separation.

2.4 Results

2.4.1 Two Planets

I looked at a wide range of planetary masses for a solar mass star, from a sub-terrestrial-sized planet ($\mu = 10^{-7}$) to a Jovian planet ($\mu = 10^{-3}$). Figure 2.1 shows the border for onset of instability in two planet systems after mass loss. The dashed line represents the initial critical Hill radius for no mass loss. The solid line, which goes through the points, is the critical Hill radius for μ equal to twice that of the initial system, corresponding to the planets doubling in mass or the central star losing half of its mass. Several of the higher mass points are greater than that predicted by the solid curve, an indication of higher order μ terms becoming important. It should be noted that these results are general to any combination of planet and stellar mass that have these ratios.

In a few cases, separations predicted to become unstable after mass loss by the Hill criterion were stable for the length of my simulations. Particularly in the $\mu=10^{-3}$ case, there was a large region in which the two planets suffered no close encounters (See Figure 2.2). These orbits corresponded to a range of Δ from .32 to .37, which were predicted to be unstable under mass evolution from the simple scaling of the equation for Δ . It is interesting to note that all of these orbits are close to the 3:2 resonance (See Fig. 2.3). For the same reason that the Hill radius will not change, these orbits will retain the ratio of their periods. The reason for the stability around the 3:2 resonance may be due to those separations being near but not in a region of resonance overlap (Wisdom 1980; Murray & Holman 2001). Clearly this conjecture needs to be confirmed but that goes beyond the scope of this thesis.

2.4.2 Multiple Planets

Figures 2.4-2.6 show the results for three different runs, looking at three planet systems in circular orbits. I looked at the mass ratios $\mu=10^{-7}$, 10^{-5} , and 10^{-3} . The results are compared to simulations without mass loss, and the difference between the two is quite noticeable for the whole mass range. It is important to note that separations whose time to close approach is comparable to the mass loss timescale show little change in behavior between the two cases. This is because the change in the time to close approach is smaller than the scatter in the simulations. Least squares fitting of the static and mass loss cases were performed to get the coefficients b , c , and b' . To test my assumption of c not changing under mass evolution, I also measured c' , the intercept for the mass loss case. Planets with initial separations in δ that were less than $2\sqrt{3}$, Δ_c in units of R_i , were discarded. For the mass loss case, points where the timescale of close approaches was comparable to the mass loss timescale were also discarded. Once the

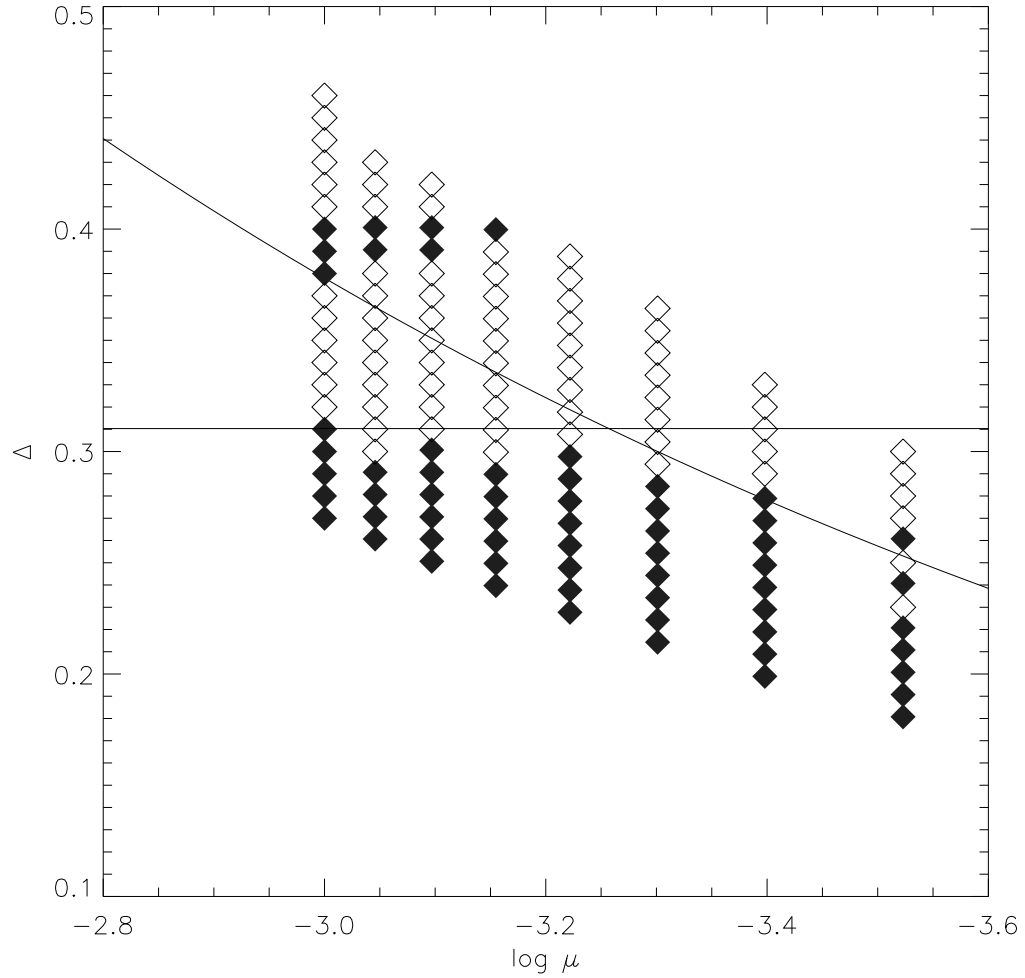


Fig. 2.2 Close-up of Figure 2.1 in the range of $10^{-3.5}$ - 10^{-3} . Open diamonds represent simulations that did not suffer any close approaches over 10^5 orbits. Filled diamonds represent simulations that did suffer a close approach, while the solid curve represents the predicted Δ_c with mass loss. The horizontal solid line shows the relative separation that corresponds to the 3:2 resonance. A region of stability where instability is expected surrounds this resonance.

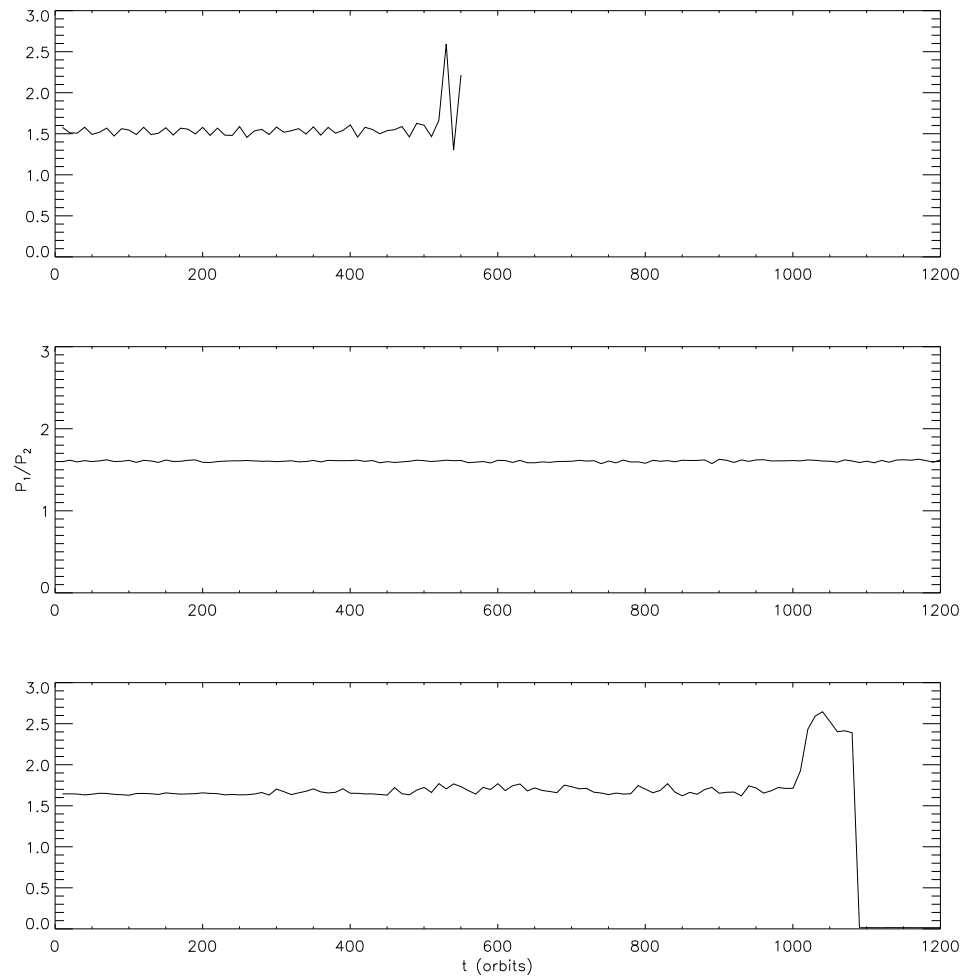


Fig. 2.3 Orbits around the 3:2 resonance for two planet stability. The top and bottom lines correspond to orbits that end in a close approach while the middle line shows an orbit that was stable over the length of the simulations.

coefficients were determined they were compared to what was predicted from Equation 2.2. Similarly, b and c from the $\mu=10^{-7}$ case without mass loss were compared with the results of Chambers et al. (1996). Table 2.1 shows that within the uncertainties, c indeed does not change with mass evolution and the slopes are consistent with predictions. Additionally, my results for the static case with $\mu=10^{-7}$ are consistent with the values of Chambers et al. (1996) for b and c .

As mass increases, the presence of strong resonances becomes more important. This is due to my choice of equal separations and equal masses, many of these resonances would disappear with small variations in mass, eccentricity, and inclination (Chambers et al. 1996), aspects that will be tested with further study. The presence of resonances is most easily seen in Figure 2.6 where $\mu=10^{-3}$. In the range of $\delta=4.4$ to 5.2, the points greatly depart from the predicted curve. The spike at $\delta=5.2$ corresponds to the first and second, as well as the second and third planets being in 2:1 resonances. This particular example shows that the basic dynamics of a system undergoing adiabatic mass evolution favor stability near strong resonances. Such a process potentially could augment the current ideas about how resonant extrasolar planets such as those around GJ876 formed (Snellgrove et al. 2001; Murray et al. 2002; Rivera & Lissauer 2000).

Table 2.1. Coefficients for Equation 2.2

μ	b^a	c	b'	c'
10^{-7}	1.16 ± 0.04	-1.6 ± 0.2	0.87 ± 0.05	-1.4 ± 0.3
10^{-5}	1.46 ± 0.12	-2.4 ± 0.6	1.14 ± 0.05	-2.5 ± 0.3
10^{-3}	2.5 ± 0.5	-6 ± 2	1.2 ± 0.5	-3 ± 2

^aCoefficients derived through numerical simulations of three planets in circular orbits for a starf undergoing both mass loss (primed coefficients) and no mass loss (unprimed coefficients). Errors quoted are 1σ . The $\mu=10^{-7}$ case can be compared to the results from Chambers et al. (1996), who determined that $b=1.176 \pm 0.051$ and $c=-1.663 \pm 0.274$.

2.4.3 Observational Implications

These simulations have several observational implications which can be broadly separated into two categories—the character of planetary systems and their observational signature in white dwarfs.

Surviving planets that are marginally stable will suffer close approaches soon after the star evolves into a white dwarf, or possibly as early as the AGB phase. There are

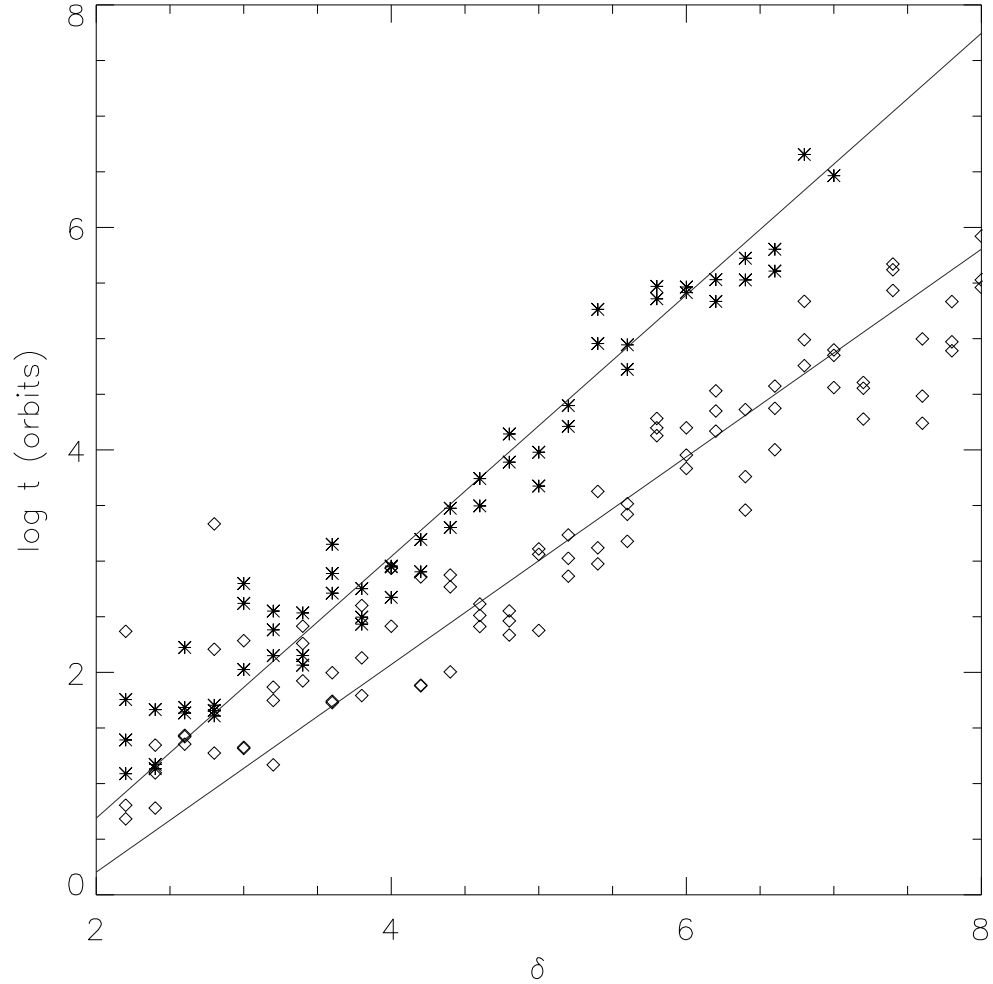


Fig. 2.4 Comparison of the timescale to the first close approach for a system of three $\mu=10^{-7}$ planets with and without mass loss, where asterisks represent static masses and open diamonds represent the presence of mass loss. The top line is given by least-squares fitting a line of slope b and intercept c for no mass loss. The bottom line is given by Equation 2.5.

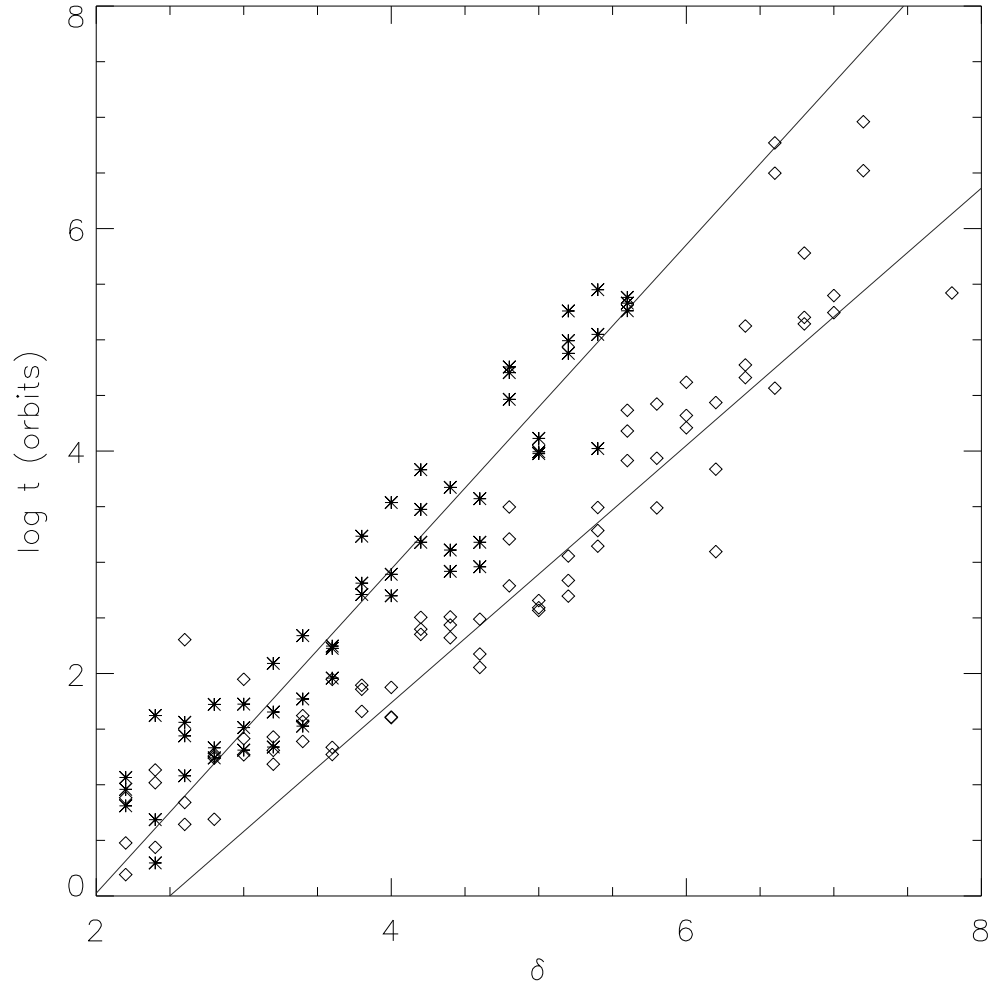


Fig. 2.5 The $\mu = 10^{-5}$ case, symbols the same as in Figure 2.4. The slope and intercept of the top line was derived by fitting the numerical simulations without mass loss. The slope of the bottom line is the predicted change due to mass loss.

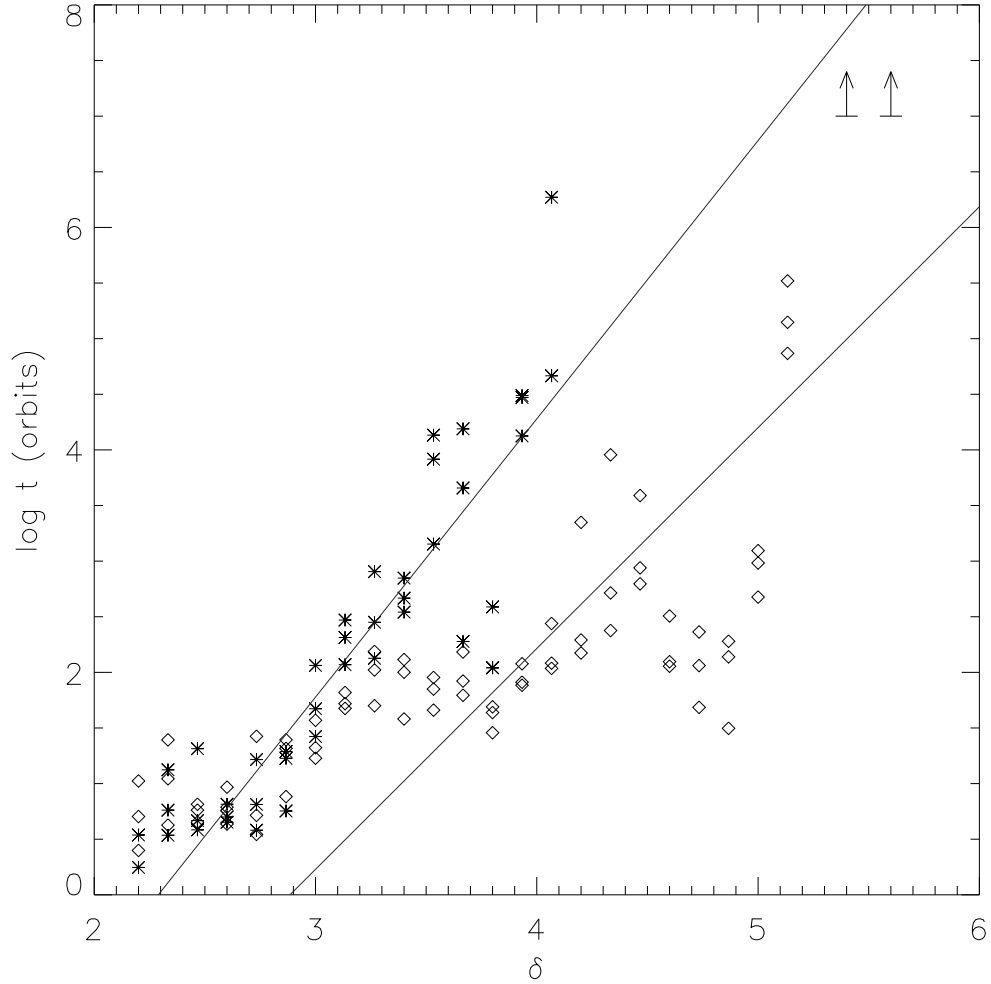


Fig. 2.6 The $\mu=10^{-3}$ case, symbols the same as in Figure 2.4. The arrows indicate separations at which my simulations remained stable for 10^7 orbits. The slope and intercept of the top line was derived by fitting the numerical simulations without mass loss. The presence of strong resonances is particularly noticeable as enhanced stability around $\delta=5.2$ for the mass loss case, which corresponds to the 2:1 resonance.

three possible end states for planets that suffer close approaches: ejection, collision, or a settling into a different and more stable configuration for all planets. The case of two planets has been studied carefully, and for two Jovian mass planets with one planet starting at ~ 5 AU, the probability of collision is roughly 8%, ejection 35%, and rearrangement 57% (Ford et al. 2001). I naively assume that these results hold similarly for multiple planets as well, since collisions have been shown to hold for multiple planet systems (Lin & Ida 1997), while ejections and rearrangements should have a similar probability (certainly to within a factor of 2 or so). Ejections will leave planets that are closer to the white dwarf, while often a rearrangement will leave one or two planets with larger semi-major axes (up to $\sim 10^3$ times greater) and one with a smaller semi-major axis (as close as 10 times smaller). Collisions are potentially more exciting because as the two planets merge they essentially restart their cooling clock and as such will be anomalously luminous by 2 orders of magnitude for 10^8 yr (Burrows et al. 2003; Zhang & Sigurdsson 2003).

To estimate how many white dwarfs might have planets that collided (F_c), I can take the fraction of white dwarfs that have marginally stable planets and multiply them by the fraction of marginally stable planets that have collisions:

$$F_c = f_{pl} f_{ms} f_c \quad (2.6)$$

where f_{pl} is the fraction of white dwarfs with planets, f_{ms} is the fraction of marginally stable planet systems, and f_c is the fraction of marginally stable systems that suffer a collision. I can estimate the number of Jovian sized planets around white dwarfs by looking at the number of young stars that still have significant disks after 1 Myr, the approximate time to form a Jovian planet. This has been found to be about 50% of young stars in nearby clusters (Haisch et al. 2001). Several numerical simulations (Barnes & Quinn 2001; Laughlin & Adams 1999; Quinlan 1992; Rivera & Lissauer 2000; Barnes & Quinn 2004, for example,) point to a high frequency of marginally stable systems around stars as well as the discovery of the marginally stable planetary systems around GJ876 and HD 82943 (Murray & Holman 2001). However, factors such as multiple planets with widely different mass ratios could greatly change the effects of stability. I estimate this fraction to be about 50% as well, although a large uncertainty is associated with this estimate. Taking the results above, I estimate then that $\sim 2(f_{ms}/0.5)\%$ of young white dwarfs should have the product of a recent planet-planet collision in orbit. Thus I predict that observations of young ($\tau \ll 10^9$ yr) white dwarfs should reveal that $\sim 2\%$ have overluminous planet mass companions, some in orbits with semi-major axis smaller than the minimum (5 AU) expected to survive the AGB phase. These planets would be detectable through their significant IR excess and should be distinguishable from brown dwarf companions by their lower gravity.

A natural byproduct of the formation of Jovian planets is the existence of a large cloud of comets at large heliocentric distances (Oort 1950; Weissman 1999). The survival of such a cloud through post-main-sequence evolution has been closely studied in the context of accounting for observed water emission in AGB stars and an explanation for metals in DA white dwarfs (Stern et al. 1990; Alcock et al. 1986; Parriott & Alcock 1998). The general result to date is that comets at semi-major axes greater than a

few hundred AU survive the AGB phase. Massive comets are then predicted to strike the central white dwarf at a rate of $\sim 10^{-4} \text{ yr}^{-1}$, depositing fresh metals in the white dwarf photosphere. Such a cometary influx can account for the DAZ phenomenon but has difficulty explaining some of the strongest metal line systems. The photospheres of these DAZs are predicted to have short metal residence times which implies a high rate of accretion. An alternate explanation for the origin of metals in white dwarfs is ISM accretion, where a steady drizzle of metal rich dust is spherically accreted from the ambient ISM. Both scenarios have difficulty explaining the frequency of DAZ white dwarfs and accounting for those systems with the strongest metal lines and shortest residence times.

Recent observations of the DAZ phenomenon do not seem to be consistent with either scenario (Zuckerman & Reid 1998; Zuckerman et al. 2003). In one DAZ, WD 1337+705, the diffusion time for metals is 3 days, which means that neither of the previous scenarios can explain the high observed metal abundances nor the stability of the metal lines (Holberg et al. 1997). Another white dwarf, WD 2326+049, has a high abundance as well as an infrared excess, possibly from a dust disk at small orbital radii (Zuckerman & Becklin 1987; Koester et al. 1997).

The evolution of a planetary system after post-main sequence mass loss coupled with the presence of an Oort cloud may provide an alternative explanation for the DAZ phenomenon and in particular the peculiarities of WD 2326+049 and WD 1337+705.

2.4.3.1 Cometary dynamics

The mass loss during post-main-sequence is near impulsive for Oort cloud comets. Previous work has shown that a significant fraction of any Oort cloud like objects will survive the mass loss phase, even in the presence of mildly asymmetric mass loss (Alcock et al. 1986; Parriott & Alcock 1998). The immediate result of the mass loss phase is to leave the remaining bound objects on orbits biased towards high eccentricity, but with similar initial periastron distance. Orbital time scales are on the order of 10^6 yr.

The number and typical size of Oort cloud objects is poorly constrained, but canonical estimates scale to 1 km sized comets. These comets are mostly composed of low density ices and silicates, with masses of $\sim 10^{16}$ g each. There are approximately 10^{12} objects per star. Clearly there is a range of masses, and it is possible the true numbers and masses of Oort cloud comets vary by several orders of magnitude from star to star. Dynamical effects also lead to a secular change in the amount of mass in any given Oort cloud.

External perturbations ensure a statistically steady flux of comets from the outer Oort cloud into the inner system. Interactions with Jovian planets lead to tidal disruption of comets (and direct collisions), scattering onto tightly bound orbits restricted to the inner system, ejection from the system, and injection into central star encountering orbits. For the Solar System, the flux of comets into orbits leading to collision with the Sun is of the order 10^{-2} per year. Of these, a significant fraction undergo breakup before colliding with the Sun, with individual fragments colliding with the Sun over many orbital periods (Kreutz sungrazers). SOHO detects $\sim 10^2$ such objects per year in the Solar System, or one every 3 days on average. A single 1 km comet can fragment

into $\sim 10^4$ fragments with sizes of order 50 m, consistent with those observed by SOHO, and consistent with the collision rates estimated both for the parent comets and the fragments. Each fragment then deposits about 10^{12} g into the Solar photosphere. Note that if the typical comet were 20 km rather than 1 km, the deposition rate would be about 10^{16} g every three days.

A white dwarf has a radius about 0.01 of the solar radius. Due to gravitational focusing, the cross-section for collision for comets scattered into random orbits in the inner system is linear in radius, so the collision rate expected for a white dwarf with a solar-like Oort cloud is 10^{-4} yr^{-1} . However, the perturbation of the outer orbits due to AGB mass loss, combined with the expansion of the outer planet orbits will drastically change this rate, leading to a new, late “heavy bombardment” phase with significantly higher rates of comet influx into the inner system. If one of the outer (Jovian mass) planets is scattered into a large ($a_{fin} \gg a_{in}$) eccentric orbit after the onset of instability, as I expect to happen in about 2/3 of the cases, then there will be strong periodic perturbations to the outer Kuiper belt and inner Oort cloud. About 10% of those systems will lead to the outermost bound planet being placed on very wide ($a_{fin} \gtrsim 10^3 a_{in}$) highly eccentric orbits, with orbital time scales comparable to the cometary orbital timescales. Perturbations on the Oort cloud from these planets lead to a persistent high flux of comets to the inner system, until the Oort cloud is depleted of comets.

The net effect of the dynamical rearrangement of the post-main-sequence planetary system is a greatly enhanced rate of cometary influx into the inner system, starting 10^7 - 10^8 years after the mass loss phase, tapering off gradually on timescales of 10^8 - 10^9 years, leading to enhanced metal deposition to the white dwarf photosphere, and increased dust formation in the inner system for some white dwarfs, depending on the final configuration of the outer planets.

Several processes affect the comet bombardment rate:

- A fraction of the previously stably orbiting outer Kuiper belt objects, that survived the AGB phase, are injected into the inner system by newly established dynamical resonances with the outer planets over $\sim 10^8$ years;
- Planets ejected to the outer Oort cloud by planet-planet perturbations will randomise the orbits of a small ($\sim 4(m/M)^2$) fraction of the Oort cloud comets, some of these will enter the inner system providing an enhanced flux of the normal Oort comet infall over $\sim 10^9$ years.
- Surviving inner planets, scattered to the smaller orbital radius, will trap the comets injected into the inner system, providing both direct tidal disruption at a few AU, and providing a much higher influx of comets to very small radii where they are tidally disrupted by the white dwarf (or in rare cases collide directly).
- Dust from tidally disrupted cometary debris will be driven to the white dwarf surface by PR drag, while larger debris will be dragged in through the Yarkovsky affect, both on a timescale shorter than the WD cooling time.

I expect the Kuiper belt to be severely depleted by the post-main-sequence phase (Stern et al. 1990; Melnick et al. 2001; Ford & Neufeld 2001). However, a substantial

population of volatile depleted rocky bodies may survive the AGB phase in the outer belt. A substantial fraction of these burnt out comets will become vulnerable to resonant perturbations by the surviving outer planets, now in new, wider orbits. The outer belt objects have orbital periods ($\sim 10^4$ - 10^5 years) that are comparable to the shortest AGB mass loss timescales, and therefore will not generally expand adiabatically in proportion to the expansion of the planetary orbits. The solar Kuiper belt is inferred to have $\sim 10^5$ objects with size above 100 km, assuming a mass function characteristic of such populations, with approximately equal mass per decade of mass. I infer a population of $\sim 10^{11}$ Kuiper belt objects with size of about 1 km, at an orbital radius of order 10^3 AU. Approximately 1% of those will be vulnerable to the new dynamical resonances after the AGB phase, allowing for evaporative destruction and ejection, I estimate $\sim 10^8$ Kuiper belt objects will enter the inner system in the 10^7 - 10^8 years after the AGB phase. The rate will peak at $\sim 10^8$ years and then decline as the reservoir of cometary bodies in orbits vulnerable to the new planetary resonances declines.

If there are multiple surviving Jovian planets, then the post-AGB planet-planet interactions will typically leave the inner planets on eccentric orbits, leading to broader resonances and a larger fraction of perturbed Kuiper belt objects. I expect in $\sim 2/3$ of the cases where there were multiple, marginally stable Jovian planets in the outer system the final configuration to have an eccentric outer planet and a more tightly bound inner planet.

Some of the comets injected into the inner system will be tidally disrupted by the surviving Jovian planets. Some comets will be ejected and some will be injected into the inner system to be tidally disrupted by the white dwarf (about 1% of those will directly impact the white dwarf). Dynamical time scales in the inner system are $\sim 10^2$ years, and the probability of ejection or disruption per crossing time is of the order of 10^{-2} per crossing time, assuming there is an inner planet, scattered inward of 5 AU, matching the outer planet scattered to wider orbital radius. So at any one time $\gtrsim 10^3$ Kuiper belt objects are in the inner system. The rate for tidal disruption by the surviving innermost Jovian planets is $\sim 10^{-6}$ yr $^{-1}$ per comet. Tidal disruption rates due to close approaches to the white dwarf may be as high as $\gtrsim 10^{-4}$ yr $^{-1}$ per comet, the rates are uncertain because of the possibility of non-gravitational processes breaking up the comet and deflecting debris. With each comet massing about $\gtrsim 10^{16}$ g, by hypothesis, I get a flux of disrupted cometary material, from the Kuiper belt remnant, assuming Solar System like populations, of 10^{14} - 10^{16} g yr $^{-1}$ of metal rich material. Given my assumed mass function, disruption of rarer more massive comets can sustain mass accretion rates an order of magnitude higher still for time scales comparable to the inner system dynamical time scales, in a small fraction of systems.

I can now compare my mechanism to the accretion rates needed to explain the constant, detected metal lines in WD 2326+049 and WD 1337+705, two DAZ white dwarfs with the highest measured abundances of Ca. An accretion rate has already been quoted in the literature for WD 1337+705, where $\sim 3 \times 10^{17}$ g yr $^{-1}$ of solar abundance ISM would need to be accreted (Holberg et al. 1997). In a volatile depleted case, only metals would be present converting to $\sim 6 \times 10^{15}$ g yr $^{-1}$ for cometary material. WD 2326+049 also has a roughly estimated value of $\sim 1 \times 10^{19}$ g yr $^{-1}$ corresponding to $\sim 2 \times 10^{17}$ g yr $^{-1}$ in the volatile depleted case (Koester et al. 1997).

Both of these estimates were based on calculations made by Dupuis et al. (1992, 1993a,b), who uses the ML3 version of mixing length theory. In fact, there are several other methods that can be used to model the convective layer of white dwarfs, including using other efficiencies of the ML theory and the CGM model of convection (Althaus & Benvenuto 1998). The calculations differ by up to four orders of magnitude on the mass fraction q of the convection layer's base in white dwarfs with T_{eff} similar to WD 2326+049. Taking values of q for the base of the convection layer from Figures 4 and 6 in Althaus & Benvenuto (1998) and getting values for the diffusion timescale from tables 5 and 6 in (Paquette et al. 1986) one can estimate what steady state accretion rate WD 2326+049 requires for the different models. The smallest rate came from ML1 theory and the largest from ML3 theory, with CGM having an intermediate value, giving a range of $\sim 2 \times 10^{13} \text{ g yr}^{-1}$ to $\sim 4.4 \times 10^{17} \text{ g yr}^{-1}$. I favor the CGM value of $\sim 10^{15} \text{ g yr}^{-1}$, which is consistent with the estimate based on observations conducted by Graham et al. (1990). The rate for WD 1337+705 may be more robust due to the fact that convective models converge for hotter white dwarfs.

Both rates are consistent with my scenario if either white dwarf has two Jovian mass planets, one in a $\gtrsim 10 \text{ AU}$ *eccentric* orbit and another in a $\lesssim 5 \text{ AU}$ orbit. Alternatively, their progenitors had an order of magnitude richer Kuiper belt population than inferred for the Solar System. With a post-AGB age of $\sim 6 \times 10^8$ years, and a mass of $\sim 0.7M_{\odot}$, the original main sequence star of WD 2326+049 was most likely more massive than solar and a more massive planetary and cometary system is not implausible. WD 1337+705 is almost 10^8 years old and would represent an object close to the peak of predicted cometary activity.

My scenario may provide a consistent picture for the presence of DAZ white dwarfs and their anomalous properties (Zuckerman & Reid 1998; Zuckerman et al. 2003). I don't expect all white dwarfs to have metal lines. Only about 2/3 of those which possessed marginally stable planetary systems containing two or more Jovians at orbital radii greater than $\sim 5 \text{ AU}$ will be able to generate significant late cometary bombardment from the outer Kuiper belt and inner Oort cloud. Following a similar estimate as in Equation 2.6, I predict about 14% of white dwarfs will be DAZs. The rate will peak after $\sim 10^8$ years, after the planet-planet perturbations have had time to act, and then decline as the reservoir of perturbable comets is depleted. The convective layer of the white dwarf will also increase by several orders of magnitude over time which would create a sharp drop of high abundance DAZs with decreasing T_{eff} . The drop would be greatest between 12000K and 10000K where the convective layer has its steepest increase (see Figure 4 of Althaus & Benvenuto 1998). Zuckerman et al. (2003), in conducting their survey of DAZ white dwarfs, estimated that $\sim 25\%$ of white dwarfs were DAZ and that metal abundance dropped with T_{eff} sharply between 12000K and 8000K.

I expect DAZ white dwarfs to have potentially detectable (generally) multiple outer Jovian planets, whose orbits will show dynamical signatures of past planet-planet interaction, namely an outer eccentric planet and an inner planet inside the radius scoured clean by the AGB phase.

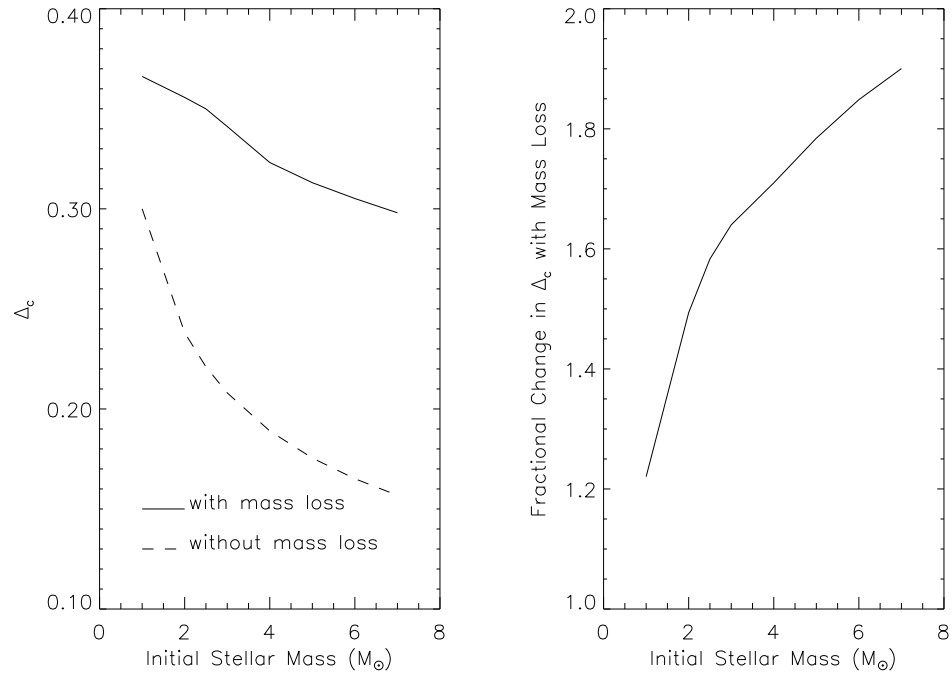


Fig. 2.7 Comparison of Δ_c with and without mass loss as a function of the central star's original mass. The right panel shows the fractional change of Δ_c when mass loss occurs. For both panels the fractional change in mass is calculated using the M_i - M_f relation of Weidemann (2000).

2.5 Discussion

Using the above results I can compare the greatest fractional change in stability for two Jovian planets around different stars $> 1 M_{\odot}$ that produce white dwarfs. I took the initial-final mass relation of Weidemann (2000) and calculated Δ_c without mass loss and with mass loss (Δ'_c). As can be seen in Figure 2.7, the higher the initial mass star, the greater the fractional change. This is expected, since higher mass stars lose more mass to become white dwarfs. The best candidates for unstable planetary systems would be higher mass white dwarfs, if planet formation is equally efficient for the mass range considered here. The scheme conjectured in this Chapter provides a method for identifying and observing the remnant planetary systems of intermediate mass stars, which might otherwise be hard to observe during their main sequence life time.

One can predict the change in the critical separation where two planets will remain stable based on the change in μ over time, simply by differentiating Δ_c with time:

$$\frac{d\Delta_c}{dt} = \mu^{-2/3} \frac{d\mu}{dt}. \quad (2.7)$$

In the general case $d\mu/dt$ depends on two factors, the change in mass of the central star and the change in mass of the planets, given by

$$\frac{d\mu}{dt} = \mu \left(\frac{d \ln M_{pl}}{dt} - \frac{d \ln M_{\star}}{dt} \right). \quad (2.8)$$

For the critical separation to widen, μ must increase with time. Putting the Equations 2.7 and 2.8 together gives the rate of change in Δ_c :

$$\frac{d\Delta_c}{dt} = \mu^{1/3} \left(\frac{d \ln M_{pl}}{dt} - \frac{d \ln M_{\star}}{dt} \right). \quad (2.9)$$

The results of my multi-planet simulations are scalable to many situations, but for planet systems surviving around white dwarfs I am interested in timescales of $\sim 10^{10}$ yr for solar type stars to $\sim 10^8$ yr for higher mass stars. The highest δ I studied for $\mu=10^{-3}$ was roughly 5.2, which by Equation 2.2 corresponds to a timescale to close approaches of 10^7 orbits of the inner planet. After the central star loses half of its mass, the timescale shortens to ~ 2000 orbits. For a planetary system with $\delta=5.2$ to be stable over the main sequence lifetime of the star, the minimum semimajor axis of the innermost planet for a higher mass star (for example, $4M_{\odot}$) would be 8.2 AU and 100 AU for a solar-type star. Longer integrations need to be performed to investigate the behavior of systems with larger values of δ . I expect my resulting timescales for the onset of instability to scale to larger δ . The initial computational effort I made here limited the exploration of slowly evolving systems with large δ in exchange for a broader exploration of the other initial condition parameters. It will also be instructive to model systems with unequal mass planets, to explore the probability of ejection and hierarchical rearrangement as a function of planetary mass ratio.

The sensitivity of stability to changes in mass has implications for planet formation as well. Further research on the migration of Hill stable regions while the planet/star

mass ratio evolves may illuminate further the general issue of how Jovian planets in the process of formation become unstable to close encounters and gross changes in orbital parameters (Ford et al. 2001). One possibility is that the mass accretion of the planets occurs at a rate fast enough that $d\mu/dt > 0$. Other factors would need to be considered, in particular the interplay between the onset of rapid mass accretion by the planet, and the accretion rate from the protoplanetary disk onto the central protostar. Gas drag and stellar mass accretion could work to stabilize orbits if the planets are embedded in a circumstellar disk, while orbital migration would change the relative separations of proto-planets. Since the stability of multi-planet systems is also sensitive to changes in mass ratio, this could help solve problems of isolation for planetary embryos and speed up the timescale for the production of giant planet cores.

The dependence of stability on both the mass of the planet and the mass of the central star suggests that stars of different masses may be more efficient at producing a certain size planet. This is exemplified by the fact that μ for a Jovian planet can change by an order of magnitude in either direction over the mass range of stars that might have planetary companions. For larger mass stars, planets can be more tightly spaced and still be mutually dynamically stable, which suggests that when planets are forming it is easier for them to become dynamically isolated in disks around more massive protostars. For lower mass stars, there is a wider annulus in which material is unstable to planetary gravitational perturbations, and so forming planets would have a larger reservoir of material from which to draw. Other factors, such as a star's temperature and radiation pressure, would play into this result as well and may dominate over this scenario. However, such effects will tend to reinforce the conclusion that less massive stars should be more efficient at creating more massive planets while higher mass stars will produce more, lighter planets if they are capable of forming planets at all. This prediction will be testable as many space and ground based programs are devoting a great deal of effort to look for planetary companions to stars.

Chapter 3

Limits to Substellar Companions Around DAZs

This work in this chapter is contained in:

Debes, J. H., Sigurdsson, S., & Woodgate, B. 2005, ApJ, (submitted)

Debes, J. H., Sigurdsson, S., & Woodgate, B. 2005, AJ, (in press)

3.1 Introduction

There are currently three explanations for the origin of DAZ WDs, accretion of the ISM, accretion of a wind from unseen companions, or accretion of comets perturbed by unstable planetary systems. For two of these three sources mentioned in Chapter 2, unseen planetary or substellar objects lurk in the glare of nearby white dwarfs. DAZs represent a promising population for a search for cool objects in orbit around WDs. If such companions can be detected, this will open an exciting chapter in the study of extra-solar planets by presenting several objects that can be directly detected and thus characterized, constraining a host of theoretical issues, such as extra-solar planetary atmospheres and the long term evolution of Jovian planets. Such experiments in the stellar graveyard can support future missions dedicated to the detection and characterization of terrestrial planets. White dwarfs then represent an intermediate step between current technology and what is needed for observations made with the James Webb Space Telescope (JWST) and the Terrestrial Planet Finder (TPF). Additionally, DAZs could potentially have a higher probability of harboring planets and have a direct impact on understanding the dynamical evolution of planetary systems.

To that end I was motivated to search the seven brightest and closest DAZ white dwarfs with the NIC-2 coronagraph on the NICMOS instrument of the Hubble Space Telescope (HST). This search was part of the the Cycle 12 program 9834, completed over the course of 2003 and 2004 with 14 orbits. I present the observations I made in Section 3.2 and detail my data analysis in Section 3.3. We present candidate planetary and brown dwarf companions in Section 3.4 as well as place limits on the types of candidates I could have detected in Section 3.5.

3.2 Observations

3.2.1 Observational Strategy

Only ~ 34 DAZs are currently known to exist, since detection of the weak metal lines are difficult without a high signal-to-noise, high resolution spectrograph (Zuckerman et al. 2003). Six of the most promising DAZ white dwarfs discovered or confirmed in the Zuckerman et al. (2003) survey were targeted for observation with NICMOS and are listed in Table 3.1. My seventh target, WD 1620-391, was chosen for the presence of circumstellar gas absorption features as well as photospheric absorption due to Si and C (Holberg et al. 1995). I chose these targets based on the fact that these were the brightest and closest DAZs known. Each target was observed with the NIC-2 coronagraph in the F110W filter. The most promising targets, WD 2326+049, WD 1337+701, and WD 1620-391 were imaged in the F160W filter as well. Both WD 2326+049 and WD 1337+701 have the highest [Ca/H] abundances measured with the exception of the newly discovered DAZ GD 362 (Gianninas et al. 2004). WD 1620-391 was chosen for extra observations due to the presence of circumstellar material. These three targets were also observed without the coronagraph for shorter exposures in the F110W, F160W, and F205W filters in an attempt to resolve any smaller structure or companions at separations $< 0.8''$. For the other targets, acquisition images were used to detect anything separated by $< 0.8''$..

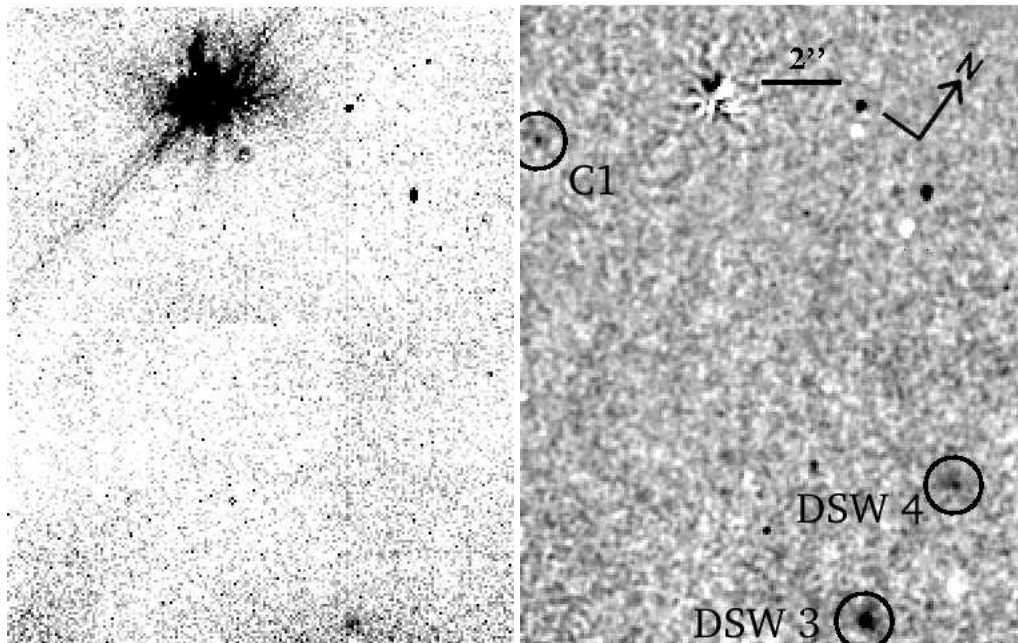


Fig. 3.1 Image of WD 2326+049 in the F160W filter before (left) and after (right) PSF subtraction. The right panel has been smoothed with a Gaussian filter to show a candidate companion (C1) and two extragalactic objects (DSW 3,4).

Table 3.1. Table of Target White Dwarfs

WD	Name	M_f (M_\odot)	M_i (M_\odot)	T_{eff} (K)	Total Age (Gyr)	Distance ^a (pc)	References
0208+396	G 74-7	0.64	2.7	7310	3.2	17	1
0243-026	G 75-39	0.70	3.6	6820	2.8	21	1
0245+541	G 174-14	0.76	4.4	5280	7.3	10	1
1257+278	G 149-28	0.58	1.7	8540	3.3	34	1
1337+701	EG 102	0.57	1.51	20435	3.6	25	2,3
1620-391	G 29-38	0.66	3.0	24406	1.1	12	4
2326+049	CD-38°10980	0.70	3.6	11600	1.1	14	2,5

^aDistances derived from parallax measurements compiled in (1). If not available, (3) and (5) were used.

References. — (1) Bergeron et al. (2001) (2) Liebert et al. (2004) (3) Perryman et al. (1997) (4) Bragaglia et al. (1995) (5) van Altena et al. (2001)

The coronagraph on NICMOS suppresses the PSF of the star by more than an order of magnitude, but a residual coronagraphic PSF remains that still limits contrast. PSF subtraction is then used to remove the remaining light. Due to the large time it takes the telescope to slew from one target to another, it is unfeasible to have a second PSF reference star. It is necessary to use the current target as the PSF reference. To use the same target without subtracting the flux from companions, a spacecraft roll is performed in the middle of the orbit. Images at one roll angle can be subtracted from the other and can later be rotationally registered to gain signal to noise. Figure 3.1 demonstrates the result of a typical subtraction, where the coronagraphic PSF is suppressed by a factor of 20-50. Any putative point sources in the field will possess a distinctive pair of positive and negative conjugate images that are separated by the differential roll angle. Any point source that is detected must then fulfill several criteria. A detected object must have both a positive and negative conjugate image, and both images must have the same flux.

Following the prescription of Fraquelli et al. (2004), two coronagraphic exposures of ~ 600 s were taken at two different spacecraft roll angles. Each exposure was separated by a differential roll angle of 10° . The differential roll angle between images limits the angular separation at which one can detect a point source. A realistic requirement is at least a two pixel separation between the centroids of the positive and negative conjugates to avoid the self-subtraction of any point source companions. This requirement is tempered by the need to spend most of the HST orbit observing the target and not rolling the spacecraft. For my observations I concentrated on integration time and chose

Table 3.2. Table of HST Observations

WD	Observation Group	Date & Time (UT)	Integration Time	Filter	
0208+396	N8Q320010	2003-09-15 19:42:00	575.877	F110W	
	N8Q322010	2003-09-15 20:10:00	575.877	F110W	
0243-026	N8Q322010	2003-09-18 18:11:00	575.877	F110W	
	N8Q323010	2003-09-18 18:39:00	575.877	F110W	
0245+541	N8Q318010	2003-08-26 21:11:00	575.877	F110W	
	N8Q319010	2003-08-26 21:39:00	575.877	F110W	
	N8Q368010	2004-10-24 07:45:00	575.877	F110W	
	N8Q369010	2004-10-24 09:11:00	575.877	F110W	
1257+278	N8Q316010	2004-02-18 11:12:00	575.877	F110W	
	N8Q318010	2004-02-18 11:41:00	575.877	F110W	
1337+701	N8Q302010	2003-12-01 17:09:00	25.918	F205W	
	N8Q302011	2003-12-01 17:11:00	25.918	F205W	
	N8Q302020	2003-12-01 17:20:00	21.930	F160W	
	N8Q302030	2003-12-01 17:24:00	19.936	F110W	
	N8Q308010	2004-02-05 21:40:00	575.877	F110W	
	N8Q309010	2004-02-05 22:45:00	575.877	F110W	
	N8Q310010	2004-02-05 23:13:00	575.877	F160W	
	N8Q311010	2004-02-06 00:27:00	575.877	F160W	
	1620-391	N8Q303010	2003-09-07 06:12:00	23.924	F205W
		N8Q303011	2003-09-07 06:13:00	23.924	F205W
N8Q303020		2003-09-07 06:22:00	17.942	F160W	
N8Q303030		2003-09-07 06:25:00	15.948	F110W	
N8Q312010		2004-03-08 03:22:00	575.877	F110W	
N8Q313010		2004-03-08 03:52:00	575.877	F110W	
N8Q314010		2004-03-08 05:00:00	575.877	F160W	
N8Q315010		2004-03-08 05:27:00	575.877	F160W	
2326+049		N8Q301010	2003-10-20 10:07:00	17.942	F205W
		N8Q301011	2003-10-20 10:08:00	17.942	F205W
	N8Q301020	2003-10-20 10:15:00	11.960	F160W	
	N8Q301030	2003-10-20 10:20:00	11.960	F110W	
	N8Q304010	2003-09-14 19:31:00	575.877	F110W	
	N8Q305010	2003-09-14 19:59:00	575.877	F110W	
	N8Q306010	2003-09-14 21:07:00	575.877	F160W	
	N8Q307010	2003-09-14 21:35:00	575.877	F160W	

a roll angle of 10° , leading to an inner radius limit to extreme high contrast imaging with self-subtraction of $0.86''$.

Table 3.2 shows a log for all of the observations taken along with the total exposure times and the filter used. Each F110W observation was designed to be sensitive enough to detect an object with $m_{F110W} \sim 23$ with a S/N of 10, which for a 1 Gyr substellar object at 10 pc would correspond to a $\sim 5 M_{Jup}$ planet. For my seven targets, which range in age from 1 Gyr to 7 Gyr and 10 to 34 pc, the images are sensitive to 7-18 M_{Jup} objects.

In addition to the seven targets, three reference stars were observed within the same orbit as the three WD targets imaged without the coronagraph. The goal was to use these to subtract out the primary targets' PSF. These targets were chosen to be close to the original target and have similar near-IR colors to aid in PSF subtraction.

One group of observations taken of WD 0245+541 failed due to an incorrect calibration of the flight software (FSW) onboard the telescope. As a result, WD 0245+541 was not placed behind the coronagraphic hole. The problem was identified by the HST staff and further observations did not show the same problem. A repeat observation was taken in October 2004, but the original failed observations were also used for my data analysis.

Due to the detection of a candidate planetary candidate around WD 2326+049 (G 29-38), second epoch observations were taken with the Gemini North Telescope using the Altair adaptive optics system in conjunction with the NIRI camera. The AO system on Gemini North, Altair, can successfully guide on stars with $R \sim 13$, such as WD 2326+049. By concentrating a diffraction limited fraction of the total flux of a dim object, the background can be overcome for extremely faint near infrared point sources. In addition, under sub-arcsecond observing conditions, the full width at half-maximum (FWHM) of the core on Altair images is ~ 60 -90 mas, providing the possibility to resolve structures better than HST (Hutchings et al. 2004).

The Gemini observations were taken on August 5, 2004. A total of 4×15 s frames were co-added at 10 dither points to subtract the background and remove pixel to pixel defects, for an effective integration on source of forty minutes. My total integration returned an average FWHM of 75 mas, significantly smaller than the diffraction limit of our F110W images with HST.

3.3 Data Analysis

The images were reduced by the calibration pipeline provided for NICMOS. In addition to the pipeline, certain steps were taken in an effort to improve the quality of the final images, roughly following the procedure set out by Fraquelli et al. (2004). Each 600 s exposure was broken up into two or three exposures for ease in rejecting cosmic rays. Each calibrated subexposure had pedestal subtraction by the PEDSUB routine in IRAF through the STSDAS package. Each subexposure was registered and median combined with sigma clipping to create a final exposure at a particular roll angle. The two images at different roll angles were subtracted one from the other and vice versa to create two difference images, one ROLL1-ROLL2 and the other ROLL2-ROLL1. One difference image was rotationally registered and median combined to produce the final

total image. Figure 3.1 demonstrates the before and after pictures of a subtraction shown at the same image stretch. The residual light due to the coronagraphic PSF is dominated by systematic errors but in general is a factor of 20-50 times dimmer after subtraction.

In the case of WD 0245+541, several other steps had to be taken for the failed observation, since at each roll angle the star was at a different position and not behind the coronagraphic hole. To combat this problem the two images were registered and difference images were produced. The final result was of sufficient quality to determine the presence of several candidate objects in the field.

The second epoch Gemini data were processed using several IRAF tasks designed by the Gemini Observatory and based upon the samples given to observers. Each frame was flatfielded and sky subtracted. In addition, due to the on-sky rotation from the Cassegrain Rotator being fixed, each frame was rotationally registered and combined.

3.4 Candidate Companions and Extragalactic Objects

Of the seven targets, only four showed candidate companions in their fields. The remaining targets did not show any other objects except WD 1257+278, which had a resolved galaxy in the background. Any extended objects were interpreted to be background objects and all point sources were flagged as potential companions. Where second epoch images were available with 2MASS or the POSS survey, they were used. Otherwise second observations were taken where possible. Each candidate with second epoch images was checked for common proper motion with the target WD by measuring the relative radius and pointing angle in degrees East of North of the companion. Extragalactic objects could potentially be of interest due to their proximity to a bright object that can be used for guiding in a laser AO system or multi-conjugate AO system.

To determine if an object had common proper motion with a target WD, we calculated the predicted motion of the WD on the sky based on its proper motion. When comparing possible companions with 2MASS or POSS data proper motion alone was sufficient to determine objects that were in the background. For WD 2326+049, WD 1620-391, and WD 0245+541, the annual parallactic motion of the star was also calculated for an added means of determining background point sources. Any object in orbit around a WD would also have to share both proper motion and annual parallactic motion.

It is important to adequately understand the errors in order to detect any possible proper motion of the background object or to determine how significant a measure of common proper motion is. The greatest sources of error are due to uncertainties in the parallax of the WD, proper motion, and centroiding errors in the PSF of the candidate. Centroiding errors for faint sources can be determined by looking at images in two filters for one of my fields that has a significant number of background sources. The field of WD 1620-391 has several background point sources that can be compared between filters and also two epochs. Comparing the difference of ~ 30 sources between the F110W and F160W filters of the observation sets of N8Q312010 and N8Q314010 yields a standard deviation between sources of ~ 10 mas, which I will adopt as my general centroiding error.

3.4.1 WD 2326+049

Because WD 2326+049 is a ZZ Ceti type pulsating white dwarf, its stable pulsation modes can be studied for time of arrival delays due to orbital motion. Since this WD has been studied for ~ 20 years, it is incredibly sensitive to low mass objects on the order of the mass of Jupiter. For this reason, I will focus on the detailed limits to planetary companions for this object in the range of semi-major axes from 0.1 AU to over 50 AU.

Table 3.3. Table of Extragalactic Objects

DSW #	RA	Dec	m_{F110W}	m_{F160W}	Notes
1	02 11 20.51	+39 55 14	21.36 ± 0.04		
2	12 59 45.63	+27 34 01	22.8 ± 0.1		$\sim 1.4''$ extent
3	23 28 47.96	+05 14 38	23.7 ± 0.2	22.1 ± 0.1	$0.23''$ aperture
4	23 28 47.67	+05 14 40	24.0 ± 0.2	22.8 ± 0.2	$0.23''$ aperture

3.4.1.1 A Candidate Planetary Companion

In my initial HST observations I discovered a promising candidate planetary companion. Figure 3.2 shows the discovery and resulting follow up images of the candidate. The point source is very faint, and was initially detected by eye by blinking F110W ROLL1 and ROLL2 images. In the HST images, the candidate is at an R and PA of $5.31 \pm 0.16''$ and $67.39 \pm 0.9^\circ$.

Several criteria had to be met for the point source to be a true detection and not a stray cosmic ray. These criteria included a marginal to significant detection at each roll angle and in each filter, similar flux within 1σ at each roll angle, and a significant detection in both the final images for each filter and the final summed image of both filters. In addition, the detections at each roll angle had to be separated by a distance consistent with the differential roll angle. In order to determine the significance I chose a 3 pixel radius circular aperture centered on the brightest pixel of the source in each image and summed the total counts in the aperture. To determine the sky level and the variation in the sky, an outer annulus with a radius of 10 pixels was chosen to surround the central aperture. Table 3.4 shows the significance of these detections in each of the mentioned frames. The F110W filters are the most marginal detections, at 2.5σ , with the F160W detection much more certain at $3-4\sigma$ for each frame. Detections in both total summed frames are significant at $\sim 5\sigma$.

The detected point source can only be considered a candidate planetary object if its F110W-F160W color is consistent with a planet and the probability of the random

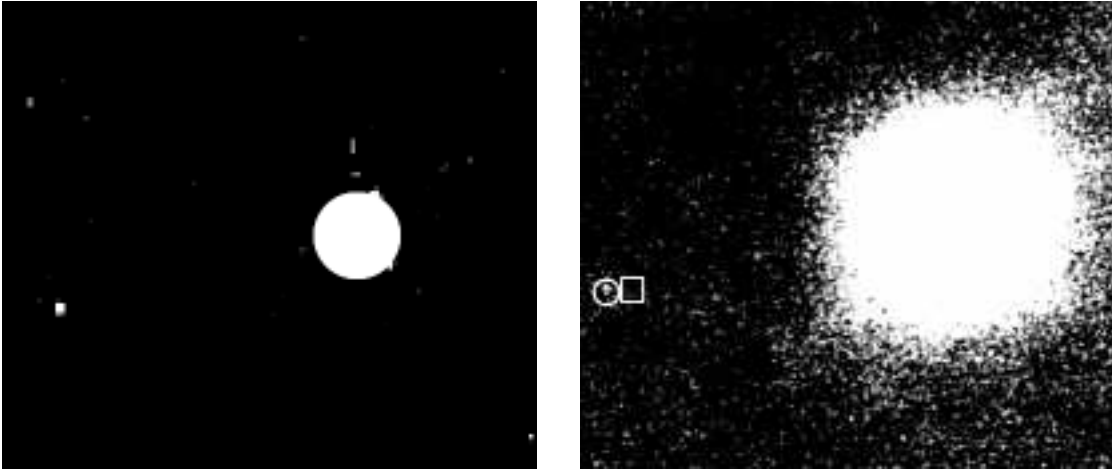


Fig. 3.2 (left) Discovery image of a candidate planetary companion in the HST F160W filter. (right) Second epoch image with Gemini, along with the predicted positions of co-moving (square) and non co-moving (circle) objects. The object is non co-moving and therefore in the background.

placement of a background point source is sufficiently low. Definitive confirmation of its association with G29-38 can be achieved with a test of common proper motion. I compared the object's magnitude and color with 1 and 3 Gyr isochrones. The F110W-F160W colors, within the photometric errors, are consistent with a 5-10 M_{Jup} object depending on G29-38's age. This color is not unique, as can be seen by a CMD of sources from the NICMOS ultra deep field parallels, which commonly have F110W-F160W colors of ~ 1 .

Figure 3.2 shows the final image of G29-38 and the detection of the candidate at the second epoch. It also shows the predicted positions of the candidate if it were an a) non co-moving background object and b) a co-moving, physically associated planet.

Our predicted positions were calculated by taking the measured radius and pointing angle of the candidate in the HST epoch and taking into account the proper motion of WD 2326+049 over the time period between the two observations. Error analysis for my predicted values were based on errors in centering, generated by the IRAF task PHOT and the reported errors for WD 2326+049's proper motion. Based on the measured proper motion of WD 2326+049 of -411 ± 0.01 mas/yr in RA and -263 ± 0.01 mas/yr in Declination (Pauli et al. 2003), I predicted a change of -367 mas and -235 mas, leading to $\Delta\alpha = (5.27 \pm 0.15)''$ and $\Delta\delta = (2.27 \pm 0.10)''$ for the non co-moving case. The position of the candidate differs by 18 mas in RA and 40 mas in Dec from the predicted non co-moving case. As can clearly be seen, the candidate is a background object that does not share WD 2326+049's proper motion. The errors in the calculation come primarily from the uncertainty in WD 2326+049's proper motion and uncertainties in the center measured. However, the position is well within the errors and shows no hint of its own proper motion.

Table 3.4. Photometry and Significance of Detections

Image	Significance	Magnitude
ROLL1(F110W)	2.5σ	-
ROLL2(F110W)	2.4σ	-
TOTAL(F110W)	4.6σ	$23.7\pm.2$
ROLL1(F160W)	2.9σ	-
ROLL2(F160W)	4.0σ	-
TOTAL(F160W)	6.6σ	$22.7\pm.2$
Gemini(H)	6.2σ	$22.6\pm.2$

The H band magnitude derived from its differential magnitude with WD 2326+049 gives an $H=22.6 \pm 0.2$, consistent with the F160W magnitude derived from the earlier observation.

Since it is a background object, it is useful to speculate what it might be. It is either a halo M dwarf, the nucleus of an Extremely Red Object (ERO) at moderate redshift, or a very high redshift quasar. If it is an M dwarf, comparison of its colors with current low mass stellar models shows they are most consistent with a metal rich halo star with a mass of $\sim 0.3 M_{\odot}$ at a distance of ~ 8 kpc, although a similar mass metal poor star, which would be a more plausible resident of the halo, is still just within my color errors (Baraffe et al. 1997, 1998). The HST colors of this object make it consistent with an ERO at a redshift of 2.5-3, although our object remains unresolved and would be ~ 900 pc wide at those redshifts, assuming the WMAP parameters (Spergel et al. 2003). Most EROs found to date are resolved (e.g, Corbin et al. 2000), and so this object would represent an unusual find. The flux densities measured for the candidate when K-corrected to high redshift (i.e. $z \sim 7$, $1.6\mu\text{m}$ becomes 2000 \AA) one finds luminosity densities of $\sim 10^{23} \text{ W Hz}^{-1}$, consistent with typical quasar luminosities.

3.4.2 WD 0208+395

Figure 3.3 shows two candidate objects, C1, C2, and a galaxy in the surrounding field. Since the candidates' separations were greater than a few arcseconds, I pursued a second observation with the Canada France Hawaii Telescope with the PUEO+KIR instruments. A second epoch image shows that both C1 and C2 are in the background. This result is discussed in detail in Chapter 4. If they had been associated, C1 would have been consistent with a 3 Gyr old $15 M_{Jup}$ brown dwarf and C2 would have been consistent with a $10 M_{Jup}$ planet.

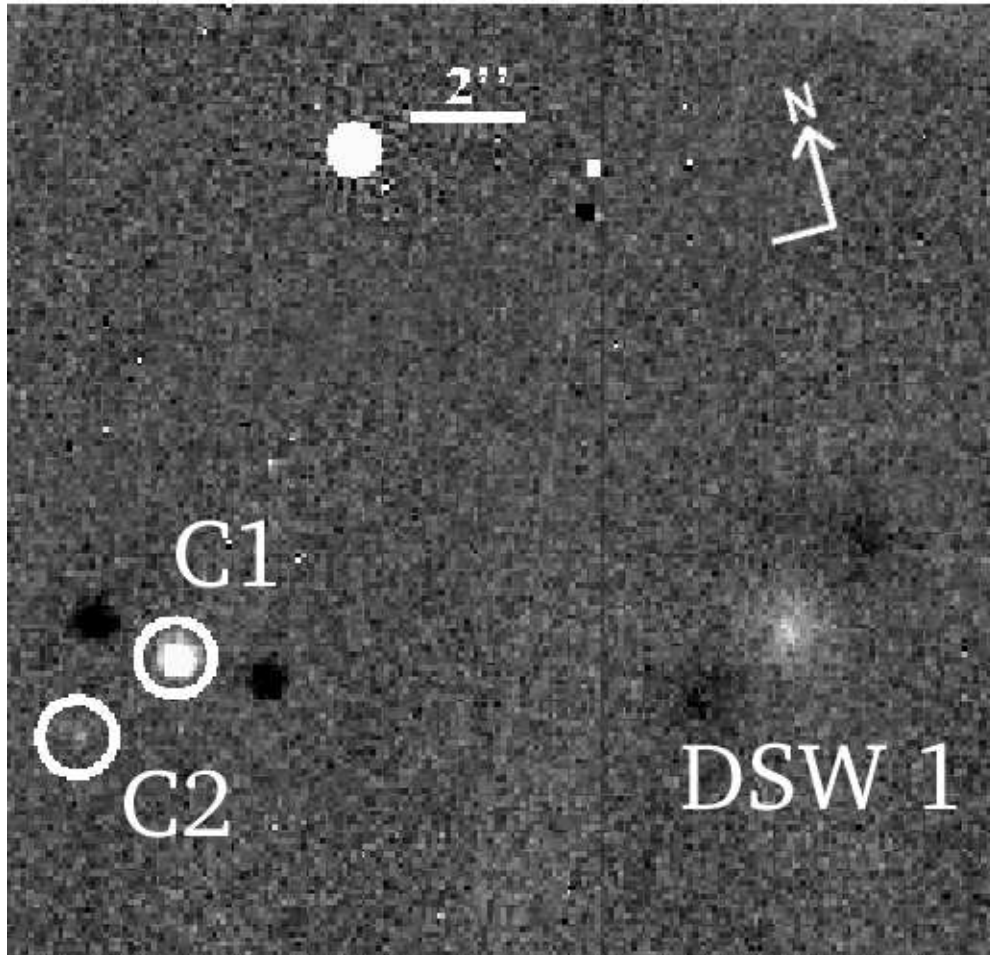


Fig. 3.3 Field of WD 0208+395 with its candidates. Candidates are circled, and the WD is masked to hide the systematic subtraction errors. A galaxy is detected in the lower right of the image.

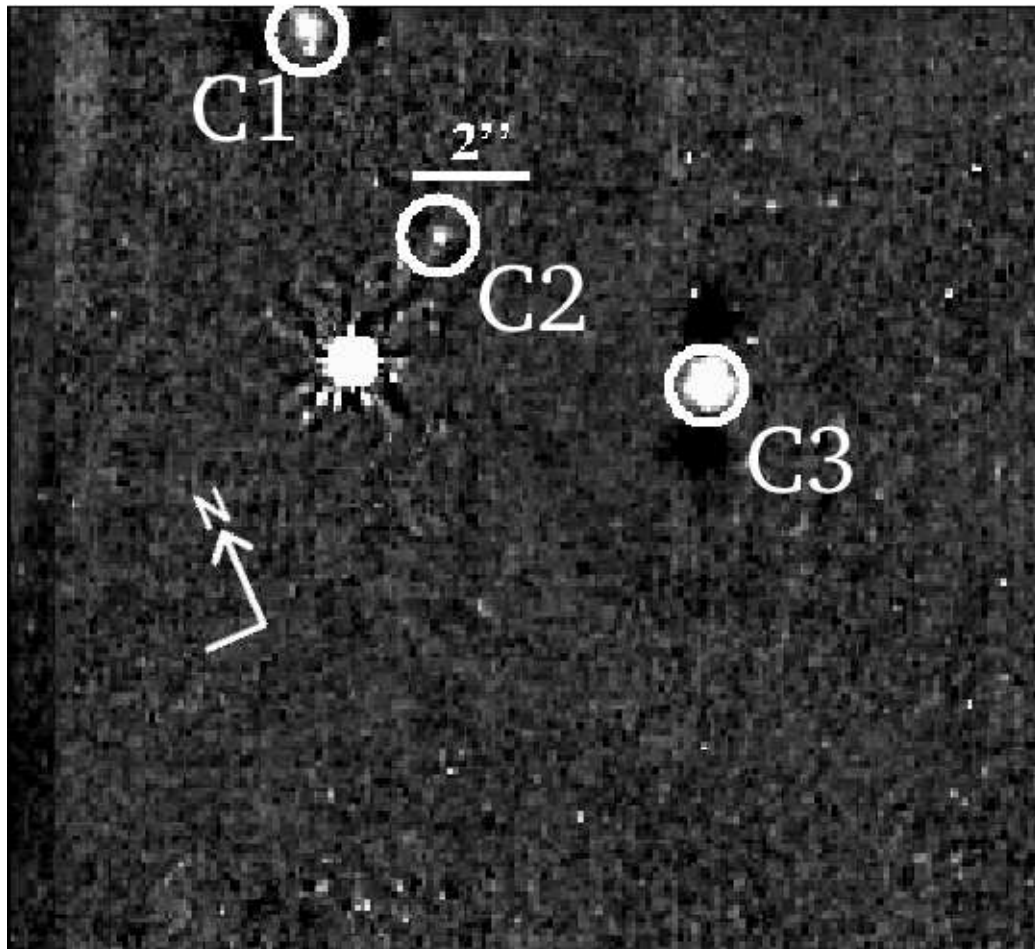


Fig. 3.4 Field of WD 0245+541 with its candidates circled.

3.4.3 WD 0245+541

This target was re-imaged \sim one year later due to a failed observation, (See table 3.1) which provided an ample baseline to test candidates for common proper motion. Figure 3.4 shows the surrounding area of WD 0245+541, along with three candidates in the field. C1 appears to be a binary object at a distance of $\sim 3''$ which in the second epoch image is clearly not co-moving. C2 is at a separation of $\sim 6''$ and 270° PA. Inspection of the POSS2 red image of this field clearly shows a point source at a separation consistent with this object being a background source. Finally, C3 has a separation of $(2.5 \pm 0.02)''$ and $348 \pm 1^\circ$ PA. WD 0245+541 has a predicted motion between the two epochs of -667 mas and -475 mas, leading to a predicted $\Delta\alpha = (0.17 \pm 0.12)''$ and $\Delta\delta = (2.94 \pm 0.12)''$ if C3 is non co-moving, compared to the observed $\Delta\alpha = 0.07''$ and $\Delta\delta = 2.86''$. The candidate does not have common proper motion, so it is a background object. The main source of error was in the reported proper motion, which had quoted errors of $0.1'' \text{ yr}^{-1}$ (Bakos et al. 2002). If C3 had been associated its F110W magnitude would have been consistent with an $18 M_{Jup}$ brown dwarf companion.

3.4.4 WD 1620-391

Unfortunately WD 1620-391 resides quite near the Galactic plane and as such has an extremely crowded field with ~ 36 sources of varying brightnesses, which can be seen in Figure 3.5. Any possible companion must be separated from background objects. A viable candidate in this field would have to be selected by an F110W-F160W color being consistent with a substellar object. Since most of these objects are background objects I must first see if there is any evidence to suspect that there would be a candidate in this field rather than assume that all sources are background objects. The number of objects as a function of distance should be $\propto r^2$ if the background distribution is truly random. A different distribution would be caused either by the presence of objects physically associated to the central white dwarf or due to physical associations among background stars, such as binaries or clustering. To test this I plotted the number of sources in the WD1620-391 field as a function of radial distance from the WD (see Figure 3.6). I compared this distribution to a pure r^2 distribution through means of a K-S test. I find that there is a 97% probability that the distribution is not based on the r^2 distribution mainly due to the ‘‘hump’’ of sources present close to the WD. I believe that those objects are viable candidates and that in a statistically significant way the distribution of sources with $r < 4''$ is fundamentally different that what would be expected. A caveat, however, is that since the WD is at a low galactic latitude the statistical test may merely be detecting some fundamental structure in the background sources rather than the presence of a candidate. Additionally, the scenario of Chapter 2 would predict more than one planet in the system to efficiently slingshot comets or asteroids to the surface of the white dwarf. Therefore, the potential exists that two planetary candidates could be present in this ‘‘hump’’ of sources $< 4''$.

Regardless, I have plotted all the detected sources in a CMD and compared them to a predicted isochrone of substellar objects in Figure 3.7. The WDs age is ~ 1 Gyr so I used the 1 Gyr models of Burrows et al. (2003) convolved with the HST filters. There are

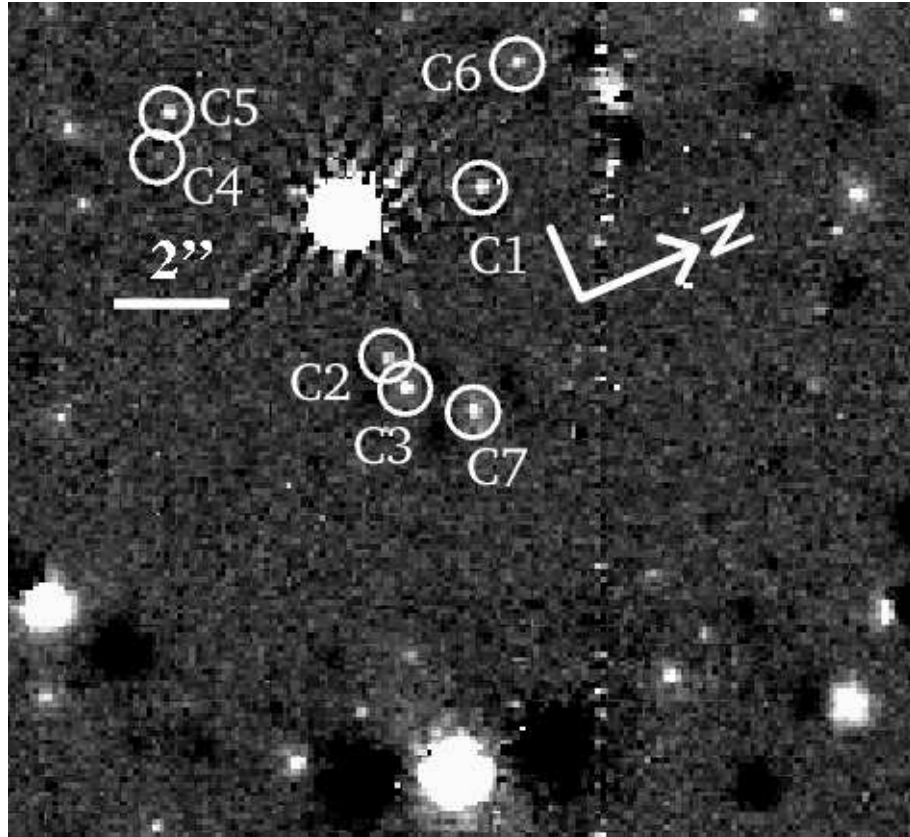


Fig. 3.5 Field of WD 1620-391 with its candidates. Each candidate that is circled is within $4''$ and has colors, consistent within the photometric errors, for a candidate planetary object.

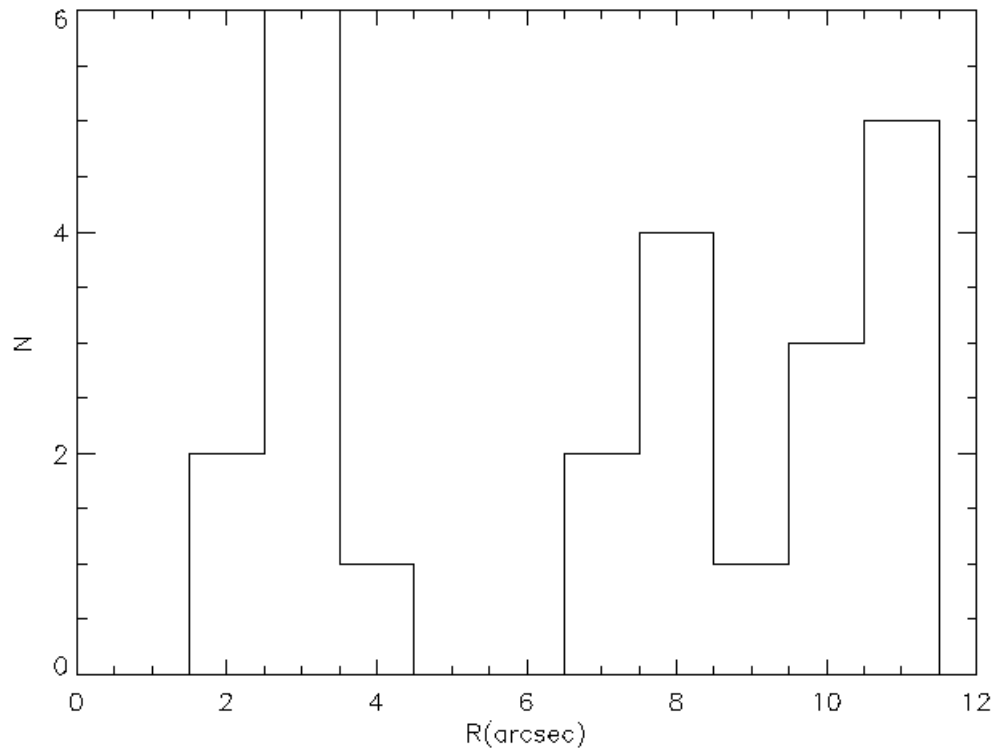


Fig. 3.6 Distribution of point sources as a function of distance around the white dwarf WD 1620-391.

some candidates that are within $4''$ and which have colors consistent within the errors to be a planetary candidate. Table 3.5 lists the candidates, their magnitudes in F110W and F160W. Every one of the candidates would be $\sim 5\text{-}6 M_{Jup}$ in mass if associated. This WDs proper motion is ~ 75 mas/yr in RA and ~ 0 mas/yr in Dec, (Perryman et al. 1997), so a second epoch image will be necessary in ruling out or in any of these sources. This however will require the high sensitivity and spatial resolution of HST due to the crowding in the field.

Table 3.5. Candidates around WD1620-391

Candidate	R	PA	F110W	F160W
C1	$2.22'' \pm 0.09$	$328.5^\circ \pm 0.7$	22.9	21.6
C2	$2.56'' \pm 0.13$	$262^\circ \pm 5$	22.9	21.8
C3	$3.10'' \pm 0.10$	$265^\circ \pm 3$	22.4	21.0
C4	$3.13'' \pm 0.14$	$141^\circ \pm 1$	23.9	23.0
C5	$3.24'' \pm 0.12$	$129.6^\circ \pm 0.8$	22.7	21.5
C6	$3.63'' \pm 0.17$	$27^\circ \pm 2$	22.5	21.2
C7	$3.91'' \pm 0.11$	$279^\circ \pm 2$	22.9	21.8

Unfortunately, our first image of WD 1620-391 is not sensitive enough to conclusively detect any of my candidate companions. Six stars were bright enough to use as a background grid of reference compared to WD 1620-391's position. Of these six, five were distinct point sources. The sixth appears to be extended, either because it has a disk or because it is a binary. When comparing the relative position between these presumably stationary objects in six months and WD 1620-391, I measure a change in RA of 204 ± 10 mas and in declination of 16 ± 10 mas. I derived the error based on the standard deviation of the individual measurements from the mean. Taking into account WD 1620-391's parallax motion during this period, one would expect a motion of 230 mas in RA and 28 mas in declination assuming WD 1620-391's reported parallax of 78.85 mas (Perryman et al. 1997). Subtracting this motion leaves 26 ± 10 mas and 12 ± 10 mas from the measured motion with my reference stars. This good agreement with the predicted position suggests that I can detect common proper motion and common parallactic motion in a future epoch with HST and these reference stars.

3.5 Limits to Companions

The main goal of this search was to detect candidate companions, but in addition, limits to the detection of such companions is also important for understanding the true nature of DAZ WDs, as well as the process of planet and brown dwarf formation around

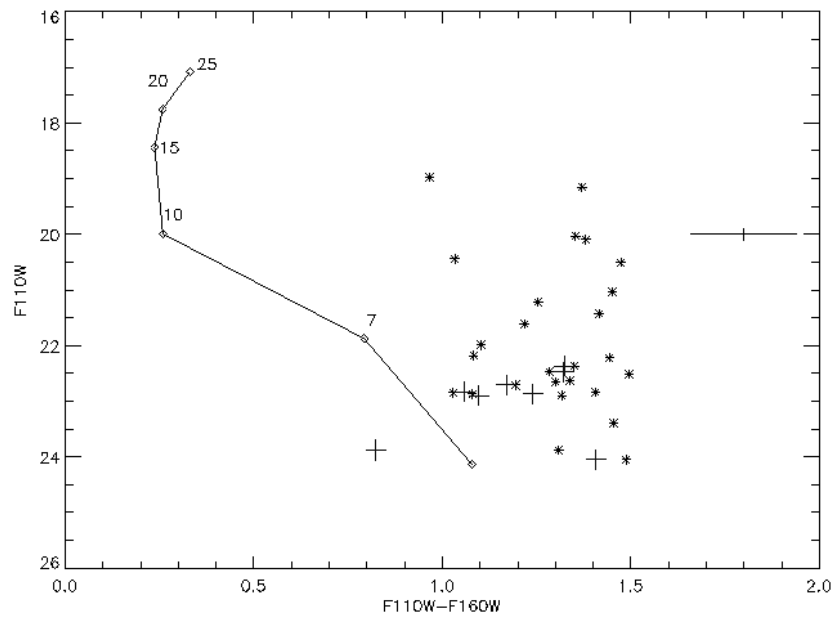


Fig. 3.7 Color magnitude diagram of sources near the white dwarf WD 1620-391. Overplotted is an isochrone of 1 Gyr substellar models from Burrows et al. (2003) convolved with HST filters at 12 pc. Thick crosses are sources $<4''$ away.

intermediate mass stars. To this end, we quantify my sensitivity to companions I could have seen in order to determine the frequency of high mass planets and brown dwarfs.

3.5.1 Limits from 2MASS Photometry

While direct imaging is most sensitive to companions $>0.9''$ unresolved companions could still be present for some of these targets. In order to rule out companions at separations where imaging or PSF subtraction could not resolve them, I turn to the near-infrared fluxes of these objects provided by near-IR photometry, such as from 2MASS (Cutri et al. 2003). Looking in the near-IR can facilitate the discovery of cool objects around WDs (Probst & Oconnell 1982; Zuckerman & Becklin 1992; Green et al. 2000).

My strategy was to take model values reported in the literature, generate predicted 2MASS J, H, and Ks magnitudes by using the models of Bergeron et al. (1995) and comparing J_{th} , H_{th} , and K_{th} with the observed magnitudes of the WDs. For my sample of white dwarfs I took model values of T_{eff} , $\log g$, and the mass from Liebert et al. (2004), Bergeron et al. (2001), and Bragaglia et al. (1995).

To compare the predicted magnitudes to those observed I took the difference of the predicted magnitudes in the 2MASS filter system J_{th} , H_{th} , and $K_{s(th)}$ and the observed magnitudes J, H, and K_s . A significant positive value would indicate an excess due to either an unseen companion or a dust disk, while a significant negative value would indicate an anomalous paucity of flux. While we used the results of Liebert et al. (2004) for two of my white dwarfs for the rest of my targets I used the Bergeron et al. (2001) and Bragaglia et al. (1995) samples since they provide atmospheric parameters for the remaining five white dwarfs. In general, I compared J magnitudes since WD 2326+049 has an infrared excess due to a dust disk at wavelengths longer than $\sim 1.6 \mu\text{m}$. Excesses in J tend to be more sensitive because J band photometric errors are smaller in 2MASS. For the rest of the targets I also checked to see if there were excesses in any of the other bands or for other targets in the sample. An excess was considered significant if it was greater than three times the measured scatter of a sample and if it was present in more than one filter.

I tested the accuracy of the three samples of WD parameters to reliably report a 3σ excess limit. I first examined the Bergeron et al. (2001) sample, which includes WD 0208+395, WD 0245+541, WD 0243-025, and WD 1257+278. Of the 150 white dwarfs I chose 146 of the sample that had reliable photometry from Bergeron et al. (2001) and converted their MKO magnitudes to 2MASS magnitudes¹ to compare with my predicted magnitudes.

I neglected any object with an excess $> 3 \sigma$ and recalculated the scatter in expected minus observed magnitudes, repeating the process three times. I ensured that the median values of the differences were consistent with zero. From the 146 WDs I find that the 1σ error in total of J, H, and Ks are 0.04, 0.04, and 0.05 mag. One important note is that Bergeron et al. (2001) used their JHK photometry to help fit several of the parameters that I used to generate my theoretical magnitudes, namely $\log g$ and T_{eff} . For this reason I had to be more careful interpreting these limits because it is possible the

¹http://www.ipac.caltech.edu/2mass/releases/allsky/doc/sec6_4b.html

presence of a companion was “fitted out”. In this case I am placing limits to what kind of excess would have been detected by the models, rather than extrapolating from the models and looking for excesses. No objects in this sample showed a significant excess.

Table 3.6. 2MASS Photometry of PG WDs

PG	J_{th}	H_{th}	$K_{s(th)}$	J	H	K_s
0017+061	15.33	15.49	15.56	13.74	13.19	12.98
0205+134	15.45	15.63	15.72	12.80	12.20	11.96
0824+289	14.95	15.13	15.22	12.42	11.80	11.65
1026+002	14.29	14.41	14.46	11.75	11.22	10.94
1033+464	14.93	15.08	15.17	12.56	12.03	11.75
1234+482	15.14	15.32	15.40	14.98	14.96	14.94
1335+369	15.03	15.15	15.20	13.29	12.92	12.85
1658+441	15.26	15.40	15.50	15.44	15.53	15.05

For WD 2326+049 and WD 1337+705 I took the sample of Liebert et al. (2004) which is a study of DA WDs from the Palomar-Green survey of UV excess sources. Of the 374 white dwarfs I chose the brightest 72 of the sample that had a $J < 15$, had unambiguous sources in 2MASS, and had reliable photometry, i.e those objects that had quality flags of A or B in the 2MASS point source catalogue for their J magnitudes.

If there were a significant number of excesses to these stars then the error will be overestimated. Since I cannot *a priori* separate this effect without foreknowledge, I’ve assumed that there are not a significant fraction of WDs with excesses. As an added check, I neglected any object with an excess $> 3\sigma$ and recalculated the scatter in observed minus expected magnitudes and iterated this process three times.

After determining the standard deviation of the sample, I found that 1σ errors for the sample in the J, H, and K bands were 0.07 mag, 0.1 mag, and 0.15 mag, respectively. I treated any excesses greater than 3σ as significant, though if an excess was only present in one band I marked this as a tentative detection. One exception is WD 2326+049 itself, which showed only a 3.5σ excess in the K_s band due to its dust disk, which has been amply confirmed in the past.

Seven objects in my sample showed significant excesses in at least two filters and one object showed a significant excess only in the K_s band. These results are shown in Table 3.6. Of the eight objects, 5 were previously known. PG 1234+482, PG 1335+369, and PG 1658+441 are new. Care was taken to ensure that the coordinates of new excess candidates in the 2MASS fields were correct and that their optical photometry was consistent both with that reported in Liebert et al. (2004) and with the distance assumed in the modeling. The absolute magnitudes of candidate excess companions were calculated by taking the excess flux and using the distance derived from models of the

WDs. A spectral type for each excess object was either taken from the literature or compared to nearby M and L dwarfs with known distances (Henry et al. 1994; Leggett et al. 2001). The results are presented in Table 3.7. The spectral types we've determined are rough and need to be confirmed through spectroscopic follow-up or high spatial resolution imaging.

PG 1234+482 and PG 1658+441 both were previously studied in the J and K bands by Green et al. (2000) for excesses. None were reported for either of these objects. Based on my analysis, PG 1234+482 has significant excesses in the H and Ks filters. Green et al. (2000) reported a similar K magnitude as that reported in 2MASS but due to larger errors in their photometry, measured it as a marginal excess of $\sim 1.3\sigma$. PG 1658+441 shows only an excess in the Ks 2MASS filter, which is contradicted by the infrared photometry taken in Green et al. (2000). Their measured magnitude in K differs by ~ 0.6 mag from 2MASS, with the 2MASS measurements having a higher reported error. Based on this uncertain photometry, the excess could be due to a mid L dwarf—the J-K color of such an object would result in a negligible excess in J and an observable excess in K_s (Leggett et al. 2001). This would be an exciting discovery, if confirmed, as only two substellar objects are known to orbit nearby white dwarfs (Becklin & Zuckerman 1988; Farihi et al. 2003) PG 1658+441 has been selected and observed for Program 10255, an HST snapshot program to resolve close WD+M dwarf binaries. If an L dwarf is present in an orbit greater than a few AU, it should be resolved with those observations.

For WD 1620-391, I needed to use the sample in Bragaglia et al. (1995), using ~ 35 of the 50 WDs modeled in that work. I again picked WDs with $V < 15$, reliable 2MASS positions, and reliable photometry in the three bands. Six white dwarfs had poor photometry or incorrect distance moduli, but these errors were corrected. The final errors were calculated, resulting in 1σ errors of 0.09, 0.08, 0.15 mag for J, H, and Ks respectively. Two WDs remained with significant excess, WD 1042-690, and WD 1845+019. WD 1042-690 is a known binary system with a dM companion, and WD 1845+019 does not currently seem to be a candidate for an excess. However, its position in both the POSS and 2MASS plates based on the position given by Lanning (2000) shows that it is blended with another point source. Inspection of the POSS and 2MASS plates leaves it ambiguous whether this barely resolved object (separation $\sim 3''$) is co-moving or not, so we mark this as a potential common proper motion WD/dM pair.

Table 3.8 shows the expected 2MASS magnitudes based on the model values, and the observed magnitudes of my target white dwarfs. All of my targets fall within $1-2\sigma$ of my expected values for all three filters, with the exception of WD 2326+049, as mentioned above.

Since none of my targets have significant excesses, I can use the 3σ limits in J to place upper limits to unresolved sources. I took the predicted J magnitudes from substellar atmosphere models, corrected for distance modulus, calculated the excess, and compared it to my sensitivity limit (Baraffe et al. 1998, 2003). Table 4.4 shows the unresolved companion upper limits for each target. Any companion with a mass beyond the hydrogen burning limit would have been detected for all of the target WDs.

Table 3.7. Magnitudes and Spectral Types of Excess Candidates

PG	M_J	M_H	M_{K_s}	Sp Type	Reference
0017+061	8.98	8.29	8.05	M5V	1 ^a
0205+134	6.46	5.81	5.56	M3.5V	2
0824+289	6.90	6.24	6.09	dC+M3V	3
1026+002	8.96	8.38	8.09	M5V	1
1033+464	8.15	7.56	7.26	M4V	1
1234+482	11.31	10.3	10.3	M8V	-
1335+369	9.30	8.84	8.77	M5.5V	- ^b
1658+441	-	-	14.1	L5	- ^b

References. — (1) Zuckerman & Becklin (1992) (2) Allard et al. (1994) (3) Green et al. (2000)

^a Zuckerman & Becklin (1992) did not estimate spectral type, estimates taken from 2MASS magnitudes of nearby M dwarfs listed in Henry et al. (1994)

^bThis work used 2MASS magnitudes of nearby M dwarfs from Henry et al. (1994) and nearby L, T dwarfs from Leggett et al. (2001) to determine rough spectral types

Table 3.8. Comparison of Predicted vs. 2MASS Photometry

WD	J_{th}	H_{th}	$K_{s(th)}$	J	H	K_s
0208+396	13.74	13.61	13.57	13.76	13.66	13.61
0243-026	14.65	14.49	14.43	14.67	14.50	14.49
0245+541	13.86	13.61	13.47	13.86	13.67	13.58
1257+278	14.95	14.89	14.88	14.95	14.92	14.89
1337+701	13.23	13.36	13.41	13.25	13.36	13.45
1620-391	11.53	11.66	11.74	11.58	11.71	11.77
2326+049	13.13	13.19	13.22	13.13	13.08	12.69

3.5.2 Imaging

Schneider & Silverstone (2003a) showed a reliable way to determine the sensitivity of an observation with NICMOS, given the stability of the instrument. Artificial “companions” are generated with the HST PSF simulation software TINYTIM². These companions are inserted into the observations and used to gauge sensitivity. I adopted this strategy for my data as well, considering an implant recovered if its flux in a given aperture was at a S/N of 5. Sample implants were looked at by eye to verify that an observer could easily distinguish the implant. The faintest structures can be detected at S/N levels less than 5 due to the roll angle change. Blinking two roll images often can bring fainter structures out. The implants were normalized so that their total flux was equal to 1 DN/s, which can then be converted to a flux in Jy or a Vega magnitude by multiplying by the correct photometry constants given by the NICMOS Data Handbook.

An implant was placed in my ROLL1 images and then identical implants were inserted 10 degrees offset in my ROLL2 images. Two difference images were created and then rotated and combined for maximum signal to noise. Figure 3.8 shows the final product of the above process. In this figure, an implant with $m_{F160W}=22.2$ has been implanted, offset, and then roll combined, creating the distinctive positive PSF surrounded by two negative PSFs separated on each side by 10 degrees.

For my Gemini data we used the PSF of WD 2326+049 as a reference for the implant. The implant was normalized to a peak pixel value of one. Scaled versions of the implants were then used to determine sensitivity. The relative flux of the companion with respect to the host star was measured and a corresponding MKO H magnitude was derived from the 2MASS H magnitude to give a final apparent magnitude sensitivity.

My resulting sensitivity plot for WD 2326+049 in Figure 3.9 shows the apparent limiting magnitudes in my search from 0.2'' to 5''. These results represent the deepest and highest contrast images taken around a white dwarf. They also represent the most sensitive direct imaging search for substellar companions in orbit around a star to date. Beyond 1'' my sensitivity was limited not by the contrast of HST but by the limited exposure time. For my other DAZ targets, my sensitivity extended from 0.9'' to 5''.

It is useful to convert the sensitivity in the observed magnitudes or fluxes into a corresponding companion mass. This is a more complex proposition with substellar companions for a variety of reasons. Since most substellar companions do not have long term energy sources, the luminosity of a brown dwarf or planet that is not significantly insolated is dependent both on mass and age. In the present situation I can estimate the age of the system based on the properties of the host star. For my current sensitivity calculation I chose the most recent models published by Burrows et al. (2003) and Baraffe et al. (2003), though as these models change and are refined, my limits will change as well. These models are consistent at > 1 Gyr to within ~1 magnitude of each other in the J and H bands, but are difficult to compare in the NIR due to the presence of H₂O molecular absorption that can cause variations in predicted magnitudes in different systems (Stephens & Leggett 2004). The Baraffe et al. (2003) magnitudes are all predicted in the CIT system, while Burrows et al. (2003) make their synthetic

²<http://www.stsci.edu/software/tinytim/tinytim.html>

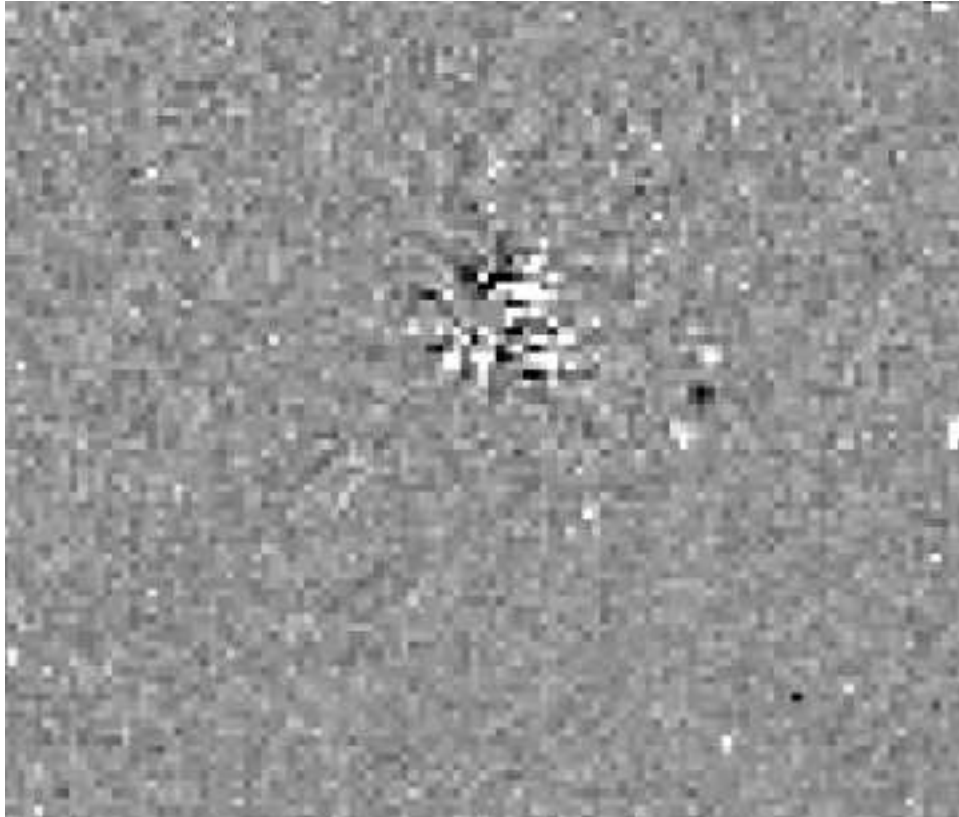


Fig. 3.8 Sample sensitivity test image. WD 2326+049 has an implanted artificial companion at a separation of $1.9''$ and a PA of 204° with respect to North in the image. North is rotated 43° counterclockwise from up in the image. The implant has an F160W magnitude of 22.2 with a S/N of 9 for a 4 pixel diameter photometric aperture.

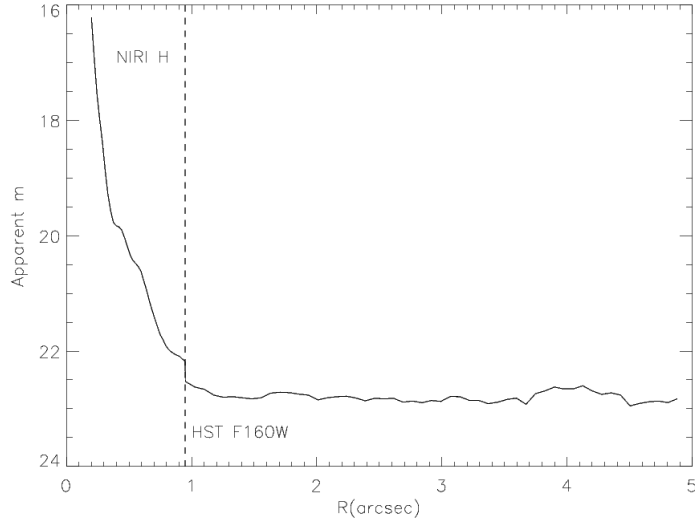


Fig. 3.9 The final azimuthally averaged 5σ sensitivity curve of my HST and Gemini images. At separations $< 1''$, the Gemini PSF still had significant flux. To ensure that my sensitivity reflected actual detectability, I used a 10σ limit in the inner regions.

spectra directly available. Both sets converge to within a magnitude of each other in the J, H, and K filters, but in general the predictions by Burrows et al. (2003) are fainter. For that reason we use the Burrows et al. (2003) models for most of my calculations in this Section. In Section 3.5.1 I instead use the Baraffe et al. (2003) models since they extend to higher mass.

Most models are for ground based J, H, and K filters. These filters were originally designed to avoid atmospheric windows of high near-IR absorption which is irrelevant for HST filter design. The wideband NICMOS filters vaguely resemble their ground-based counterparts, but possess significant differences in the case of objects that have deep molecular absorption. To adequately understand what type of companions one is sensitive to, it is necessary to take flux calculations from the models and convolve them with the waveband of interest to get a predicted absolute magnitude for the HST filters:

$$M_x = -2.5 \log \left(\frac{\int A_\lambda F_\lambda d\lambda}{\int A_\lambda d\lambda} \right) + 2.5 \log Z_{\text{vega}} \quad (3.1)$$

where A_λ is the transmission function of the filter, F_λ is the flux of the putative companion, and Z_{vega} is the Vega magnitude zeropoint as described by the NICMOS Data Handbook.

Figure 3.10 shows a sample M_{F110W} vs. $M_{F110W} - M_{F160W}$ color magnitude plot for substellar objects with ages of 1 Gyr and 3 Gyr as a function of their mass (Burrows et al. 2003). A comparison with Burrows et al. (2003)'s plots show that the predicted J and F110W magnitudes differ by slight amounts. It should also be noted that these

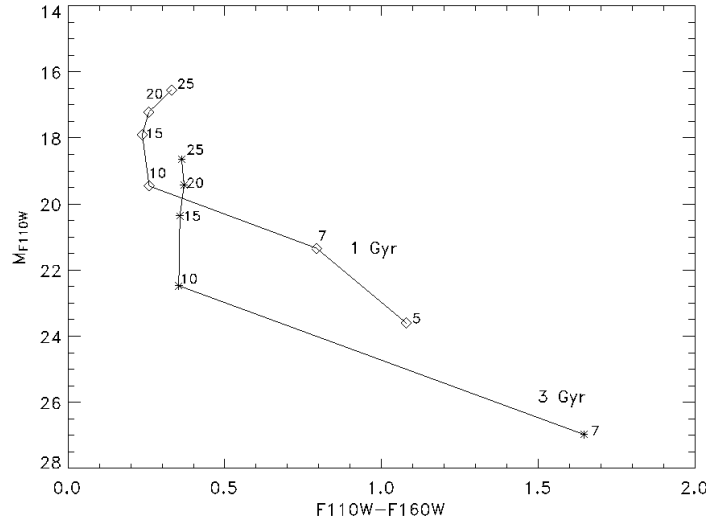


Fig. 3.10 Isochrones of substellar objects with a total age of between 1 and 3 Gyr in NICMOS filters. Small numbers correspond to masses in units of M_{Jup} . I used the spectral models of Burrows et al. (2003) and convolved them with the NICMOS filters.

predicted fluxes are based upon a completely isolated object that is not experiencing any insolation from its host star. Companions around WDs would have been insolated by their parent star during its main sequence lifetime. However, insolation calculations show that this would be insignificant for well separated companions (Burrows et al. 2004). The largest insolation would occur during the red giant branch (RGB) and asymptotic giant branch phases (AGB) of post main sequence evolution; but a quick calculation of the equilibrium temperature shows the temperature at 5 AU during these phases would be less than the temperature experienced by HD 209458B, the Jovian planet in a 0.03 AU orbit around a main sequence star.

To get a final prediction of the types of companions to which the observations were sensitive requires a fairly accurate estimate of the WD's total age. This is the sum of its cooling age and its main sequence lifetime. Estimates of the main sequence lifetime can be taken from the initial to final mass ratio relationship between WDs and their progenitor stars (Weidemann 2000). Cooling times can be derived by modeling. Liebert et al. (2004) gives WD 2326+049's mass and cooling age as $0.7 M_{\odot}$ and 0.6 Gyr. Using a theoretical version of the initial-to-final mass function, $M_i = 10.4 \ln(M_{WD}/M_{\odot})/0.49 M_{\odot}$ one derives an initial mass of $3.7 M_{\odot}$ (Wood 1992). The main sequence (MS) lifetime can be estimated by $10(M/M_{\odot})^{-2.5} Gyr$, which gives an MS lifetime of 0.4 Gyr and thus a total age of 1 Gyr (Wood 1992). There is some dispute as to the precise mass of WD 2326+049 from pulsational studies. They predict a mass of $0.6 M_{\odot}$, leading to an age closer to 2-3 Gyr if one assumes that the cooling time remains the same or is a bit longer (Kleinman 1998). I will place my limits based on ages of 1 and 3 Gyr, thus spanning the possible uncertainty in WD 2326+049's age. However, it is also possible

Table 3.9. Upper limits to Companions

WD	Excess Limit (J)	Mass (M_{Jup})	Sensitivity $> 0.9''$ (F110W)	Mass (M_{Jup})
0208+396	15.5	48	23.9	10
0243-026	16.4	51	24.1	10
0245+541	15.6	53	23.5	18
1257+278	16.8	40	23.8	14
1337+701	14.5	70	23.4	14
1620-391	12.3	61	22.9	7
2326+049	14.4	39	23.3	6

that younger planets may be present, such as from a recent collision between two planets (Debes & Sigurdsson 2002) or from a companion formed in an AGB outflow (Livio et al. 1992).

Figure 3.11 shows an example of the azimuthally averaged 5σ sensitivity for WD 0208+395. With a total estimated system age of ~ 3 Gyr for WD 0208+395, I overplot the lowest companion mass detectable, using the models of Burrows et al. (2003). Table 3.9 has the mass limits for each WD for separations $> 0.9''$.

3.5.3 Limits from Pulsational Studies

For WD 2326+049, I also have the advantage of limits to companions due to studies of its pulsations. WD 2326+049 has often had claims of the presence of possible companions. Its infrared excess was originally attributed to a brown dwarf companion, while radial velocity and pulsational timing hinted at the presence of either a low mass stellar companion or a massive black hole, all of which were shown to be spurious by more careful, longterm pulsational timing (Kleinman et al. 1994).

Pulsational timing is done in a similar fashion to pulsar timing, in that phase changes of the observed minus calculated (O-C) pulse arrival times can be used to calculate a Keplerian orbit to a perturbing body. For pulsating white dwarfs the technique requires the identification of a stable pulsational mode and measuring its arrival time very precisely. Measuring higher derivatives of the period change can also help to further constrain the keplerian parameters of a companion orbit before it has completed a full revolution. This technique for pulsars has been remarkably effective at finding “oddball” planets, such as the first extrasolar planets ever discovered, and a Jovian mass planet in the metal poor M4 cluster (Wolszczan & Frail 1992; Sigurdsson et al. 2003).

Long baseline timing studies of pulsating white dwarfs can produce very stringent limits to the types of companions orbiting them, down to sub-Jovian masses. They are limited by the timescale of observations and probe the inner-most separations. In

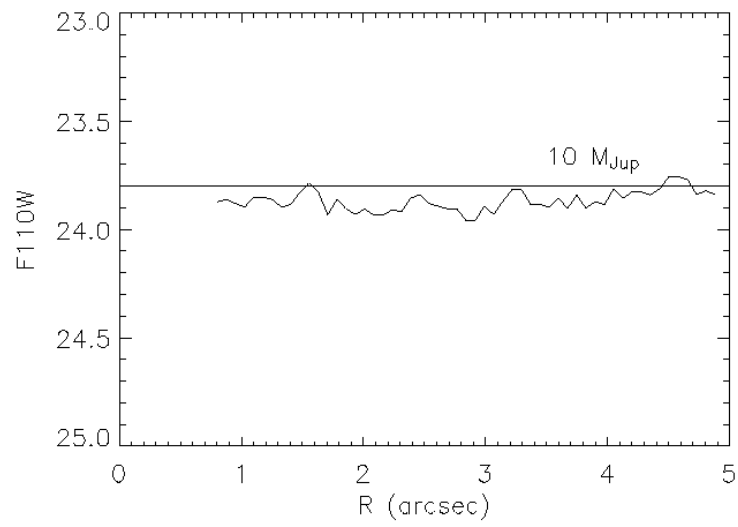


Fig. 3.11 Sensitivity at 5σ to point sources in F110W around WD 0208+395. The WD's F110W magnitude is ~ 13.8 , giving a contrast of 10 magnitudes at $1''$. Overplotted is the magnitude of a $10 M_{Jup}$ planet 3.2 Gyr old at the distance of WD 0208+395 from the models of Burrows et al. (2003).

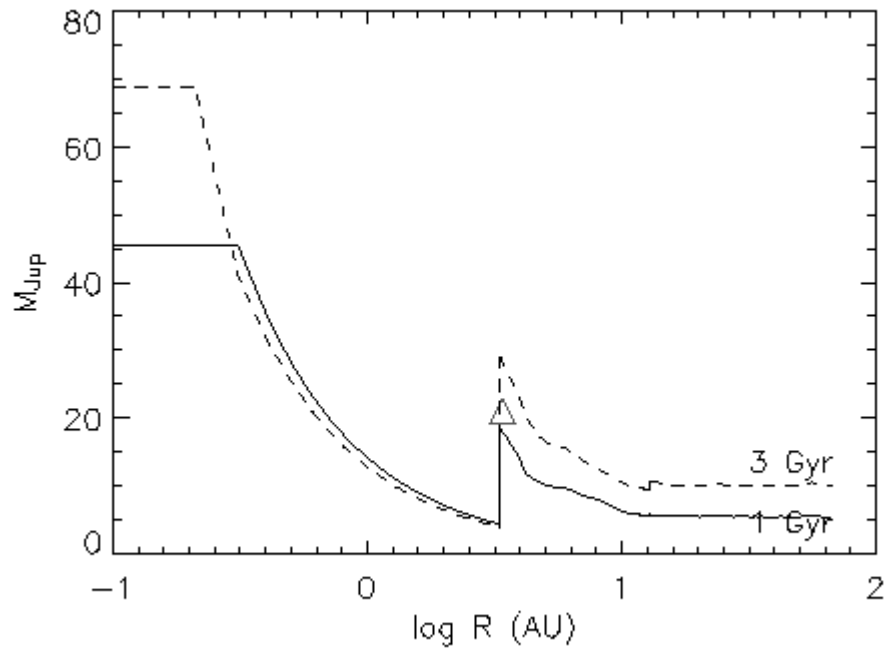


Fig. 3.12 Combined limits to substellar objects around WD 2326+049 from a combination of 2MASS photometry, pulsation studies, and my high contrast imaging. The solid and dashed lines show the limits to the age of WD 2326+049 and the triangle shows the expected minimum mass of a companion tentatively discovered by pulsational studies.

this sense pulsational timing is generally complementary to direct imaging searches, the combination of the two providing a comprehensive and sensitive method for searching for extra-solar planets.

Kleinman et al. (1994) demonstrated that for WD 2326+049, perturbations on the order of 10s or greater could have been detected around the white dwarf. In fact, a trend was discovered in their data that had an amplitude of 56s and a possible period of 8 years. This was a tentative detection given the possibility of the mode that they used being unstable or slowly varying. However, one can estimate based on WD 2326+049's parameters how massive such a companion would be and what its semimajor axis would be. The minimum mass derived was $21 M_{Jup}$ with a semi-major axis of 3.4 AU assuming WD 2326+049 has a mass of $0.6 M_{\odot}$. Assuming a higher mass does not significantly change these values.

If this trend is not due to a companion, the pulsational studies had an estimated noise of ~ 10 s. Using this limit, one can calculate the limits to detecting other types of companions at different orbital separations sampled by these observations.

Figure 3.12 shows the combination of the pulsational timing limits based on the 10s noise limit and my observational data. At separations less than 0.5 AU, the limit is determined by our 2MASS limit. Between 0.5 AU and 3 AU, the limits are determined by the pulsational studies. Beyond 3 AU, the limits are determined by my imaging. Overplotted is the separation and mass of the possible companion detected in the pulsational timing. my observations discount the possibility of the tentative companion, if the total age of WD 2326+049 is closer to 1 Gyr. If it is older, I can constrain the inclination of this companion's orbit to be $>60^{\circ}$ from face on based on my detection limit of $30 M_{Jup}$ if WD 2326+049 is closer to 3 Gyr. Inspection of the limits shows that any companion $> 12 M_{Jup}$ is ruled out for separations between ~ 1 AU and 3 AU and > 5 AU if G 29-38 is closer to 1 Gyr. All but planetary mass objects are ruled out for a good portion of the discovery space around this white dwarf. Further observations, such as sensitive radial velocity variations would provide a stronger limit to close in companions than what is possible with 2MASS.

Chapter 4

Limits to Substellar Objects Around Nearby White Dwarfs

4.1 Introduction

In this Chapter, I search for planets and brown dwarfs with imaging using the PUEO/KIR instruments on the Canada France Hawaii Telescope (CFHT). This initial survey is intended to demonstrate that useful detections of substellar and planetary objects are possible with a large enough sample of nearby white dwarfs from the space and from the ground.

In Section 4.2 I present the observations I performed. In Section 4.3 I present the candidate companions I have discovered as well as any background objects that may be present. Several of these companions can be ruled out through the use of second epoch observations. In Section 4.4 I determine the limits to companions that I could have detected.

Table 4.1. List of WD Targets

WD	V	M_f (M_\odot)	M_i (M_\odot)	T_{eff} (K)	D (pc)	Total Age (Gyr)	References
0208+396	14.5	0.60	2.1	7310	16.7	2.9	1
0501+527	11.8	0.53		61000	68.8		
0912+536	13.8	0.75	4.4	7160	10.3	2.8	1
1055-072	14.3	0.85	5.7	7420	12.2	3.0	1
1121+216	14.2	0.72	4.0	7490	13.4	2.2	1
1213+528	13.3	0.64	2.8	13000	38.6	1.0	2,3
1334+039	14.6	0.55	1.2	5030	8.2	10.2	1
1626+368	13.8	0.60	2.1	8640	15.9	2.58	1
1633+433	14.8	0.68	3.4	6650	15.1	2.75	1
1633+572	15.0	0.63	2.6	6180	14.4	3.76	1
1953-011	13.7	0.74	4.3	7920	11.4	1.89	1
2140+207	13.2	0.62	2.4	8860	12.5	2.12	1
2246+223	14.4	0.97	7.1	10330	19.0	1.69	1
2341+321	12.9	0.57	1.6	12570	16.6	3.44	4

4.2 Observations

Observations of all the white dwarfs were taken during three trips to the Canada France Hawaii Telescope—the first on October 11-14 2003, the second on April 1, 2004, and the final on September 29, 2004. Observations were taken primarily in the J band on the first run and in the H band on the second and third run using the KIR instrument in conjunction with PUEO, the wavefront curvature AO system (Rigaut et al. 1998). Table

4.1 shows the list of targets including their V magnitudes, masses, primordial masses, estimated ages, effective temperatures, and distances. The mass, T_{eff} , and cooling age came from either Bergeron et al. (2001) or Liebert et al. (2004), with the exception of WD 0501+527. WD 0501+527's parameters come from Finley et al. (1997). The primordial mass (M_i) was calculated by a theoretical initial to final mass function given by $M_i = 10.4 \ln(M_{WD}/M_{\odot})/0.49 M_{\odot}$ (Wood 1992). The main sequence lifetime of the star was determined by $t_{MS} = 10M_i^{-2.5}$ Gyr (Wood 1992). Since these relations only work well for $M_{WD} > 0.54 M_{\odot}$, WD 0501+527's total age is unknown.

The very advantage these targets have for detecting planets is almost completely negated by the fact that most current AO systems cannot reliably correct atmospheric turbulence for such faint objects. With most large telescope AO systems requiring targets with $V \lesssim 13$, most of these targets would have to be imaged without the help of AO. However, the curvature wavefront sensor AO system of PUEO provides a heightened advantage by being able to guide on targets with $V \lesssim 16$, allowing most nearby WDs to be accessible to AO correction (Rigaut et al. 1998). AO correction is particularly useful for gaining spatial resolution as well as sensitivity against the near IR background. These two benefits allow the more modestly sized CFHT to compete realistically with larger telescopes in this area without AO, as well as with space based Near-IR imaging.

Table 4.2 shows my list of observations as well as total integrations for each target WD. Most objects were observed for ~ 1 hr using 240s subexposures that were dithered in a $5''$ five point grid pattern for background subtraction. This left a $\sim 20'' \times 20''$ field of high sensitivity. WD 1213+568 and WD 1633+572 had shorter total exposure times, with 15 minutes and 16 minutes respectively. WD 0208+396, WD 0501+527, and WD 2341+321 had longer integrations of 90 minutes, 66 minutes, and 78 minutes, mainly due to dither patterns being interrupted by weather. Objects that threatened to saturate the detector had shorter subexposures. This was the case for WD 1213+568 and WD 2140+207 whose subexposures were 60s and 120s respectively. Flatfields were taken at the beginning of each night.

As can be seen from Table 4.1, my targets ranged in brightness, which in turn affected the performance of the AO correction. Correction deteriorated towards dawn on my second run as the sky background increased, and weather conditions varied throughout our first run. The third run had spectacular seeing throughout most of the night (0.5-0.6'' in V), allowing diffraction limited images to be taken of WD 2140+207, WD 2246+223, and WD 2341+321. Throughout much of the second run, when most of my targets were taken, the full width half maximum (FWHM) of my final images ranged from ~ 140 milliarcseconds to ~ 200 milliarcseconds, compared to a diffraction limited FWHM of 120 milliarcseconds. WD 0501+527's final FWHM was 132 milliarcseconds, compared to the J band diffraction limited FWHM of 90 milliarcseconds.

4.3 Data Analysis

All data were flatfielded, background subtracted, registered, and combined into final images. These final images were used for two purposes: for deep background limited imaging far from the central target star and as PSF reference stars for other observations. Due to dithering, the highest sensitivity was generally within $7''$ of the target star.

Table 4.2. Observations

WD	Date(UTC)	Filters	Total Integration(s)
0208+396	11: 10: 46 2004-09-30	H	5280
0501+527	14: 22: 43 2003-10-11	J	3840
	15: 12: 45 2003-10-12	K	1920
0912+536	06: 33: 58 2004-04-02	H	3600
1055-072	08: 12: 16 2004-04-02	H	3600
1121+216	09: 24: 38 2004-04-02	H	3600
1213+528	10: 47: 20 2004-04-02	H	900
1334+039	11: 32: 37 2004-04-02	H	3600
1626+368	12: 46: 04 2004-04-02	H	3600
1633+433	14: 13: 36 2004-04-02	H	3600
1633+572	15: 22: 16 2004-04-02	H	960
1953-011	05: 09: 33 2004-09-30	H	3600
2140+207	06: 27: 51 2004-09-30	H	3600
2246+223	07: 44: 44 2004-09-30	H	3600
2341+321	09: 56: 37 2004-09-30	H	4680

In order to gain contrast close to each target white dwarf, I also employed PSF subtraction to get high contrast to within $1''$. To achieve good results, each registered subexposure was subtracted from another reference PSF image; preferably from a reference that was brighter than the target and that had a similar FWHM. The subtraction images were median combined to produce the final subtracted image. In the case of WD 1121+216 and WD 1953-011, there was a brighter star in the field and that was used as a simultaneous reference. Even though observations were separated by timescales on the order of hours, I was able to get subtraction that suppressed the PSF by 3-4 magnitudes at $0.8''$ (see Figure 4.1), with a higher sensitivity typically achieved in the non-subtracted images beyond $2''$. PSF subtraction was not possible for WD 1213+528, WD 0208+396, and WD0521+527, since no suitable reference was available. Figure 4.1 shows a comparison before and after PSF subtraction with a contemporaneous reference for WD 1953-011.

Any point sources that were detected had their flux measured by adding the counts within an aperture comparable to the FWHM of the particular image and comparing the counts in the same size aperture with the target star. A differential H magnitude was computed and then added to the 2MASS H magnitude of the WD, taking into account the transformation from the 2MASS system to the MKO system. Extended objects were interpreted to be background galaxies and had their total flux measured within a $0.5''$ radius aperture and compared to the flux of the target star in the field. Typically, most of the light from a star was captured within a $1.5''$ radius aperture, such that larger

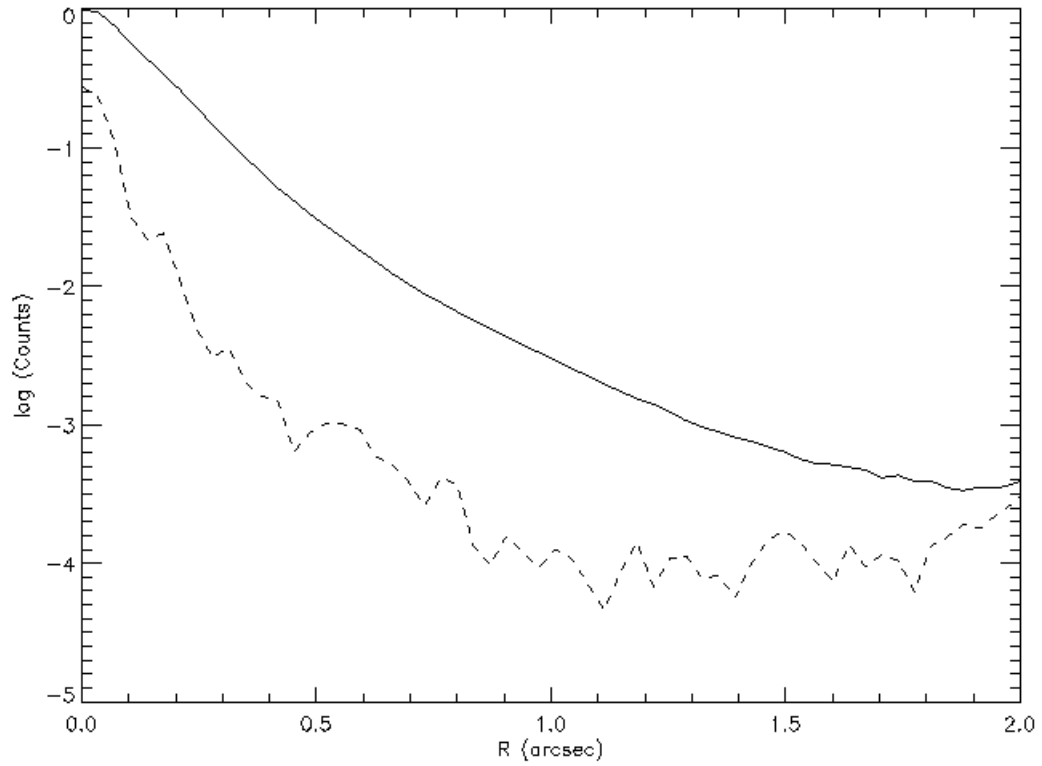


Fig. 4.1 Two azimuthally averaged PSFs for WD 1953-011, before subtraction (solid line) and after subtraction (dashed line). This WD had a contemporaneous PSF reference in the field which was used for subtraction purposes.

apertures changed the instrumental magnitude by ~ 0.01 mag or less. Since AO PSFs tend to vary with time photometric accuracy is limited by this variation and I found it preferable to use differential magnitudes since to zeroth order all PSFs in an image should be varying in the same manner. The large isoplanatic patch of PUEO makes this a reasonable assumption (Rigaut et al. 1998).

Table 4.3. Extragalactic Objects

Name	RA	Dec	H
DSW 1	02 11 20.67	+39 55 19.2	20.5
DGF 1	10 57 34.75	-07 31 22.8	19.8
DGF 2	10 57 34.63	-07 31 13.8	20.2
DGF 3	10 57 35.15	-07 31 11.5	20.5
DGF 4	11 24 12.82	+21 21 23.9	19.7
DGF 5	21 42 40.97	+20 59 49.5	19.0
DGF 6	21 42 41.71	+20 59 46.9	20.2
DGF 7	22 49 05.83	+22 36 37.3	19.0

4.4 Candidate Companions and Background Objects

Many targets showed nothing besides the primary in the field of view. However, six of the targets had other objects in the field which I designated as potential candidates. Any candidate would have to be unresolved. Where second epoch images were available, I used them to determine if any candidate was co-moving with the primary. If any second epoch images showed no common proper motion that candidate was eliminated. Two candidates do not have second epoch information and remain as viable brown dwarf candidates. Several of the higher latitude targets also had nearby resolved galaxies within $10''$, which I note in case they are useful for future groundbased study; such as with laser guided AO or multi-conjugate AO. Table 4.3 gives their positions and H band magnitudes within a $0.5''$ aperture. One object, DSW 1, has already been presented in Chapter 3, but here I add its MKO H magnitude from my CFHT observations.

4.4.1 WD 2341+321

WD 2341+321 has two candidate point sources—C1 and C2—that cannot be refuted with second epoch POSS images. Both are too faint to have been detected. C1 is at an R of $9.17'' \pm 0.01$ and a PA of $116^\circ \pm 1$, with an H magnitude of 18.5. C2 is detected closer in, after PSF subtraction. Figure 4.2 shows the original image and after PSF subtraction. This dimmer candidate is more promising since it is closer to the target WD, and is

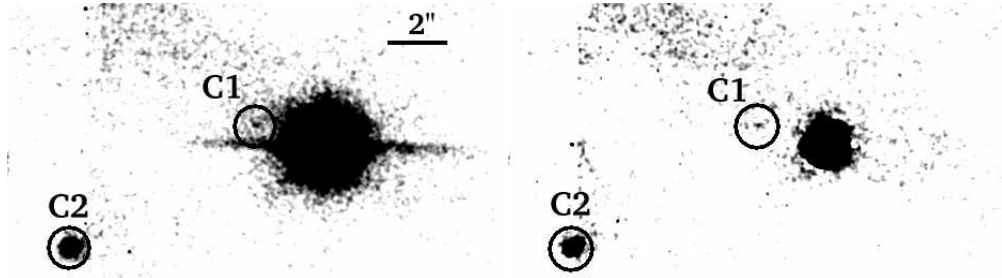


Fig. 4.2 Candidate companion (C1) at a separation of $2.25''$. If this object is physically associated it would be an $11M_{Jup}$ object.

detected at a S/N of 7 with an H magnitude of 22.3. It has an R of $2.25''$ and PA of $72.5^\circ \pm 1$. If both are physically associated with WD 2341+321, they would be $27 M_{Jup}$ and $11 M_{Jup}$ respectively. At a distance of 16.6 pc, they would have orbital separations of 37 AU and 152 AU corresponding to primordial separations of 13 AU and 54 AU, given a current WD mass of $0.57 M_\odot$ and an inferred initial mass of $1.6 M_\odot$. However, they cannot be ruled associated until they demonstrate common proper motion with WD 2341+321. WD 2341+321's proper motion is $0.21''/yr$, so it should be relatively easy to determine common proper motion within a year (Perryman et al. 1997).

4.4.2 WD 1121+216

WD 1121+216 has a brighter star $\sim 5''$ away. Inspection of POSS plates clearly shows that it is a relatively fixed background star and it is not a common proper motion companion.

After PSF subtraction, WD 1121+216 shows emission that at first glance appears to be a dust disk or blob ~ 20 AU from the WD. Figure 4.3 shows the emission. It is clearly visible both in the original image and after PSF subtraction. Inspection of the POSS 2 B plate shows that it is most likely a background galaxy, as there is an extended source at the position of the emission currently seen near the WD. Caution should be taken with high latitude objects that appear to show extended emission as a background galaxy can be mistaken for circumstellar emission. Any such discovery should show common proper motion to be credible. The background galaxy has a surface brightness of $20.1 \text{ mag}/\square''$. This detection demonstrates that I could have discovered any circumstellar emission for my targets at approximately this level.

4.4.3 WD 1213+528

WD 1213+528 shows a candidate companion $\sim 8''$ to the south, but inspection of POSS 2 plates shows that this object is not a common proper motion companion.

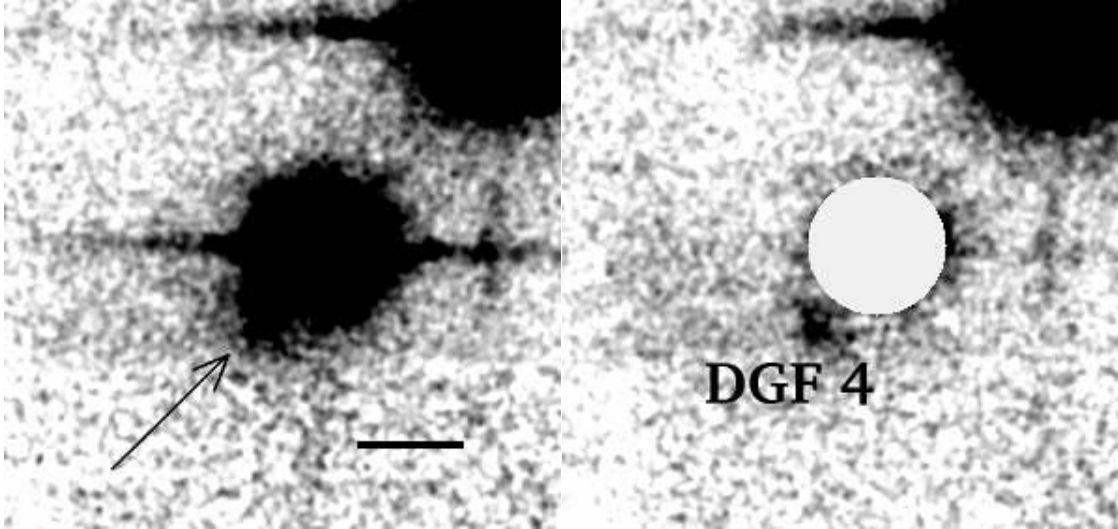


Fig. 4.3 These images show extended emission discovered around WD 1121+216 before (left panel) and after (right panel) PSF subtraction. Second epoch POSS images show that it is a background galaxy. The scale bar in the left panel represents $2''$.

4.4.4 WD 1953-011

WD 1953-011 has several nearby background sources, which are well separated. Most are visible on POSS plates and due to WD 1953-011's proper motion are easily discarded as possible proper motion companions. The brightest background object in the field, $\sim 7''$ to the South, has a noticeable companion at a separation $1.08'' \pm 0.01$, $\text{PA} = 88.6^\circ \pm 0.3$ with a $\Delta H = 7.6$. Figure 4.4 shows the star before and after PSF subtraction and Gaussian smoothing.

A spectrophotometric SED of the host star makes it consistent with either a $\sim M_0$ dwarf at ~ 300 pc or a K2 giant at ~ 10 kpc (Allen 1999). If it is a main sequence star, the companion would be a $0.07\text{-}0.08 M_\odot$ object according to the models of Baraffe et al. (2003). If it is instead a giant, the companion is an M dwarf. The M dwarf seems more plausible given the low galactic latitude of the source and the apparent lack of significant reddening. It is also possible the two stars are not physically associated. Despite the fact that this is not relevant to my current study, this discovery demonstrates the efficacy of my PSF subtraction technique.

4.4.5 WD 2140+207

WD 2140-207 has a dim, point-like object $\sim 5''$ away, with several point sources and galaxies in the surrounding field. Most of the point sources can be discriminated as background objects from POSS plates, including the near object discovered. With the help of POSS PSF subtraction, a marginal detection of the companion was possible on the POSS 2 B plate. At epoch 1990.57, the time of the observations taken by POSS,

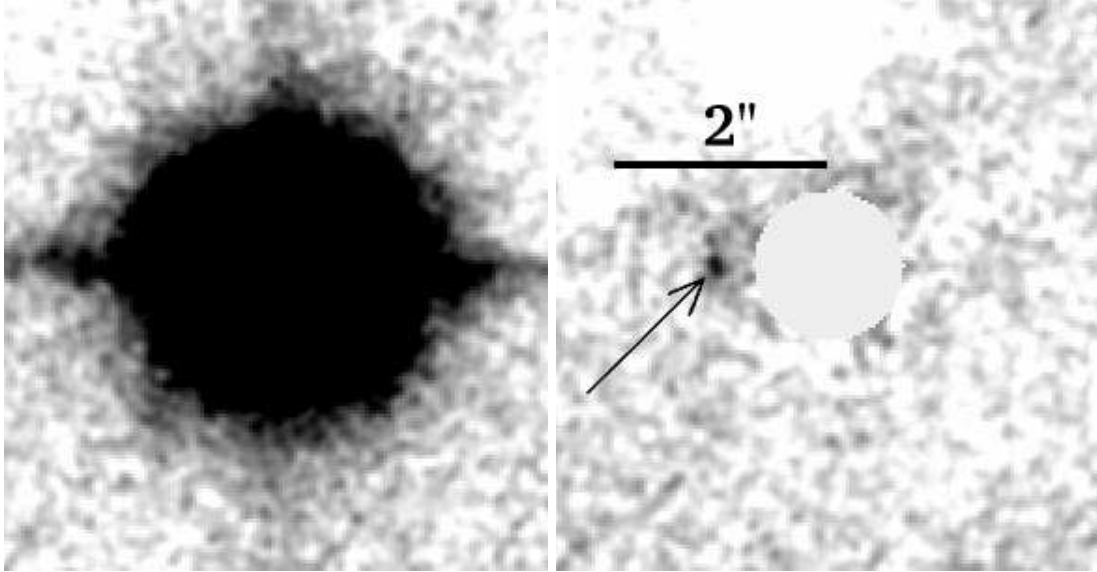


Fig. 4.4 Images of a nearby background star near WD 1953-011 that show a companion with $\Delta H=7.6$ with a separation of $1.08''$ before (left panel) and after (right panel) PSF subtraction. This detection demonstrates the study's sensitivity to point sources close to my targets.

the separation of the object had an R of $8.58''$ with a PA of 239.6° east of north. In my CFHT observations the object had an R of 5.88 and a PA of 296.7° . This is clearly a background object.

4.4.6 WD 0208+396

Two candidate objects as well as a galaxy $\sim 8''$ away were discovered in HST images presented in Chapter 3. The point source candidates were re-imaged on my third visit to CFHT ~ 1 year later and their H magnitudes measured. Figure 4.5 shows the images at the two epochs. C1 and C2 had H magnitudes of 19.35 and 22.22 respectively. In order to determine whether any of the candidates had common proper motion I needed to compare their positions relative to the HST observations in Chapter 3. In those observations the C1 was found to be at a separation of $8.60^\circ \pm 0.1$ and a PA of $175^\circ \pm 1$. Its F110W magnitude was 20.64 ± 0.01 . WD 0208+396 has a proper motion of 1069 mas/yr in RA and -523 mas/yr in Dec, which allows us to predict the position of the C1 if it is not co-moving. I predict C 1's position with respect to WD 0208+396 to be $\Delta RA = -0.41'' \pm 0.1$ and $\Delta Dec = -8.03'' \pm 0.1$. I find that the candidate is measured at a position $\Delta RA = 0.03''$ and $\Delta Dec = -8.02''$. C 2 has an F110W magnitude of 23.5 ± 0.1 and in the HST image had an $R = 10.33'' \pm 0.2$ with a $PA = 169^\circ \pm 2$. Its predicted position if not co-moving was predicted to be $\Delta RA = 0.82'' \pm 0.1$ and $\Delta Dec = -9.60''$. The measured relative position was $\Delta RA = 1.27''$ and $\Delta Dec = -9.51''$. There is a systematic, significant

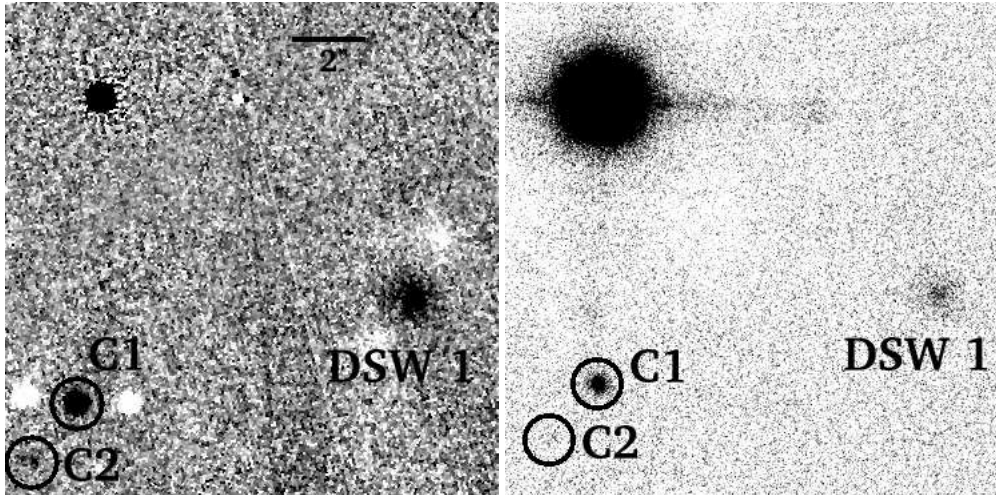


Fig. 4.5 A comparison between the HST and CFHT fields for WD 0208+395. The HST field is on the left and the CFHT field is on the right. The images are about $9''$ long on a side and shows one of the candidates due South of WD 0208+396 which is masked.

difference between the predicted ΔRA and that measured for both candidates which are also spatially close. Measurements of the relative position of the galaxy in the field also shows a similar discrepancy in where its relative position should be (it's obviously not co-moving) which supports the explanation that the CFHT field is rotated clockwise by $\sim 1.7^\circ$, which places all of the measured positions within the errors of the predicted positions. Therefore, I can state with certainty that the candidates are both background objects.

4.5 Limits to Companions

Since many targets did not have any possible companions, it is instructive to place limits on what kind of objects could be detected around each target. I can place limits both for resolved and unresolved companions by the combination of my imaging results and the measurement of these objects' measured flux in comparison with their expected flux.

4.5.1 Imaging

I followed the same strategy for determining my imaging sensitivity as in Section 3.5.2. The main difference for AO imaging is that the PSF is not stable, so I use a version of my target WD PSF normalized to 1 DN. The implant would be scaled by a value, placed within the field and an aperture approximately equal to the implant's core FWHM was used to determine the S/N. If the S/N was >5 , then the implant was considered recovered. Values at 20 different angular locations were determined at each

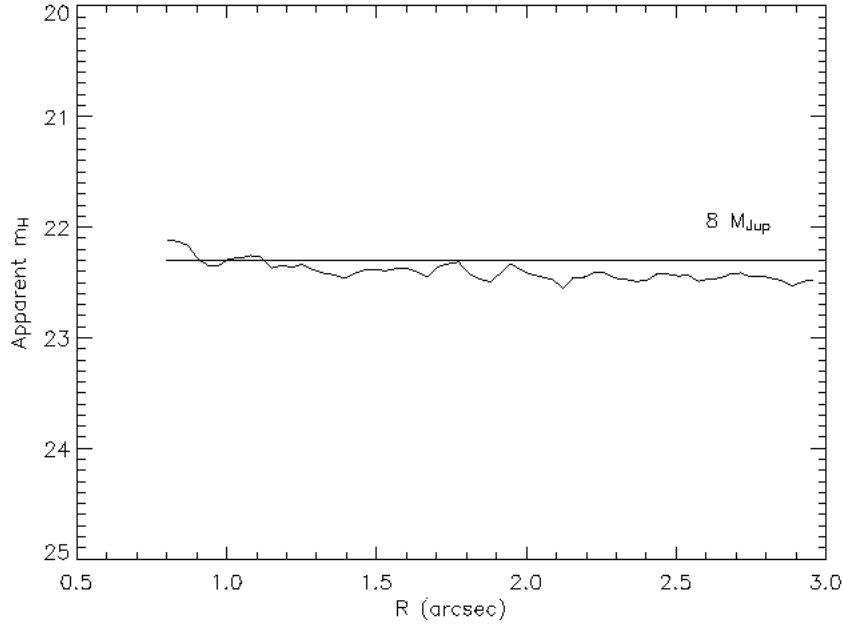


Fig. 4.6 Sample 5σ sensitivity curve of WD 2246+223. Overplotted is the H magnitude of an $8 M_{Jup}$ companion at the age and distance of the target.

radius, for azimuthal averaging. The median of the different values was taken to give a final azimuthal averaged sensitivity. Relative photometry with respect to the target WD (or another unsaturated object in the field) was calculated and the 2MASS H magnitude for the target WD was used to determine a final sensitivity. Figure 4.6 shows a typical sensitivity curve with PSF subtraction.

The values were then used with a grid of substellar spectral models to determine what kind of substellar object a limiting magnitude would correspond to at the particular distance and age of the WD system. Specifically, I used the models of Baraffe et al. (2003), primarily because they had isochrones that spanned the mass range and age of interest to my target WDs. The magnitudes were cross checked with the models of Burrows et al. (2003) and for isochrones that overlapped they provided similar results to within a magnitude or to within 1 or $2 M_{Jup}$, thus giving me confidence that I could mesh my results here with those in Chapter 3. Using interpolation, I turned the observed sensitivities to specific masses at the particular ages of the WDs. Table 4.4 shows the final sensitivities for each WD.

4.5.2 Near-IR Photometry

While direct imaging is most sensitive to companions $>1''$ unresolved companions could still be present for some of these targets. In order to rule out companions at separations where imaging or PSF subtraction could not resolve them, I turn to the near-infrared fluxes of these objects provided by 2MASS photometry (Cutri et al. 2003). Using the measured effective temperatures, gravities, and distances of the WDs given in the literature, I can model the expected J, H, and K_s fluxes based on the models of Bergeron et al. (1995). If the photometry is of a high enough accuracy, one can place limits on the type of excesses present for these objects. These limits allow me to understand what types of companions and dusty disks are ruled out. The details of this process have already been described in Section 3.5.1. For my targets here, the majority come from Bergeron et al. (2001), but the WD 2341+321 parameters came from Liebert et al. (2004). Section 3.5.1 calculated the estimated 1σ limits for both samples in the J, H, and K_s filters to be 0.04, 0.04, and 0.05 mag respectively for the Bergeron et al. (2001) sample. For the sample of Liebert et al. (2004) I find that the limits are 0.07, 0.10, and 0.15 for J, H, and K_s respectively.

The one exception is WD 0501+527, whose parameters are taken from Finley et al. (1997). The distance to WD 0501+527 is determined from its Hipparcos parallax (Perryman et al. 1997). In the Finley et al. (1997) sample, only spectroscopic properties were determined, so no attempt to model the distance was made. Due to a lack of modeled distance, I cannot estimate the rough error in the modeling as an ensemble. Rather, I compare ΔJ to the quoted photometric errors in 2MASS. The errors in J are ~ 0.02 , and since ΔJ falls within this range, I use this as my estimate for a significant excess, which I determine to be an excess of 0.06 in J. Since WD 0501+527 is so hot, its cooling time is $\ll 1$ Gyr and its total age depends entirely on its initial mass. Unfortunately this is unknown, so I calculate possible companion limits given a range of possible main sequence ages for this WD.

All of my other objects show no significant excess as well so I need to determine to what mass limit I could have detected an excess in my sample. Taking the substellar models of Baraffe et al. (2003), I took the 3σ limits and interpolated between the models to fit the estimated total ages of the white dwarf targets. I find that for all of my targets, any object more massive than $\sim 69 M_{Jup}$ would have been detectable in the 2MASS search. Therefore, all targets should not have any stellar companions present at close separations. The exceptions to the limit are WD 1213+568, which already has an unresolved companion M dwarf, and WD 0501+527, which is less sensitive due to its large T_{eff} . Any further excess beyond the companion of WD 1213+568 cannot be determined. Table 4.4 shows my results for unresolved and resolved companion sensitivities. For the excess limits we take into account the distance to the WD to obtain a limit on the absolute magnitude of an object that could create an excess.

Table 4.4. Sensitivities

WD	Excess Limit (M_J)	Mass (M_{Jup})	Sensitivity $>1''$ (H)	Mass (M_{Jup})
0501+527 (1 Gyr)	15.6	75	19.8	25
(5 Gyr)		80		54
(10 Gyr)		80		63
0912+536	15.6	40	21.3	12
1055-072	16.1	39	20.9	14
1121+216	15.9	37	21.3	11
1213+528	-	-	18.0	29
1334+039	15.4	61	21.9	18
1626+368	16.0	43	21.1	14
1633+433	16.3	40	20.9	14
1633+572	16.4	45	20.5	19
1953-011	15.4	37	20.8	10
2140+207	15.3	40	21.5	10
2246+223	16.7	33	22.3	9
2341+321	14.8	63	22.4	15

Chapter 5

Future Directions for High Contrast Imaging

The work in this chapter has been published in:

Debes, J. H., Ge, J., Kuchner, M., & Rogosky, M. 2004, *ApJ*, 608, 1095

Debes, J. H. & Ge, J. 2004, *PASP*, 116, 674.

5.1 Gaussian Aperture Pupil Masks

5.1.1 Introduction

The search to directly image an extrasolar planet around a nearby solar type star requires contrast levels of $\sim 10^{-10}$ a few λ/D from the central star, where λ is the wavelength of light observed and D is the diameter of the observing telescope's primary mirror. Scattered light in a telescope and the diffraction pattern of the telescope's aperture limit the contrast possible for direct detection of faint companions (Brown & Burrows 1990). The circular aperture of telescopes creates a sub-optimal diffraction pattern, the so-called Airy Pattern which is azimuthally symmetric. In addition, the intensity in the diffraction pattern of the circular aperture declines as $(\theta/\theta_o)^{-3}$, where $\theta_o = \lambda/D$. Currently the best way to diminish the Airy pattern is to use a coronagraph by using the combination of a stop in the focal plane that rejects a majority of the central bright object's light and a Lyot stop in the pupil plane to reject residual light diffracted to the edge (Lyot 1939; Malbet 1996; Sivaramakrishnan et al. 2001). Several recent ideas explore the use of alternative "apodized" apertures for high contrast imaging in the optical or near-infrared (Nisenson & Papaliolios 2001; Spergel 2001; Ge 2002; Kuchner & Spergel 2003a). These designs revisit concepts first experimented with in the field of optics (Jacquinot & Roizen-Dossier 1964). Other designs, such as the band limited mask or notch-filter mask, seek to null the light from a central star by varying the amplitude of the central star's light in the focal plane (Kuchner & Traub 2002; Kuchner & Spergel 2003b; Debes et al. 2004).

All of these designs in theory can reach the contrast ratio necessary for imaging a planetary companion. Most of these concepts, however, are just starting to be tested in the lab or on a real telescope where other concerns arise. Each design also has its own set of drawbacks. Pupils or image plane masks that require transmissive functions require precision to very high levels (10^{-10}) and are susceptible to degradation in a space environment (Kuchner & Spergel 2003a). Designs that use binary masks have less restrictive tolerances but must be fabricated precisely. The specific advantages of each idea cannot be determined until they are actually built and tested in such a way as to simulate real observing conditions.

Apodization through binary shaped apertures that have either completely transmissive or completely opaque openings represents one promising class of techniques. An intuitive description of how the choice of a shaped aperture affects the resulting PSF is in order. The entrance aperture can be described as a contour $y' = \pm(1/2)C(x')$, where $|x'| < x'_M$ is the maximum horizontal extent of the aperture. An example of a familiar contour for an entrance aperture is $C(x') = \sqrt{x'_M - 4x'^2}$, the equation for a circular aperture. The resulting point spread function (PSF) as predicted by scalar Fraunhofer diffraction theory is given by the 2-D Fourier transform of the aperture:

$$\mathcal{A}(\xi', \eta') = \int_{-x'_M}^{x'_M} \int_{-\frac{1}{2}C(x')}^{\frac{1}{2}C(x')} \exp(2\pi k i \xi' x') \exp(2\pi k i \eta' y') dx' dy' \quad (5.1)$$

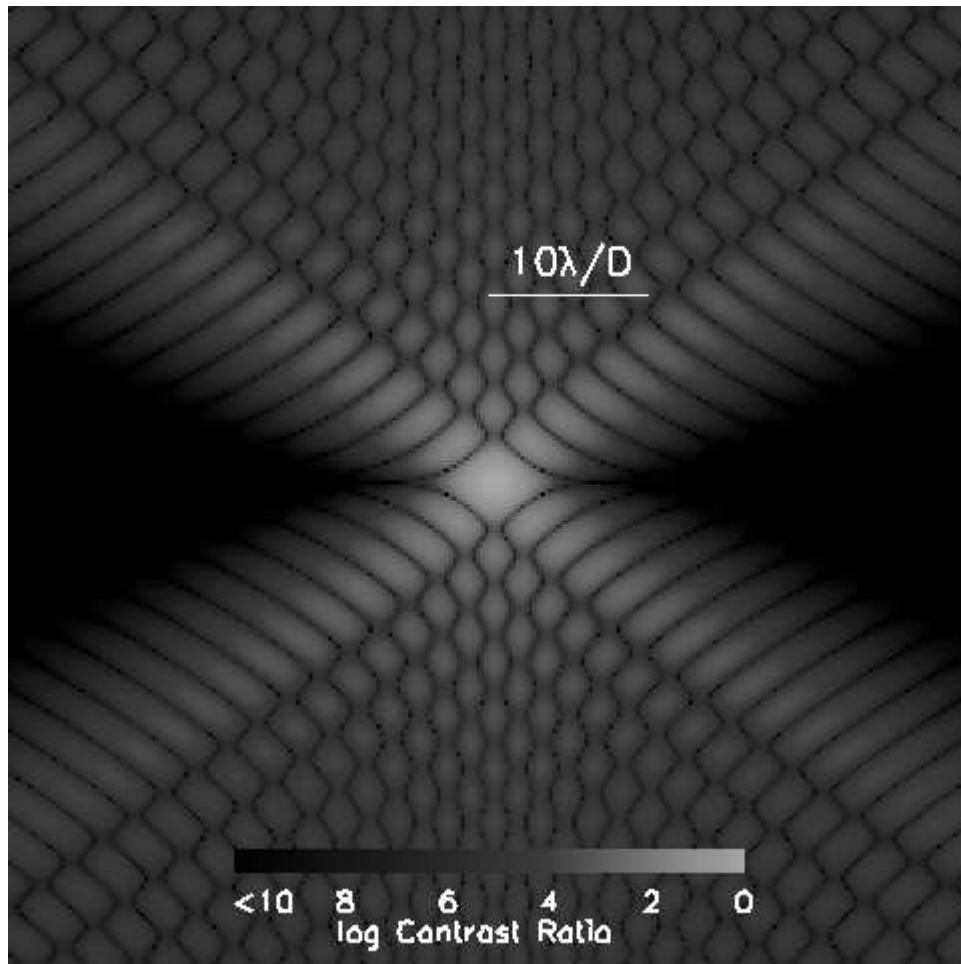


Fig. 5.1 The resulting monochromatic diffraction pattern for a single aperture GAPM with $a = 1$, and $\alpha = 2.5$. The image is logarithmically scaled.

where $k = 2x'_M/\lambda$ and I follow the notation of Jacquinet & Roizen-Dossier (1964). I then transform this equation into the reduced coordinates $x = x'/2x'_M$, $y = y'/2x'_M$, $\xi = 2\xi'x'_M/\lambda$, and $\eta = 2\eta'x'_M/\lambda$. The equation then becomes:

$$\mathcal{A}(\xi, \eta) = \int_{-\frac{1}{2}}^{\frac{1}{2}} \int_{-\frac{1}{2}C(x)}^{\frac{1}{2}C(x)} \exp(2\pi i \xi x) \exp(2\pi i \eta y) dx dy. \quad (5.2)$$

This two dimensional problem can be simplified to a one dimensional Fourier transform provided the PSF is restricted to a particular $\eta = \eta_o$:

$$\mathcal{A}(\xi, \eta_o) = \int_{-\frac{1}{2}}^{\frac{1}{2}} \frac{\sin(\pi \eta_o C(x))}{\pi \eta_o} \exp(2\pi i \xi x) dx \quad (5.3)$$

By sampling η to the desired precision, one can build up a 2-D PSF by performing a 1-D Fast Fourier Transform (FFT) (Lieber 2003). In this way the PSF can be determined with more accuracy and less time than with traditional 2-D FFTs. There exists the special case of the diffraction pattern along the $\eta = 0$ axis, which even more greatly simplifies the expression by becoming a simple Fourier Transform of $C(x)$:

$$\mathcal{A}(\xi, 0) = \int_{-\frac{1}{2}}^{\frac{1}{2}} C(x) \exp(2\pi i \xi x) dx \quad (5.4)$$

Binary shaped apertures where $C(x)$ is described as a truncated Gaussian function represent a promising design for high contrast imaging and was suggested for extrasolar planet searches by Spergel (2001). However, the idea has potential uses on ground based telescopes as well for more modest goals, such as high contrast imaging surveys that cannot afford to take the overhead of aligning coronagraphic masks or that observe multiple targets in one field of view (Ge 2002). In this case the gaussian contour is

$$C(x) = a \left\{ \exp \left[-(2\alpha x)^2 \right] - \exp \left(-\alpha^2 \right) \right\}. \quad (5.5)$$

Since the Fourier transform of a gaussian function is another gaussian, the amplitude of the diffraction pattern $A(\xi, \eta)$ along the ξ axis decreases like $e^{-\xi^2}$, which I denote the high contrast axis. The intensity distribution in the imaging plane is given by $|AA^*|$. The ratio $z = I(\xi, \eta)/I(0, 0)$ gives the contrast relative to the peak intensity of the diffraction pattern. The variables a and α are free parameters that can be used to optimize the aperture for depth of contrast, the angle from the central object at which high contrast starts, and the azimuthal area of high contrast. It should be noted that based on this definition, changing α subtly changes the height of the contour since the maximum height of the contour is $\propto 1 - \exp(-\alpha^2)$. However, in terms of the range of α that we test and are interested in for realistic observations ($\alpha = 2 - 4$), this is a negligible effect on the order of a few percent.

The final peak intensity $I(0, 0)$ measured on a detector is proportional to the total area of the aperture squared. In the reduced coordinates that I use, a square, fully transmissive aperture gives the maximum intensity, which I normalize to one (Jacquinet &

Roizen-Dossier 1964). In this normalization, a circular aperture gives rise to a maximum intensity of $\pi^2/16$. Determining the peak intensity for a Gaussian aperture pupil mask (GAPM) then requires summing the total area of the given aperture and squaring it:

$$I(0,0) = \left| \int_{-\frac{1}{2}}^{\frac{1}{2}} C(x) dx \right|^2. \quad (5.6)$$

Solving this for Equation 5.5, gives $I(0,0) = (a\sqrt{\pi}\text{erf}(1/2)/(2\alpha) - a\exp(-\alpha^2))^2$. I can compare this to a circular aperture. For an $\alpha = 2.7, a = 1$ GAPM, this corresponds to a peak intensity 3% of a full circular aperture. A Lyot stop that undersizes the circular aperture by 1/2 gives a peak 6.25% of the original. Light gathering power is proportional to the area, and so for the same examples, the Lyot coronagraph would have 25% throughput and the GAPM would have 17%.

By substituting Equation 5.5 into Equation 5.3, the PSF can be determined. Figure 5.1 shows the resulting PSF for an aperture with $a = 0.6$ and $\alpha = 2.9$, a typical pattern from a Gaussian contour. Since the contour is not azimuthally symmetric, neither is the PSF. The PSF has a region of high contrast, which I denote the high contrast region (HCR). High contrast is deepest along the ξ axis.

If one is designing a mask, it would be useful to have several first order estimates of the dependance of a and α on the resulting diffraction pattern. I start with the contrast along the axis of highest contrast and an approximate separation in ξ where high contrast starts. The exact solution of Equation 5.4 is given by

$$\mathcal{A}(\xi, 0) = \frac{\sqrt{\pi}}{2\alpha} \exp\left[(\pi\xi/2\alpha)^2\right] \star \text{sinc}(\xi) - 2 \exp\left(-\alpha^2\right) \text{sinc}(\xi), \quad (5.7)$$

where $\text{sinc}(\xi) = \sin(\pi\xi)/\pi\xi$. This is difficult to manipulate analytically, but can be approximated to first order by

$$A(\xi, 0) = \frac{\sqrt{\pi}}{2\alpha} \exp\left[-(\pi\xi/2\alpha)^2\right] - \exp\left(-\alpha^2\right) \text{sinc}(\xi), \quad (5.8)$$

which ignores the truncation of the exponential part of the function.

The width of the PSF core can then be estimated by determining the location of the first zero (ξ_{fz}) in Equation 5.8. After some manipulation one finds that

$$\xi_{fz}^2 = \frac{4\alpha^2}{\pi^2} \left[\alpha^2 - \ln|\text{sinc}(\xi_{fz})| + \ln\left|\frac{\sqrt{\pi}}{2\alpha}\right| \right]. \quad (5.9)$$

One can solve this equation exactly through a simple recursion algorithm. However, noting that $\ln|\text{sinc}(\xi)| \sim 3$ over the range of ξ we are interested in ($\xi = 3 - 10$), that $\ln\left|\frac{\sqrt{\pi}}{2\alpha}\right| \sim -1$ over the range of interesting α values ($\alpha = 2 - 4$), and assuming $\alpha^2 \gg 2$, I find that Equation 5.9 is well approximated by:

$$\xi_{fz} = \frac{2\alpha^2}{\pi} \left(1 + \frac{1}{\alpha^2} \right). \quad (5.10)$$

The approximate contrast one can expect to achieve is then found by substituting ξ_{fz} into Equation 5.8 and squaring the result. Finally, one can estimate the angular coverage of the HCR by noticing the HCR is governed by the tail of the Gaussian function, which transitions over at the contour's change of curvature. By solving for the maximum angle where the change occurs on the aperture, the resulting angle of high contrast in the imaging plane is given by

$$\cot \theta = \sqrt{\frac{2}{e}} a \alpha. \quad (5.11)$$

By placing a mask into the pupil plane with a Gaussian aperture, one can transform a traditional circular aperture telescope into one with a diffraction pattern better suited for high contrast imaging. Using a mask represents a quick, efficient, and economical way to test this emerging imaging method to determine its advantages and trade-offs and compare them to the performance of other existing techniques. More subtle phenomena that limit contrast can also be studied and removed with a well-known system whose ideal performance and performance under non-ideal conditions can be easily modeled. Scattered light from microroughness or polarization effects can be more reliably studied and verified experimentally rather than with theoretical treatments.

I have endeavored to begin answering the question of which design ultimately will be useful in the search for extrasolar planets, or which will be most useful for other areas of astronomy where less stringent tolerances are present. To that end I have designed, fabricated, and tested several GAPM designs for use with the Penn State near-IR Imager and Spectrograph (PIRIS)(Ge 2003). In Section 5.1.2 I explore what the best design for a telescope would be. In Section 5.1.3 I briefly discuss the process of fabrication of the GAPMs, while in 5.1.4 I discuss the various tests I performed in the lab and on the ground at the Mt. Wilson 100'' telescope.

5.1.2 Designing a GAPM for current telescopes

The idealized design of a single Gaussian aperture in practice cannot be used on current telescopes due to their circular secondary obstructions and the presence of the support structure. These two additions serve to modify the resulting diffraction pattern and destroy the advantages of the single aperture. Therefore, a new design that avoids or minimizes their effect is necessary to retain high contrast. There are two possible solutions: multiple apertures that avoid the structure completely, or blocking support structure without changing the diffraction pattern in the imaging plane.

5.1.2.1 Multiple Apertures

By taking a contour over a sub-aperture of width hD where D is the diameter of the telescope pupil, one reproduces a similar diffraction pattern as obtained from the contour described in Equation 5.5. One important exception is that ξ and η must be rescaled by dividing by h . One can model the resulting PSF from placing multiple subapertures on the pupil by a convolution of the base subaperture with a sum of N δ -functions in the desired positions of the subapertures. The Fourier transform of that

convolution becomes:

$$\mathcal{A}'(\xi, \eta) = \mathcal{A}(\xi, \eta) \sum_{k=1}^N \exp(2\pi i x_k \xi) \exp(2\pi i y_k \eta). \quad (5.12)$$

As mentioned in Spergel (2001) and Kasdin et al. (2003), one can also have multiple apertures with asymmetric sides as long as they are reflected about the y -axis. In this case the contour can be described on the full pupil in the original reduced coordinates of Equation 5.1 as

$$\begin{aligned} C_1\left(\frac{x}{h}\right) &= hC\left(\frac{x}{h}\right) + 2y_o \\ C_2\left(\frac{x}{h}\right) &= -\frac{hb}{a}C\left(\frac{x}{h}\right) + 2y_o \end{aligned} \quad (5.13)$$

where y_o is a constant vertical offset from the y -axis and a is not equal to b . The resulting diffraction pattern is the superposition of the PSF from the two contours. Either approach can yield a grouping of apertures that completely avoids the support structures and maximizes the possible throughput. The potential tradeoff is a widening of the PSF core, as well as a new peak that is multiplied by a factor of Nh^4 .

5.1.2.2 Minimizing Support Structure

Another option for avoiding the secondary of a telescope is to create an opaque secondary Gaussian curve that blocks the circular secondary mirror. The result in the focal plane would be the superposition of PSFs, which follows naturally from the Babinet principle. One way of implementing this design is to have a contour similar to Equation 5.5 but with a second contour with a height b where $b < a$:

$$\begin{aligned} C_1(x) &= aC(x) \\ C_2(x) &= -bC(x). \end{aligned} \quad (5.14)$$

The resulting PSF retains the higher resolution of the telescope, though angular coverage may be less than what could be achieved with multiple apertures.

In this case it is important to estimate the effect of not avoiding the support structure. The level of contamination by the support vanes for the secondary mirror can be estimated by deriving the diffraction pattern for a slit with the same proportions of the vanes and using Babinet's principle. A vane of width w along the x -axis and length l in the y -axis produces an amplitude of

$$\mathcal{A}_s(\xi, \eta) = wlsinc(\xi w)sinc(\eta l). \quad (5.15)$$

The vane will be brightest along the ξ axis. Ideally, support vanes should be rotated 45° with respect to the HCR, so that the diffraction spikes can be masked by the lower contrast regions of the PSF. \mathcal{A}_s can be compared to $\mathcal{A}(0)$. If $\mathcal{A}_s \ll \mathcal{A}(0)$ and the secondary is not so large that the loss in throughput is great, this method may be preferable. As an example, I look at spider vanes that have a width of $\sim 10^{-3}D$, which

corresponds to a contrast of 10^{-8} at a distance of $5\lambda/D$ assuming that the two vanes are oriented 45° to the axis of interest. Clearly this places a fundamental limit on the width of any support structure (or gaps in a multi-mirror design) for an extrasolar planet search. Taking the limiting contrast to be 10^{-10} at $5\lambda/D$, the size limit is $10^{-4}D$.

Table 5.1. Table of Design Parameters

GAPM Design	α	a	b	x_k	y_k	h
Mt. Wilson	2.7	0.23	0.33	$(\pm 0.3125, \pm 0.1625, \pm 0.1625)$	$(0.1, 0.2125, 0.3875)$	0.5
Lab	2.7	1.	-	0	0	0.8

5.1.2.3 Final Design of the Prototype

I designed a mask to be used at the Mt. Wilson 100'' telescope for preliminary observations, as well as a single aperture design for testing in the lab. The diameter of the secondary at Mt. Wilson is $\sim 30\%$ the diameter of the primary and the width of the spider vanes are $\sim 0.25\%$ of the diameter. I decided to completely avoid the support structure for the initial prototype to lower the risk of the PSF being contaminated by misalignments of the pupil mask. For a final design I decided to try a variation of what was proposed by Spergel (2001), using a contour based on Equation 5.13 by placing 3 sub-apertures in each quadrant of the mask to maximize throughput to about 16%. Table 5.1 shows the parameters that I used for the two masks as well as the positioning of the apertures for the Mt. Wilson design. Figure 5.2 shows what the final design looked like. Figure 5.3 shows a comparison between a J band image taken with the mask and a theoretical PSF modeled by taking digital images of the apertures at high magnification and taking a 2D FFT with IDL. Since the spatial scale of the PSF determined in Equation 5.2 is scalable with wavelength, one can build a multi-wavelength PSF by adding the scaled PSF in wavelength bins together and multiplying by the transmission of the particular filter used.

5.1.3 Fabricating a GAPM

Once a design was chosen, the masks were fabricated. I chose to fabricate the Mt. Wilson and lab designs with Photo-Chemical Machining (PCM). This technique has been used to produce masks to block thermal radiation from telescope structures for near-IR observing and for creating Lyot stops (McCarthy 2001).

The process of PCM, also called Photo-Etching or Photo-Chemical Milling, involves using a thin metal sheet that is coated with a light sensitive polymer. A UV photo imaging tool is used to imprint the desired design on the sheet. It is then developed much like film and chemically etched by an aqueous solution of ferric chloride (FeCl_3).

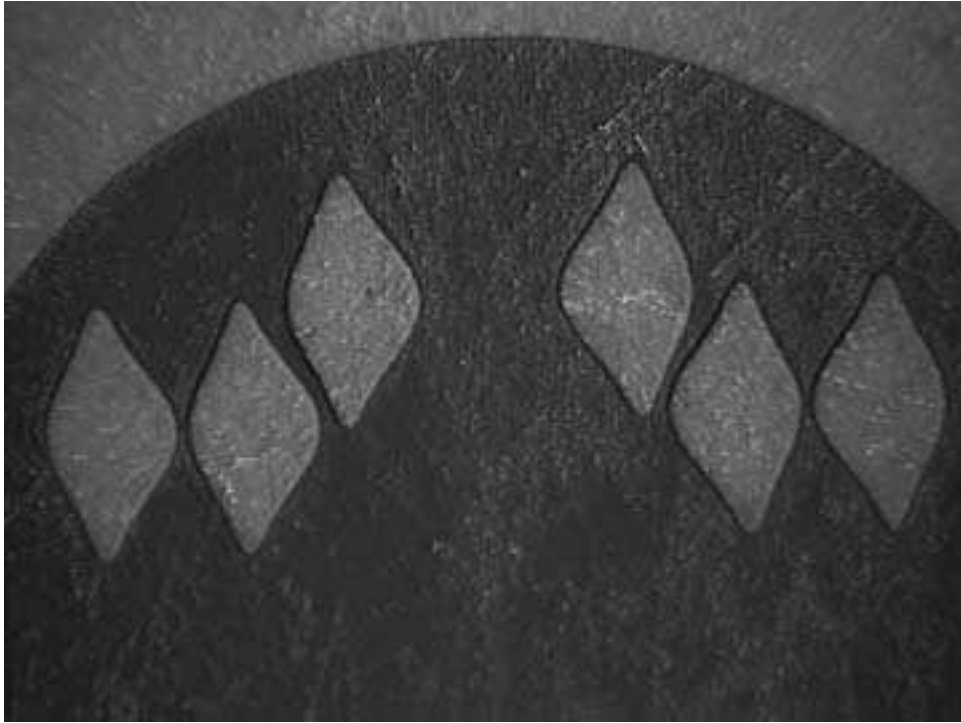


Fig. 5.2 The top half of the fabricated mask used for observing on the Mt. Wilson telescope at 5x optical magnification. The twelve apertures allow $\sim 25\%$ throughput, while avoiding the support structure of the telescope. This picture shows the imperfections in the fabrication process.

Several masks are present in the PIRIS camera mainly for the traditional Lyot coronagraphic modes. They were fabricated by Newcut, Inc. (Newark, NJ). For the GAPMs I submitted CAD designs based on the parameters listed in Table 5.1 to Newcut and they fabricated the masks. A sheet of 25-50 \sim 4 mm diameter masks was fabricated at very low cost within a few weeks. When they were delivered they were photographed on an optical telescope with 5x and 50x magnification.

This technique can provide the basic shape I need, but it has difficulty preserving the exact shape of the design in the smallest regions. The edges of the Gaussians on the mask were truncated well before they would be mathematically. Variations on the order of 10 μ m are also observed in the masks. Both of these imperfections can degrade contrast, which is discussed further in Section 5.1.4. These imperfections are likely caused by the photo printing as well as the chemical etching. For instance, the corner truncation and width variation can be caused by underexposure of the light sensitive polymer. The rugged edge can be caused by non-uniform chemical etching. Since the etching is isotropic, changes in the physical and chemical conditions of the etchant can cause local irregularities.

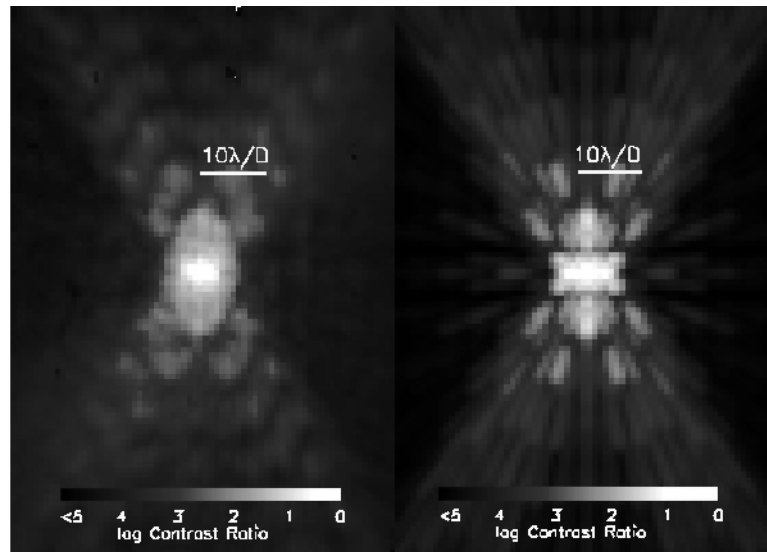


Fig. 5.3 Comparison of the theoretical J band diffraction pattern (right) compared with lab results with PIRIS (left). Both are on the same logarithmic scale. The model used included the imperfect shape of the mask that was fabricated and the model was integrated over the transmission function of a typical J filter.

5.1.4 Testing the Prototype

5.1.4.1 First Light and Lab tests

I placed the Mt. Wilson design on the Penn State Near-IR Imager and Spectrograph (PIRIS) and ran tests both in the lab and on the 100'' Mt. Wilson telescope. I used the prototype as part of a survey for faint companions around nearby solar type stars (Chakraborty et al. 2002).

I used the prototype GAPM to study two stars, ϵ Eridani and μ Her A. The mask allowed confirmation of a common proper motion companion to μ Her A and placed limits on any possible companions around ϵ Eridani, down to the level of a $38M_{jup}$ brown dwarf. This corresponds to a performance an order of magnitude better than adaptive optics alone and 2 times worse than my Lyot coronagraph performance without blocking the central star's light (Debes & Sigurdsson 2002).

Lab testing was also performed in the J and H bands on the Mt. Wilson design. The setup involved taking an incandescent lamp and simulating a point source to sample the PSF generated by the different masks. An optical fiber took light from an incandescent lamp where it passed through a micro objective and a pinhole. The light then was collimated by a collimator achromat. After the collimator the light was focused onto the slit wheel aperture by an image achromat. The image achromat also forms an exit pupil, ~ 1.9 m away from the focal plane, mimicking the Mt. Wilson 100'' exit pupil. On the slit wheel I placed my focal plane coronagraphic masks. The light then travels through the camera optics of PIRIS where it is read by the 256×256 PICNIC array.

Figure 5.4 shows an azimuthally averaged comparison between the data taken at Mt. Wilson, lab tests in the J band, and two theoretical multiwavelength PSFs as a function of λ_o/D , where λ_o represents the central wavelength of the filter used. For the lab and models this corresponds to using a J filter, whereas on Mt. Wilson all observations were done in the K band. Azimuthal averaging was performed over $\pm 30^\circ$ from the high contrast axis on both sides. One simulation, called model 1, represents a completely ideal situation where the mask is perfectly created and no wavefront errors exist. The second simulation, model 2, takes the observed shape of the masks under magnification as the apertures and neglects other errors. One can see that the theoretical simulation of the observed shape matches the lab data quite well, off by less than an order of magnitude close to the center. The observed shape errors also degrade the contrast achievable by the idealized design. Finally, the effect of the atmosphere is present in the Mt. Wilson data. From my observations, the seeing was $\sim 1''$, giving a Fried parameter $r_o \sim 46$ cm at $2.2 \mu\text{m}$. I estimate that my Strehl ratio for most of the observations was lower than expected, ~ 0.1 . At this level of correction, the halo from the atmosphere severely degrades the contrast to $\sim 10^{-2}$.

From images of the pupil optics of PIRIS, I observed low amounts of light leakage and thermal emission. This leakage slightly degrades contrast, which would explain the slight difference between my models and the observed lab PSF.

The single aperture GAPM was also tested in the J band in the lab. Figure 5.5 shows the contrast achieved with an azimuthal average over $\pm 20^\circ$ with respect to the high contrast axis. The truncation present in the fabrication also severely degrades the contrast possible with this mask. I find that I can achieve a contrast of $\sim 10^{-5}$ at $10\lambda/D$.

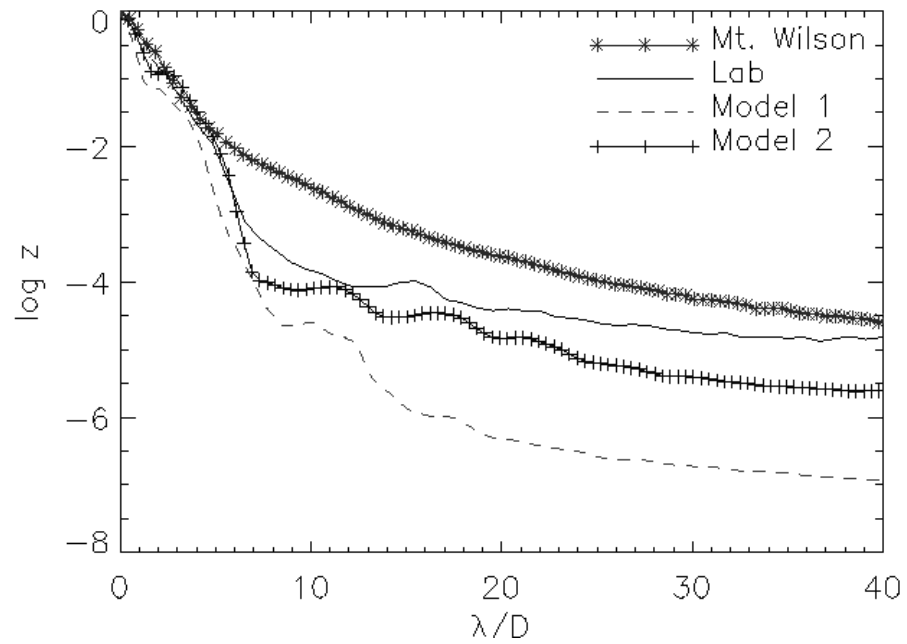


Fig. 5.4 Azimuthally averaged PSF profiles for the GAPM multiaperture design tested at Mt. Wilson, along with results of a lab test in the J band and two different models. Model 1 represents a model with perfect apertures, while Model 2 is the simulated results based on the actual shape of the apertures.

5.1.4.2 Modeling the Degradation in Contrast

Figure 5.2 shows one of the greatest limitations to the current prototype, which is the truncation of the thinnest parts of the mask. This is due to errors in the fabrication process as well as a lack of resolution to reproduce the true contour. I can model this effect by taking images of the apertures and digitizing them into model apertures, which has been shown to be effective in Figures 5.3 and 5.4.

There is also a way to express this analytically, by slightly changing the contour of the aperture:

$$C(x) = a \left\{ \exp \left[- (2\alpha x)^2 \right] - \exp(2\beta x) \exp \left(-\alpha^2 \right) \right\}, \quad (5.16)$$

where β is a free parameter that can be determined empirically. The effect of this change raises the floor of contrast by increasing the strength of the second term in Equation 5.16.

Figure 5.6 shows a comparison between the observed multi-wavelength PSF of my prototype Mt. Wilson design and a model based on Equation 5.16 both azimuthally averaged over 20° around the high contrast axis. A value of $\beta=13$ matches the observed PSF and the models based on the fabricated apertures quite well.

Another potential problem beside truncation of the edges is the tolerance for accuracy in the mask itself. I can estimate the effect by considering either a square opening or obstruction of side h depending on the kind of error that occurred. This extra square will create its own diffraction pattern that will constructively add to the PSF. Using the same equation as in Equation 5.15, we can estimate the intensity due to the total number of errors present for a particular distance, $\sim (N_{err} h^2 / \pi \xi)^2$, where N_{err} is the total number of errors present. In the case of errors due to the resolution of a fabrication method, one can base the estimate on the fact that the number of errors will be $\sim h^{-1}$ where I assume the size of the error is no bigger than the resolution of the machine. This leads to the contrast degrading as h^2 . In order to reach a contrast of 10^{-10} at $4\lambda/D$, errors are restricted to $< 10^{-4} D_p$, where D_p is the pupil mask diameter. For a pupil mask with a diameter of 4 mm, this corresponds to a resolution of $.4 \mu\text{m}$.

5.1.4.3 Lessons for AO observers

The lessons that can be gained from the AO observations can be put to use for future work. It is clear that a high order of correction is needed for the full advantage of the GAPM to be utilized. Ideally one would choose an inner working distance (IWD) that is less than the region that is fully corrected (to the level of the residual halo) by the AO system. This angle, $\theta_c = N_{act} \lambda / 2D$, depends on the number of actuators across the diameter of the primary (Sivaramakrishnan et al. 2001). For Mt. Wilson, this area extends out to $8\lambda/D$ so a design with an IWD of closer to $4\lambda/D$ or less would be ideal.

Ground based observations are also limited by the contrast ratio of the uncorrected halo to the core (z_{halo}). The FWHM of the halo is approximately the uncorrected seeing, which typically is $> \theta_c$. In that case, a good estimate of the best contrast achievable is simply the ratio of the peak intensity of the uncorrected halo to the peak intensity of

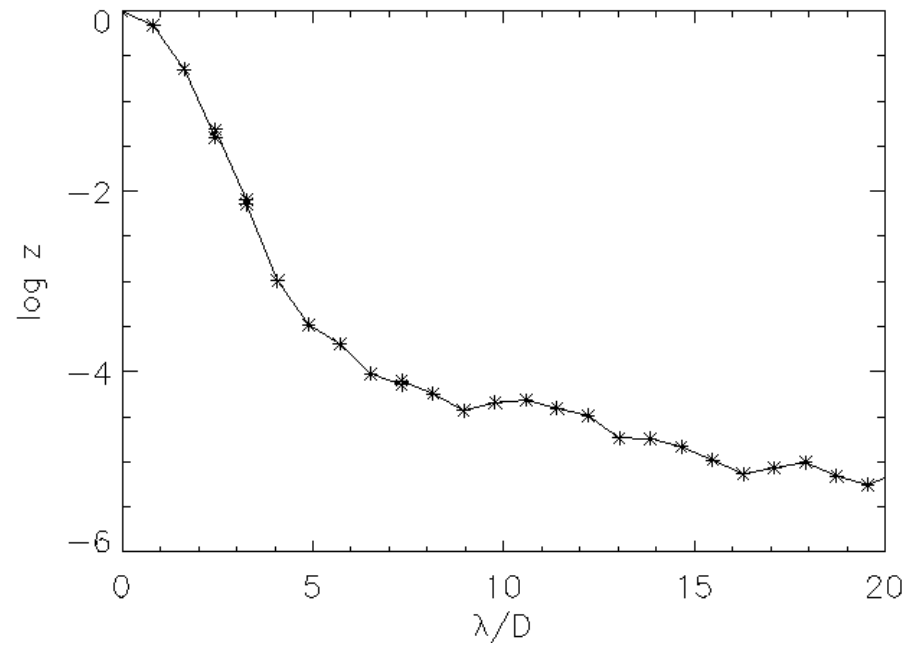


Fig. 5.5 Azimuthally averaged PSF of the single aperture design in the J band. I achieved 4×10^{-5} contrast at $10\lambda/D$. Truncation of the mask during fabrication is the main degradation of contrast with what would be theoretically possible.

the corrected image core (Hardy 1998):

$$z_{\text{halo}} = \frac{1 - S}{1 + \left(\frac{D}{r_o}\right)^2}, \quad (5.17)$$

where S is the Strehl Ratio, r_o is the Fried Parameter of atmospheric turbulence, and D is the diameter of the telescope. Roberts & Neyman (2002) have reported S values of ~ 0.2 for the AEOS telescope in the visible ($0.55 \mu\text{m}$) for an $r_o \sim 12$ cm, giving an approximate contrast of 10^{-3} . In this case, larger telescopes gain an advantage in contrast given the same seeing conditions and ability to attain a certain Strehl ratio. Higher order adaptive optics will need to correct to very high levels ($S \sim 0.9$) to successfully achieve a high contrast with a GAPM. However, using a more modest α with a more modest level of high contrast may present a useful alternative to a coronagraph for groundbased searches with AO. Example would be a search for substellar companions in a dense young cluster or a search for faint companions to white dwarfs such as what was described in Chapters 3 and 4.

5.2 Notch-Filter Masks

5.2.1 Introduction

Directly imaging extrasolar terrestrial planets in reflected light requires facing the extremely high predicted contrast ratios between planets and their host stars, e.g., $\sim 10^{-10}$ for an Earth analog orbiting a solar type star at quadrature. A planet-finding coronagraph must realize this contrast within a few diffraction widths (λ/D , where λ is the wavelength of light, and D is the long axis of the primary mirror) of the stellar image. Though several coronagraph designs can achieve this contrast according to scalar diffraction theory (Kuchner & Spergel 2003a), substantial work on mask design and laboratory investigation probably remains before this contrast can be achieved in practice.

Some coronagraph designs use image-plane masks to absorb on-axis light and diffract it away (Malbet 1996; Sivaramakrishnan et al. 2001; Kuchner & Traub 2002). Other designs use shaped or apodized pupils which benefit from combining aperture shape and the pupil intensity distribution to remove the wings of a circular aperture's PSF (Kasdin et al. 2003; Vanderbei et al. 2003; Debes et al. 2002, 2003; Ge et al. 2002). Image masks offer the advantages that they explicitly remove starlight from the beam, and that they can provide high contrast at small angles from the optical axis, given sufficient control over low-spatial frequency modes.

Scattered light, wavefront errors, and mask construction errors can all degrade the contrast of a coronagraph. For example, for any coronagraphic image mask, mid-spatial frequency intensity errors near the center of the mask must be $\lesssim 10^{-9}$ (Kuchner & Traub 2002). Some of these errors can be controlled using active optics, but these corrections will necessarily apply only over a limited range of wavelengths.

Notch-filter masks offer a promising choice for planet-finding coronagraphs (Kuchner & Spergel 2003c). These image masks absorb most of the light from an on-axis point

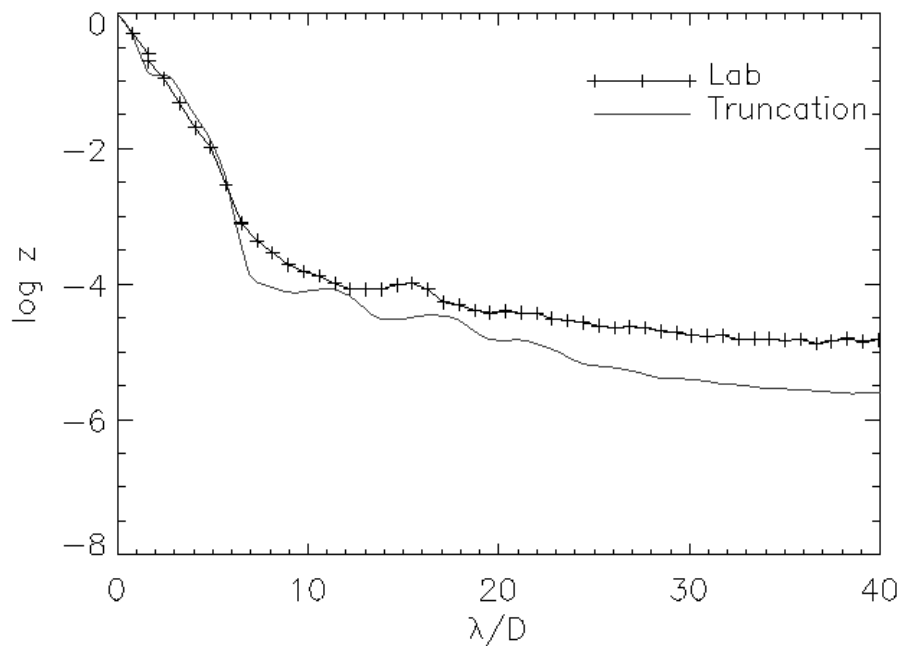


Fig. 5.6 A comparison between the J band PSF and a model based on the truncation of the Gaussian contour's wings described in Equation 5.16. For the model I used $\beta=13$ and the parameters listed in Table 5.1 for the Mt. Wilson design. Both the model and the lab data were azimuthally averaged for 20° about the high contrast axis.

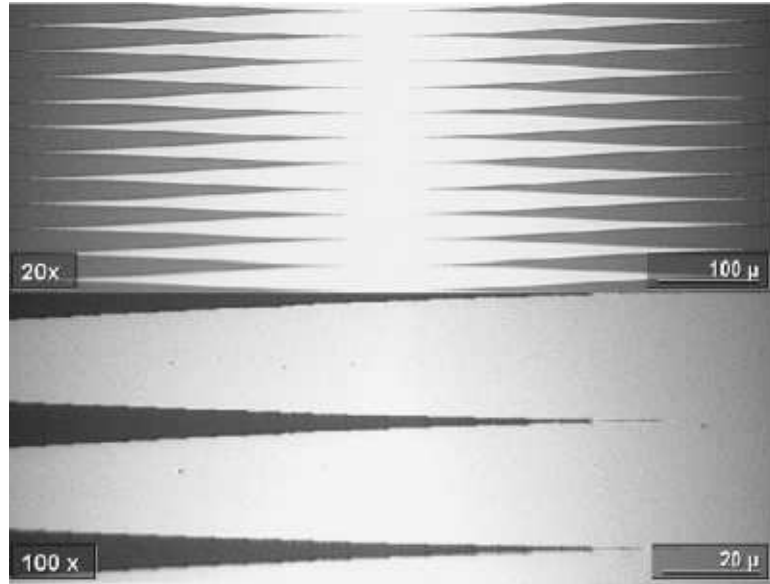


Fig. 5.7 Optical microscope images of the final mask design.

source, and diffract all of the remainder onto a matched Lyot stop. While Lyot coronagraphs with Gaussian image masks must have a throughput of $\lesssim 1/2$ to reach 10^{-10} contrast, linear notch-filter masks have unlimited dynamic range according to scalar diffraction theory, and a throughput of $\sim (1 - \epsilon)$, where ϵ is typically $\sim 0.3 - 0.5$.

Other coronagraph designs besides notch filter masks can create perfect subtraction of on-axis light. However, those designs based on masks with odd symmetry (Rouan et al. 2000; Riaud et al. 2001) or interferometrically synthesized masks with odd symmetry (Baudoz et al. 2000a,b) create nulls that degrade as θ^2 , where θ is the angle from the optical axis. This rapid degradation means that the finite size of a real star causes the coronagraph to leak light at levels unsuitable for terrestrial planet detection. Other designs, like the dual phase coronagraphic mask with an apodized entrance pupil (Soummer et al. 2003a,b), produce the needed null depth, but must use masks with special chromatic behavior and require precise, achromatic aperture apodization. Notch-filter masks are intrinsically achromatic and like the dual phase coronagraph, they create nulls of order θ^4 or slower (Kuchner & Traub 2002).

Notch-filter masks can be designed such that they are binary—regions of the mask are either opaque or transparent. This is a great advantage as intensity errors are not an issue so long as the mask is sufficiently opaque, leading to manufacturing constraints that are orders of magnitude smaller. However, the shape of the mask must be precisely reproduced, to the level of $\lambda f_{\#}/3600$ for a contrast of 10^{-10} within the search area. For an instrument with $f/100$ and working $\lambda \sim 0.66\mu\text{m}$, this corresponds to a tolerance on the order of 20 nm. Nanofabrication techniques are required to reach this precision.

As part of a joint university-industry study partly funded by Ball Aerospace and in collaboration with the Penn State Nanofabrication facility (Nanofab), I have fabricated a prototype notch-filter mask and tested it in an experimental setup. I discuss briefly the mask fabrication process in Section 5.2.2, describe methods for modeling performance in Section 5.2.3, and review the experiments and results in Section 5.2.4.

5.2.2 Mask Design and Fabrication

Following the prescription laid out in Kuchner & Spergel (2003c), I designed a notch-filter mask based on a $1 - \text{sinc}^2$ band limited function. The mask is a vertically repeating pattern of opaque curves described by:

$$\hat{M}_{BL}(x) = \pm 0.5 \frac{\lambda_{min}}{D} \left[1 - \text{sinc}^2 \left(\frac{\pi \epsilon x D}{2 \lambda_{max}} \right) \right] \quad (5.18)$$

where ϵ is used to determine the half power of the mask, the effective distance where a companion could reasonably be detected, λ_{min} and λ_{max} are the minimum and maximum wavelengths of the spectral band of interest. In reality the mask is constructed and therefore sampled at some resolution, i.e. with a nanofabrication tool, such that the band limited equation is modified slightly;

$$\hat{M}_{samp} = \Pi \left(\frac{x}{w} - n \right) \star \hat{M}_{BL}(n) \quad (5.19)$$

where n is over all integers, w is the resolution of the tool, and Π is the tophat function. The final step is to convolve \hat{M}_{samp} with a series of δ functions spaced by λ/D to produce the mask function:

$$\hat{M}_{notch} = \sum_{k=0}^N \delta \left(y - \frac{k\lambda}{D} \right) \star \hat{M}_{samp} \quad (5.20)$$

Repeating the band limited curve on scales $\lesssim \lambda/D$ ensures that the notch-filter mask becomes a good approximation of a transmissive mask for spatial frequencies in the pupil plane $< D/\lambda$.

I designed the mask for a f/158 system and a working wavelength of $0.633 \mu\text{m}$. My choice of ϵ was 0.46, to allow an inner working distance of 2-3 λ/D . For my working wavelength, the maximum size is $\sim 100 \mu\text{m}$. While the theory prescribes that the width of the stripes be no wider than $\lambda_{min} f_{\#}$, there is no prohibition from making the width smaller and so I built the mask with stripes of width $25 \mu\text{m}$. There are two advantages to undersizing—one is guarding against blue light leakage in a broadband case and the other is allowing future tests to be performed at smaller $f_{\#}$.

The Leica EBPG5-HR EBL tool available at Nanofab can produce resist features down to a minimum size of $\sim 20 \text{ nm}$ with a precision of $\pm 5 \text{ nm}$ for high resolution resists. The features are placed to an accuracy of $< 35 \text{ nm}$ over a 125 mm writing area. The EBL resist was developed on a commercially supplied quartz substrate, covered by a layer of chromium that served as the opaque parts of the mask. Figure 5.7 shows the final mask under 20x and 100x optical magnification.

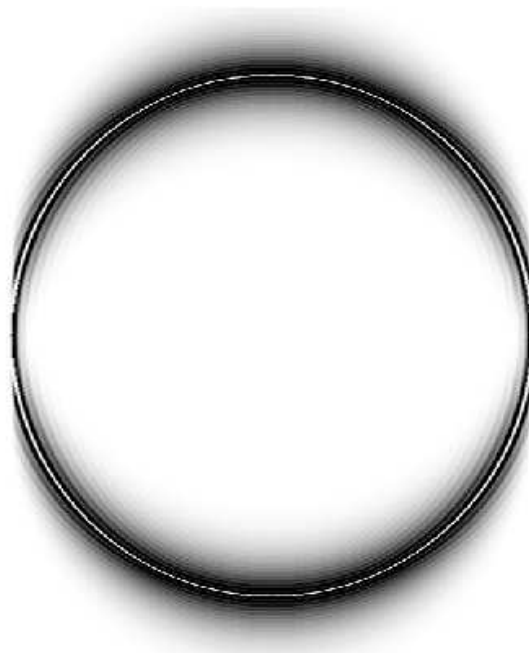


Fig. 5.8 A model of the light distribution in the pupil plane prior to a Lyot stop of a notch-filter mask design with an $\epsilon=0.46$, at the working wavelength of $0.633 \mu\text{m}$.

The resolution used for the EBL tool was $.25 \mu\text{m}$. Errors in the mask shape produce a leakage of light with an intensity of $0.25 h^2$ where h is the size of the error measured in diffraction widths (Kuchner & Spergel 2003c). Based on the EBL tool resolution, my mask should be capable of producing manufacturing-error-limited contrasts of 1.5×10^{-6} without the use of an apodized Lyot stop; with my choice of experimental setup and wavelength, achieving a deeper contrast of 10^{-8} at the peak would require 20 nm precision.

5.2.3 Modeling the Performance of the Mask

One would like to know in advance how the mask responds to different sources of error. It is also instructive to try and reproduce the actual performance of the fabricated mask in an attempt to understand the major sources of error in the experimental setup. However, modeling the resulting diffraction pattern requires the use of numerical methods such as Fast Fourier Transforms (FFTs) which are not adept at accurately handling simultaneous high resolution in both the imaging and pupil planes (Brigham 2003).

Modeling the resultant scalar diffraction pattern or point spread function (PSF) of an optical system can be summed up in the following combination of the wave amplitude PSF of the original aperture \hat{A} , the mask function \hat{M} , and the Fourier Transform of the Lyot Stop aperture function \hat{L} :

$$\hat{A}' = \hat{A}\hat{M} \star \hat{L} \quad (5.21)$$

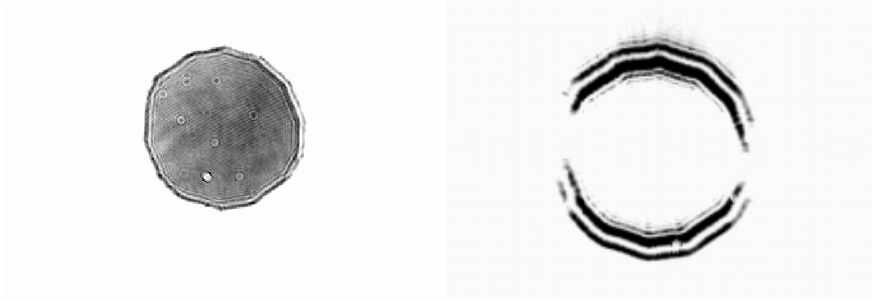


Fig. 5.9 A comparison between pupil images of the testbed with no mask (left) and with a mask centered (right).

where the star denotes convolution. The numerical problem arises when the arrays that represent \hat{A} and \hat{L} typically are Nyquist sampled, corresponding to $\lambda/2D$, on order of the *maximum* scale of the mask function. To avoid this, I rely on the fact that the Fourier Transform of \hat{M} is semi-analytically described so that I can construct an accurate, coarsely sampled array that can then be used in the model. The Fourier Transform of \hat{M} , $M(u, v_o)$ at a particular value of v_o is given by

$$M(u, v_o) = \int_{-\frac{1}{2}}^{\frac{1}{2}} \frac{\sin(\pi v_o \hat{M})}{\pi v_o} \exp(2\pi i u x) dx \quad (5.22)$$

In this way M can be built up using a 1D FFT that is faster and more accurate than its two dimensional analogue. The final intensity at the image is given by $|\hat{A}'\hat{A}'^*|$. Figure 5.8 shows the light distribution before the Lyot Stop for the notch-filter mask I designed assuming no errors and a circular entrance pupil.

5.2.4 Experiments and Results

The testbed used at Penn State was designed to test many different coronagraph and shaped pupil designs. I used a HeNe laser as the light source and approximated a point source by placing a microscope objective lens in front of the laser and placing the focused image on the entrance aperture of a single mode fiber. Light exiting the fiber was collimated, followed by an ~ 3.16 mm entrance aperture. An image was formed at the focal plane image masks, which were mounted on a precision x-y-z stage. The light was then re-collimated and passed through a Lyot stop at an image of the entrance pupil. Lastly, the light was focused onto the CCD detector, where the final image was formed. The largest possible Lyot stop permitted by the linear mask design I chose would have been shaped like the overlap region of two circles (Kuchner & Traub 2002). Instead, for convenience, I used an iris as a Lyot stop. The final diameter used for the experiments was 1.8 mm. This diameter is 75% of what would be expected theoretically. I discuss the possible explanation for this in Section 6.3.

In order to measure a contrast ratio for any point in the PSF of the unblocked point source or of the point source behind the mask, the counts in a particular pixel must be normalized to the peak pixel counts of the unblocked point source for a given exposure time. Ideally, one would measure the counts with the mask out and in for the same exposure time. The deepest contrast one can achieve with this method is limited by the nonlinearity of the CCD, in my case $\sim 20,000$ ADU. For a $S/N > 5$ in a particular pixel, this level would correspond to a contrast of only 1.2×10^{-3} . To measure deeper contrasts, one must take longer exposures of the blocked point source and normalize the results to an extrapolated count rate for the unblocked source.

To obtain reliable estimates of the count rates and fluxes of the different configurations I observed the PSF over a range of linearly increasing exposure times, taking care to avoid saturating the image. I measured the peak pixel and total flux in each exposure using the IRAF task IMEXAM. I averaged the results and fit a linear model to them using a least squares fitting routine in IDL called LINFIT. By extrapolating to a specific exposure time, a normalization for observations with the notch-filter mask could be obtained.

I repeated this procedure for the point source through the quartz substrate of the notch-filter mask, with no substrate present, and with the Lyot stop completely open in order to determine the transmission of the substrates and the throughput of the Lyot stop. My reported results for the notch-filter mask are scaled to the peak pixel count rate of the unblocked point source through the substrate. I used the other measurements to gauge the throughput of the quartz substrate and the Lyot stop.

In the setup I also took observations of the pupil image both with and without the mask, to gauge how well qualitatively the mask worked compared to what is predicted by scalar diffraction theory. Figure 5.9 shows that with the mask in place, the pupil qualitatively resembles what is predicted by my model in Figure 5.8. Note that both pupils in Figure 5.9 are at the same scale and that the bulk of the light falls outside the original pupil.

Once the peak pixel count rates and fluxes were measured, deep observations of the notch-filter mask were taken. Figure 5.10 shows two images set to the same contrast level and normalized to the same exposure time. The top image is one of the point source without the notch-filter mask in place, while the bottom image is an exposure with the mask centered.

The bar at the bottom shows the number of counts on the detector associated with each level of the greyscale. As can easily be seen, the diffraction pattern of the light source is diminished greatly.

Figure 5.11 demonstrates a more quantitative comparison with the mask present and absent and the undersized Lyot Stop in place for both configurations. The figure shows the images taken during my experiments azimuthally averaged over all angles except for 20° on either side of the notch-filter's mask axis to avoid the region completely blocked by the mask. The curves are normalized to the peak pixel count rate of the unblocked image. I have converted the spatial scale in pixels to units of λ/D by multiplying by a factor of $l_{pix}/(\lambda f_{\#})$, where l_{pix} is the width of a pixel in μm . By doing this, one can scale my results for existing or future telescopes. It is important to note that this scale reflects the degradation of spatial resolution due to a Lyot Stop that is undersized. The



Fig. 5.10 (top) 10 second image of the laser point source without the mask in place. (bottom) Image with same intensity stretch with the mask in place. The peak pixel value of the bottom image is 2.8×10^5 ADU.

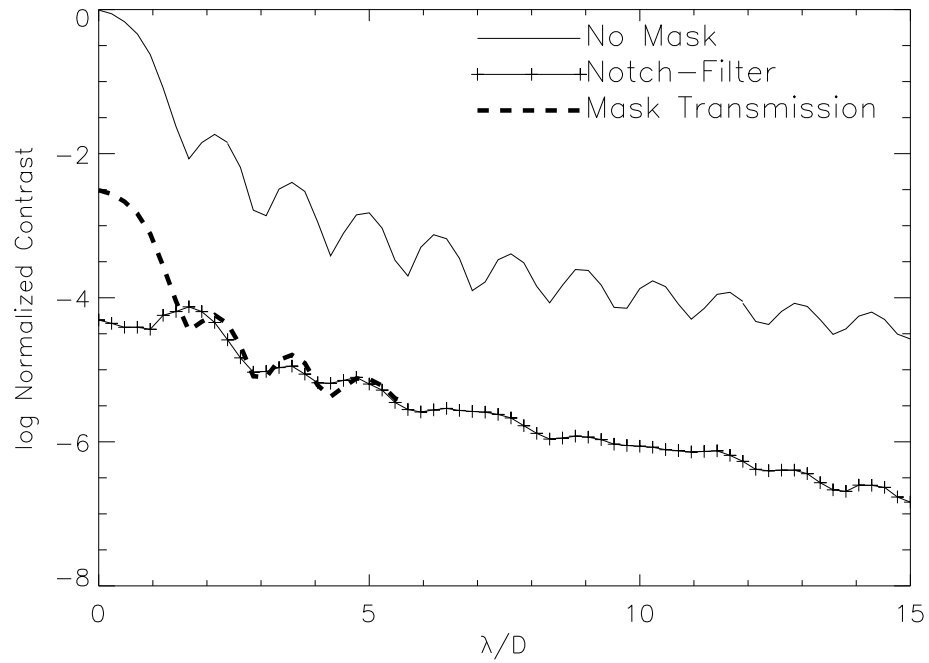


Fig. 5.11 Comparison between the unblocked point source, the notch-filter mask, and mask transmissivity. Each image was azimuthally averaged to within 20° of the notch filter mask axis.

diffraction pattern is clearly suppressed by at least 2 orders of magnitude within $10\lambda/D$, with a contrast of 9.5×10^{-6} reached at $3\lambda/D$. In the course of my experiments I found that the mask was not completely opaque, allowing a small fraction of light transmission. I measured the magnitude of this mask transmissivity (MT) as well with the Lyot Stop in place and show it in Figure 5.11 for comparison. It appears that most of the residual light corresponds to the wings of this transmission.

Table 5.2 allows us to compare the relative throughput of the notch-filter mask to a setup without a Lyot stop. I define throughput as the ratio of flux for a certain design to the flux of the system with a completely open Lyot stop and no mask in place. I also measured the point source through the quartz substrate of the mask. As can be seen, the throughput of the notch-filter mask+Lyot stop combination is $\sim 27\%$.

Table 5.2. Experimental Fluxes and Peak Count Rates

Configuration	Flux (ADU s ⁻¹ cm ⁻²)	Peak Pixel Count Rate (ADU s ⁻¹)
Notch-filter glass	7×10^8	2.2×10^6
No Mask	8.0×10^8	2.4×10^6
No Mask, No stop	2.6×10^9	1.9×10^7
Mask Transmissivity	2.3×10^6	7.2×10^3

Chapter 6

Conclusions

6.1 The Scenario of Post Main Sequence Evolution for Planetary Systems

By performing numerical integrations of two planet and multiple planet systems, I have shown that the stability of a system changes with mass evolution. In the specific case of mass loss as the central star of a planetary system becomes a white dwarf, I have found that previously marginally stable orbits can become unstable fairly rapidly after the mass loss process. Coupled with my knowledge of the survival of material exterior to outer planets such as Kuiper Belt and Oort Cloud analogues (Stern et al. 1990), a picture of the evolution of circumstellar material over the latter stages of a star's lifetime becomes clear.

As a star reaches the RGB and AGB phases, inner planets are engulfed by both the expanding envelope of the star and through tidal dissipation. The surviving planets move slowly outwards, conserving their angular momentum as the star loses its mass over several orbital periods of the planets. The planets may sculpt the resulting wind of the giant star (Soker 2001) and if they are on the very edge of stability, undergo chaotic episodes during the AGB phase, creating some of the more exotic morphologies in the resulting planetary nebula. When the star becomes a white dwarf, two planet systems that are marginally stable will become unstable and suffer close approaches, while for three or more planets the timescale to close approaches shortens by orders of magnitude. There are three possible outcomes once the planets start suffering close approaches: the planets collide, one planet is ejected, or the two planets remain but are in highly eccentric orbits (Ford et al. 2001). One major open question is how many marginally stable systems there are, but there are indications that many, if not most, general planetary systems should be close to instability (Barnes & Quinn 2001; Laughlin & Adams 1999; Quinlan 1992; Rivera & Lissauer 2000; Barnes & Quinn 2004). Rocky material in the inner edge of the Kuiper Belt, which is defined by the last stable orbits with respect to the planetary system, will follow the same fate as marginally stable planets, suffering close approaches with the planetary system and becoming scattered into the inner system. After the comets are scattered into the inner system the rate of close encounters with planets or the central white dwarf increases. The surviving material at outer Kuiper Belt and Oort Cloud distances will have orbital periods comparable to the timescale of the central star's mass loss. These objects have their eccentricity pumped up by the effectively instantaneous change in the central star's mass, and then through interactions with planets create a new dust disk around the white dwarf, contaminating the white dwarf photosphere to an observable extent.

6.2 The Prospects for Finding Cool Companions in the Stellar Graveyard

In Chapters 3 and 4 I have shown that a combined approach to observing individual nearby white dwarfs for planetary mass companions is preferable. Through this technique I can probe planetary orbits not accessible by other methods. Any planet discovered could become an important spectroscopic target for follow-up. The information gleaned from a large scale version of this study may provide key information on

planet formation and evolution in intermediate mass stars as well as providing a possible explanation for the origin of white dwarfs with metal absorption (Debes & Sigurdsson 2002).

A volume limited survey of WDs out to a certain distance would be a logical extension of this work. Such a study would require several components that are currently or partly accomplished, including:

- Reliable models of nearby white dwarfs' cooling ages and masses, as well as accurate parallaxes. The study of Bergeron et al. (2001) is a good example of such modeling that would aid a planet search.
- Sensitive Mid-IR photometry of white dwarfs, such as with *Spitzer*, to provide stricter limits on unresolved companions.
- High resolution, high contrast near- or mid-IR imaging to resolve companions in orbits $> 5\text{-}10$ AU where I would expect Jovian planets.
- Pulsational timing/eclipse surveys/radial velocity campaigns to provide a sensitive connection between those techniques and high contrast imaging.

I have found a candidate extrasolar planetary companion which has been refuted by second epoch measurements, plus several candidates that still need follow-up. While no bona fide planets have been confirmed, the detection of candidates proves that this technique is feasible. In addition, thanks to a combination of ground and space based observing, I can place strict upper limits on the presence of planets for DAZs and field WDs.

6.2.1 DAZ White Dwarfs

I can use Table 4.4 and the results of my excess limits to draw some broad conclusions from this search. The combination of the 2MASS excess determinations and the HST imaging create the most sensitive search for planets around WDs to date. The sensitivity achieved could easily have detected an object $>10 M_{Jup}$ at separations >30.6 AU, with the closest detection possible at 9.3 AU. Taking into account that any primordial companions' semi-major axis would have expanded by a factor of M_i/M_f , we can infer the closest primordial separation these objects would have had if they had been detected. Taking the values of Table 4.1 for M_i and M_f and using my minimum projected angular separation, I find that any object that formed at >10 AU could have been detected, assuming that there were no forces that retarded expansion. Forces that could retard expansion would be due to tidal interactions with the giant star. However, this effect should be minimal at initial distances of 10 AU (Rasio et al. 1996).

I can also make some initial comments about the origin of DAZ white dwarfs. Given the upper limits on unresolved companions, I can infer the plausibility of one of the possible explanations for the DAZ phenomenon. The problems with ISM accretion have been documented extensively in previous work (Zuckerman et al. 2003; Aannestad et al. 1993). Zuckerman et al. (2003) noted that a large fraction of DA/dM objects had metal absorption lines in their atmospheres, and inferred that other DAZs may be the

result of unseen companions. If this scenario is true, then for each of these objects, the maximum companion mass plausible is $56 M_{Jup}$ for 5 of the seven targets and $72 M_{Jup}$ for the rest.

If the explanation for DAZs is due to close brown dwarf companions, the frequency of DAZs is at odds with the frequency of DAZs one would predict based on radial velocity surveys. These surveys find that $\sim 0.5\%$ of stars have brown dwarfs with semi-major axes < 3 AU (Marcy & Butler 2000). One would expect 0.5% or less of field DAs to be DAZs based on the radial velocity result. The only possible counter explanation is that brown dwarf formation at these radii is ~ 40 times more efficient for higher mass main sequence stars. Radial velocity surveys of G giants are too young to reliably estimate the fraction of brown dwarf companions in orbits wider than ~ 1 AU, but none have yet been found in ~ 100 stars. (Sato et al. 2003).

I can compare my results with the predicted frequency of planets found in radial velocity surveys, even though my results and those of the radial velocity surveys probe fundamentally different semi-major axes. Since the numbers are small, I will merely look at percentages and assume that they are constant as a function of distance and central stellar mass, clearly naive assumptions. Since 5% of field stars have planetary systems, I need to estimate how many would have planets massive enough to be detected by my observations. Of the 118 known planetary systems in orbit around solar type stars, ~ 6 have companions with $M \sin i > 10 M_{Jup}$ ¹. The frequency of such planets amongst stars already bearing one or more planets is then $\sim 5\%$, leading to an overall probability of 0.25% of all field stars possessing a planet that I could have detected. Assuming Poisson statistics, to have a 50% chance at detecting one or two planets would require a sample of 400 WDs with ages ~ 3 Gyr. As mentioned earlier, G giants can be used as a proxy for detecting planets around A stars. G giants are typically intermediate mass stars, although field giants tend to have larger uncertainties in their mass compared to the main sequence stars in other radial velocity surveys. As of the results published in Sato et al. (2003), one planetary object with $M \sin i = 6-10 M_{Jup}$ and semi-major axis ~ 1 AU had been detected in a sample of ~ 100 targets. The implied frequency of $\sim 1\%$ would mean a slightly more favorable chance to find one planet in a sample of ~ 100 WDs. If DAZs do not preferentially harbor planetary systems, it would be a long search if I only focus on them. Any search should include DAZs, but also focus on a larger sample. While one cannot glean any deeper meaning from this extrapolation, it demonstrates the target sample size one should consider for future surveys of field WDs.

Let us now consider the possibility that DAZs do preferentially harbor planetary systems, and based on my detection limits, determine how many DAZs would need to be observed. Since I could detect $> 10 M_{Jup}$ objects and $\sim 5\%$ of field stars with planetary systems have objects that massive, I can infer that 5% of DAZs could have planets that could have been detected. If DAZs (and also DZs or helium white dwarfs with metal absorption) are indeed good markers for planetary systems, one would need a sample of 20 WDs to have a 50% chance to detect a massive planet. To date ~ 34 DAZs are known. Currently the estimated fraction of apparent single WDs that are DAZs are $\sim 20\%$; if they all harbor planets this implies a much higher frequency of planets than that measured

¹<http://www.obspm.fr/encycl/encycl.html>

by radial velocity surveys. However, radial velocity surveys are starting to detect longer period systems, which may have a higher frequency of formation and better represent the type of population that would cause a DAZ (Jones et al. 2002). There exists a real possibility that DAZs have planetary systems that preferentially *do not* have planets more massive than $1M_{Jup}$. Massive planets are most likely too efficient when forming to leave a significantly large Oort cloud analogue (Hansen 2004). Conversely, such objects may be too efficient at removing any remaining cloud, so that contamination occurs early and fades quickly from a WD atmosphere. If this hypothesis is true, it may not be surprising that no firm candidates were found in this search. One would hope to get the massive planets for free, since DAZ forming planetary systems need at least two constituent planets.

There are then two approaches to continuing the search—increasing the sample size and increasing the sensitivity of a search. In the short term a large sample of WDs must be observed, since the probable frequency of massive planets among WDs that harbor a planetary system is small. Future observatories such as the James Webb Space Telescope should have an easier time detecting Jovian and sub-Jovian planets, which will hopefully resolve the origin of DAZs and whether they are ultimately useful for planetary studies, including spectroscopy if any candidates are confirmed.

The discovery of candidate planetary mass companions demonstrates that this limited survey was sensitive to planets. These results show that if massive planets were present around these WDs I would have detected them. Even with a small sample, limits can be placed on the frequency of massive planets in orbit around stars more massive than the Sun, and begin to observationally address the question of planet formation efficiency vs. spectral type. Ideally, the next step would be to expand the sample of WDs studied and to probe to lower masses, where the planetary mass function peaks ($\sim 1 M_{Jup}$). High spatial resolution and sensitivity missions like JWST would most likely be able to detect such objects.

For WD 2326+049, the sensitivity of my Gemini observations allows us to place some strong conclusions on previous claims for the presence of close companions due to pulsational timing by Kleinman et al. (1994) and the presence of spatially resolved structure to WD 2326+049 by Haas & Leinert (1990). If WD 2326+049 is 1 Gyr old I can refute the presence of a companion at ~ 3.4 AU. I can place limits on its mass if WD 2326+049 is older. The possibility exists that the companion could be closer to WD 2326+049 than its maximum extent. However, if one looks at the timing of maximum extent from the star, I am at precisely the time when the companion would be furthest in its projected orbit. But I see no evidence for a companion beyond some structure in the AO PSF at a projected separation that does not match the predicted orbital separation (Trujillo 2004, personal communication). Additionally, my Gemini data was of high enough spatial resolution that I should have easily detected extended structure similar to what was reported in Haas & Leinert (1990). I see no such structure in any of my HST or Gemini observations. Any dust disk present around G29-38 must be confined to smaller than 72 mas or 1 AU projected separation.

6.2.2 Field White Dwarfs

I have surveyed thirteen white dwarfs for substellar objects. From this search I have found two potential candidates both around the white dwarf WD 2341+321. This star requires follow-up observations to confirm or refute these candidates. If any of the companions is confirmed to be co-moving, they are dim enough to be consistent with planetary mass objects. With putative absolute magnitudes in the H band of ~ 21 - 22 , these would be hard to confuse with higher mass objects such as in young stellar populations (Mohanty et al. 2004).

6.2.3 Upper Limits to the Presence of Substellar Objects for the Whole Sample

To date, nine hydrogen white dwarfs with metal lines, so-called DAZs, have been searched for substellar objects—seven from my observations with HST and two from the ground. WD 1633+433 and WD 1213+529 both have been found to have small amounts of metals such as Ca in their atmospheres (Zuckerman et al. 2003). WD 1213+529 has an unresolved stellar companion, while WD 1633+433 appears from its 2MASS photometry and my imaging to be devoid of anything $> 12 M_{Jup} > 15$ AU away and $> 48 M_{Jup}$ at separations < 15 AU. Given that $\sim 25\%$ of DAs have measurable metal lines and their explanation seems less likely due to ISM accretion and more due to unseen companions, either substellar or planetary, they are interesting targets for faint companion searches (Zuckerman et al. 2003; Debes & Sigurdsson 2002).

Using a binomial type distribution that has been used to calculate the frequency of brown dwarf companions to nearby stars, I can calculate limits to the frequency of substellar objects around DAZs as well as my full sample of 20 white dwarfs (McCarthy & Zuckerman 2004). That distribution is given by

$$P(f, d) = f^d (1 - f)^{N-d} \frac{N!}{(N - d)!d!} \quad (6.1)$$

where P is the probability, f the true frequency of objects, N the number of observations, and d the number of successful detections.

If one integrates over all the probabilities, one can derive limits that encompass 68% of the distribution. From these limits I can compare my results with both the radial velocity surveys and imaging surveys for brown dwarfs. In this study I can place meaningful limits to planet and brown dwarf formation around stars that originally had masses between $1.5M_{\odot}$ - $7M_{\odot}$, the range of initial masses inferred for my targets. From my limit of $\sim 1''$ as the innermost separation where I could have detected a companion for all of my targets, I can derive an innermost projected orbital separation that I probed. Since any companion that is found today in an orbit with semi-major axis a had a primordial orbit M_f/M_i times smaller before the star lost its mass and turned into a white dwarf, I can probe inwards to regions that should have been sites for planet formation. With a subset of my targets sensitive to planetary mass objects at separations that would be where planets with orbits like Jupiter would be found I can study a region of parameter space complementary to radial velocity surveys (Marcy & Butler 2000).

For my samples I neglect WD 0501+527 and WD 1213+529, since the observations of these targets are significantly less sensitive than the other observations. Of the 18 remaining WDs from the DSW05b and CFHT samples, eight are DAZs and the rest are a mixture of other white dwarf spectral types including DAs with no detectable metals in their atmospheres.

In my DAZ sample, the images of five WDs were sensitive enough to detect planets, and none were found. Therefore, they do not have planetary mass objects $> 10 M_{Jup}$ at projected separations > 21 AU, corresponding to an inferred minimum primordial separation of > 6 AU. When I integrate over all possible probabilities I get an inferred limit of $< 17\%$ for the frequency of massive planets in orbit around DAZs. Assuming that every DAZ may possess a planetary system, this is within a factor of 3 to the frequency of massive planets discovered with the radial velocity surveys with $M \sin(i) > 10 M_{Jup}$, where 6 of 118 discovered planetary systems² possess such companions $< 5-6$ AU as well as radial velocity surveys of G giants (Marcy & Butler 2000; Sato et al. 2003). Furthermore, none of the eight apparently single DAZs showed the presence of companions $> 72 M_{Jup}$ in close, unresolved orbits. This implies that $< 12\%$ of DAZs have companions that are stellar. Any unseen object that could pollute a WD would have to be substellar for the majority of current apparently single DAZs.

For my total sample of 18 WDs, I can also place limits on any object $> 18 M_{Jup}$ present at projected separations > 34 AU and corresponding to a minimum primordial orbit of > 10 AU. From zero detections in this sample, I infer that intermediate mass stars from between $1.5-7 M_{\odot}$ have brown dwarf companions $< 6\%$ of the time.

High spatial resolution imaging of white dwarfs will also be important as supporting observations for Spitzer observations of white dwarfs that are looking for mid-IR excesses due to substellar companions. WD 1121-216 in particular may falsely show an excess due to it temporarily being coincident with a background galaxy. Approximately 100 WDs have been approved to be observed with Spitzer in the Cycle 1 GO programs. A combination of the Spitzer photometry and imaging would provide a more sensitive test for unresolved companions while providing a check against source confusion due to Spitzer's larger PSF with the IRAC camera, for example (Fazio et al. 2004). A large survey like that would also start placing rigorous limits on the presence of faint companions to nearby white dwarfs.

6.3 Future Technologies for High Contrast Imaging

I have performed several simulations, lab tests, and telescope observations with GAPMs in order to better understand the interplay between theory and the reality of observations. GAPMs alone provide an improvement over a simple circular aperture for quick high contrast imaging. They are very sensitive to an accurate reproduction of shape and thus need accuracies that require nanofabrication techniques such as e-beam lithography, similar to what has been used for notch-filter masks (Debes et al. 2004). I have commissioned some precise GAPMs with accuracies on the order of $0.25 \mu\text{m}$ which should lead to a more accurate shape reproduction and a minimization of errors.

²<http://www.obspm.fr/encycl/encycl.html>

Precisely fabricating these masks can potentially improve performance to the ideal limit for a mask provided it is above the scattered light limit of the telescope, bringing it in line with Lyot coronagraphs of comparable throughput. Demonstration of these masks in conjunction with an adaptive optics system could present a workable example of a quick way to survey for faint companions without needing to incur the overhead cost of precise alignment behind a coronagraphic image mask.

Similarly, I have tested extensively the notch-filter mask. My experiments did not attain the mask performance levels expected from scalar diffraction theory. Here I will quantify the effect of some errors that degraded the contrast and speculate on the potential uses of this mask for space-based planet searches.

Mask transmissivity (MT), the finite size of the point source, mask alignment errors, and mask fabrication errors all combine to explain the degraded performance of the notch filter mask. These effects can be estimated and collected into an error budget to guide further testing of the mask and drive improvements in my setup.

The MT for dark parts of the mask should be less than the contrast requirements. Degradation from light transmission can be estimated by assuming a λ/D by λ/D hole in the mask with fractional transmission f . The central intensity of the leakage would be $\sim 0.25f$ as found in Kuchner & Traub (2002).

The transmission flux measured in Table 2.1 is 3×10^{-3} times the unblocked point source, giving a transmission peak intensity of 7.5×10^{-4} . This is larger than what is observed at the center, but one can estimate what would be expected further away—the PSF is $\sim 10^{-2}$ the peak at the first Airy ring, which for the transmission gives an intensity of $\sim 10^{-5}$, which is more consistent with what is seen further from the center. The mask may not be uniformly transmissive and slightly thicker toward the center, which could account for the suppression of the peak core. The opaque parts of the mask are covered by a 105 nm thick layer of chromium; if this layer is doubled or tripled it will push the MT to $\sim 10^{-8}$.

If the error in alignment with respect to the mask is larger than the physical size of the point source, then the leakage is $\sim (\Delta\theta/\theta_{1/2})^4$, where $\Delta\theta$ is the error in alignment and $\theta_{1/2}$ is the half power position of the mask (Kuchner & Traub 2002). The size of my single mode fiber core, 5 μm , ensures that the leakage due to it is less than the leakage due to misalignment of the mask. I have measured the half power of the mask to be ~ 8 pixels or 192 μm in the focal plane. My precision stage had an estimated accuracy of $\sim 16 \mu\text{m}$, based on half the value of the smallest movement possible in the focal plane. The leakage would be $\sim 4.8 \times 10^{-5}$ that of the unblocked point source.

The surface roughness of my lenses will dictate the levels of scattered light I should observe and allow us to estimate the contribution of scattered light to the degradation in contrast. I measured the surface roughness of one of my lenses with a profilometer at Nanofab and obtained an estimate of the RMS roughness (see Elson & Bennett (1979)). Scattered light levels are $\propto \delta_{rms}^2$, assuming a collection of plane gratings that diffract (scatter) light into angles of interest. This formalism is for an opaque surface that reflects light. However, the results for a series of uncorrelated surfaces (i.e. an optical setup of many lenses) give similar results provided that the roughness is separated on scales $> 2\lambda$ (Elson et al. 1983). I find that the RMS roughness of the lens is 0.4 nm, which can be compared to the measured roughness of HST, ~ 5.5 nm. Therefore, I estimate that the

scattered light levels should be $\sim (\delta/\delta_{HST})^2$ less than that of HST, corresponding to a contrast level of $3 \times 10^{-7} (x/14.5)^{-2.19}$, where x is in multiples of λ/D (Brown & Burrows 1990; Malbet et al. 1995). This corresponds to a scattered light level of $\sim 9 \times 10^{-6}$ at $3 \lambda/D$ and 1×10^{-6} at $8 \lambda/D$. More accurate measurements and analysis are needed to better quantify the limitations of scattered light in the lab, as the above comparison is not necessarily accurate with such small scattering angles (Brown & Burrows 1990).

MT and scattered light dominate the source of errors at $\sim 3 \lambda/D$, which is consistent with what is seen in Figure 5.11. The resulting PSF with the notch-filter mask resembles the MT PSF, close to the PSF core, where the residual Airy Pattern of the MT dominates. Further from the core, the Airy pattern is less distinct, most likely due to speckles from light scattered from the microroughness of my lenses.

A Lyot stop of diameter ~ 2.4 mm should have sufficed for a contrast of 10^{-6} . Experimentally I found that an undersized Lyot stop with 75% the diameter of the theoretical design appeared more efficacious. This was based on an initial belief that the degradation was caused by excess scattered light or slight misalignments of the Lyot stop and the optical beam. In those cases, undersizing the Lyot Stop would compensate for low levels of leakage. However, since it is apparent that the main cause of the degradation in contrast is due to the MT, undersizing the stop simply reduces throughput.

The design “as-is” already could have significant science benefits in space. Observations at the scattered light limit of HST coupled with PSF subtraction (shown to give an improvement of contrast of around a factor of 50-100) could yield contrast levels of $\sim 10^{-7}$ (Schneider & Silverstone 2003b; Grady et al. 2003). For HST, the Lyot stop would need to be designed such that the central obscuration and support pads would be adequately blocked at a cost in throughput. The Lyot stop would be the overlap of three HST pupils, just as in the ideal case. If I assume that with sufficient integration time I can reliably detect planets at this contrast level, I can speculate how useful HST would be for a planet search. An instrument on HST optimized for coronagraphy could become a test bed for future TPF coronagraph technology. This setup would allow a limited extrasolar planet direct imaging survey around nearby stars and white dwarfs. As an example I consider my reported contrast at $3 \lambda/D$ in the J band on HST with PSF subtraction. Given the best results one could expect $\Delta J=17.5$ and observe 1 Gyr old $3 M_{Jup}$ planets 10 AU from their host stars out to 30 pc and a 10-100 Myr old $2 M_{Jup}$ at 6.3 AU around β Pictoris (Burrows et al. 2003).

Bibliography

- Aannestad, P. A., Kenyon, S. J., Hammond, G. L., & Sion, E. M. 1993, *AJ*, 105, 1033
- Alcock, C., Fristrom, C. C., & Siegelman, R. 1986, *Astrophys. J.*, 302, 462
- Allard, F., Wesemael, F., Fontaine, G., Bergeron, P., & Lamontagne, R. 1994, *AJ*, 107, 1565
- Allen, D. 1999, *Allen's Astrophysical Quantities*
- Althaus, L. G. & Benvenuto, O. G. 1998, *MNRAS*, 296, 206
- Armitage, P. J. & Hansen, B. M. S. 1999, *Nature*, 402, 633
- Bakos, G. Á., Sahu, K. C., & Németh, P. 2002, *ApJS*, 141, 187
- Baraffe, I., Chabrier, G., Allard, F., & Hauschildt, P. H. 1997, *Astron. Astrophys.*, 327, 1054
- . 1998, *A&AS*, 337, 403
- Baraffe, I., Chabrier, G., Barman, T. S., Allard, F., & Hauschildt, P. H. 2003, *A&AS*, 402, 701
- Barnes, R. & Quinn, T. 2001, *ApJ*, 550, 884
- . 2004, *ApJ*, 611, 494
- Baudoz, P., Rabbia, Y., & Gay, J. 2000a, *A&ApS*, 141, 319
- Baudoz, P., Rabbia, Y., Gay, J., Burg, R., Petro, L., Bely, P., Fleury, B., Madec, P.-Y., & Charbonnier, F. 2000b, *A&ApS*, 145, 341
- Becklin, E. E. & Zuckerman, B. 1988, *Nature*, 336, 656
- Bergeron, P., Leggett, S. K., & Ruiz, M. T. 2001, *ApJS*, 133, 413
- Bergeron, P., Wesemael, F., Lamontagne, R., Fontaine, G., Saffer, R. A., & Allard, N. F. 1995, *ApJ*, 449, 258
- Boss, A. P. 2000, *ApJL*, 536, L101
- Bragaglia, A., Renzini, A., & Bergeron, P. 1995, *ApJ*, 443, 735
- Brigham, E. 2003, *The fast Fourier transform and its applications* (Englewood Cliffs:Prentice Hall)
- Brown, R. A. & Burrows, C. J. 1990, *Icarus*, 87, 484

- Burgasser, A. J., Kirkpatrick, J. D., McElwain, M. W., Cutri, R. M., Burgasser, A. J., & Skrutskie, M. F. 2003, *AJ*, 125, 850
- Burgasser, A. J., Kirkpatrick, J. D., McGovern, M. R., McLean, I. S., Prato, L., & Reid, I. N. 2004, *ApJ*, 604, 827
- Burleigh, M. R., Clarke, F. J., & Hodgkin, S. T. 2002, *MNRAS*, 331, L41
- Burrows, A., Sudarsky, D., & Hubeny, I. 2004, *ApJ*, 609, 407
- Burrows, A., Sudarsky, D., & Lunine, J. I. 2003, *Astrophys. J.*, 596, 587
- Butler, R. P., Marcy, G. W., Fischer, D. A., Brown, T. M., Contos, A. R., Korzennik, S. G., & Nisenson, P. & Noyes, R. W. 1999, *ApJ*, 526, 916
- Chakraborty, A., Ge, J., & Debes, J. H. 2002, *AJ*, 124, 1127
- Chambers, J. E., Wetherill, G. W., & Boss, A. P. 1996, *Icarus*, 119, 261
- Chu, Y. H., Dunne, B. C., Gruendl, R. A., & Brandner, W. 2000, *astro-ph/0010469*
- Corbin, M. R., O'Neil, E., Thompson, R. I., Rieke, M. J., & Schneider, G. 2000, *Astrophys. J. Suppl. Ser.*, 120, 1209
- Cutri, R. M., Skrutskie, M. F., van Dyk, S., Beichman, C. A., Carpenter, J. M., Chester, T., Cambresy, L., Evans, T., Fowler, J., Gizis, J., Howard, E., Huchra, J., Jarrett, T., Kopan, E. L., Kirkpatrick, J. D., Light, R. M., Marsh, K. A., McCallon, H., Schneider, S., Stiening, R., Sykes, M., Weinberg, M., Wheaton, W. A., Wheelock, S., & Zacarias, N. 2003, *VizieR Online Data Catalog*, 2246, 0
- Debes, J. H., Ge, J., & Chakraborty, A. 2002, *ApJL*, 572, L165
- Debes, J. H., Ge, J., & Ftaclas, C. 2005a, in preparation
- Debes, J. H., Ge, J., Kuchner, M. J., & Rogosky, M. 2004, *ApJ*, 608, 1095
- Debes, J. H., Ge, J., Mandelowitz, C., & Watson, A. 2003, in *High-Contrast Imaging for Exo-Planet Detection*. Edited by Alfred B. Schultz. *Proceedings of the SPIE*, Volume 4860, pp. 138-148 (2003)., 138–148
- Debes, J. H. & Sigurdsson, S. 2002, *Astrophys. J.*, 572, 556
- Debes, J. H., Sigurdsson, S., & Woodgate, B. 2005b, (*ApJ*, submitted)
- . 2005c, *AJ*, submitted
- Delfosse, X., Forveille, T., Mayor, M., Perrier, C., Naef, D., & Queloz, D. 1998, *A&AS*, 338, L67
- Duncan, M. J. & Lissauer, J. J. 1997, *Icarus*, 125, 1
- . 1998, *Icarus*, 134, 303

- Dupuis, J., Fontaine, G., Pelletier, C., & Wesemael, F. 1992, *Astrophys. J. Suppl. Ser.*, 82, 505
- . 1993a, *Astrophys. J. Suppl. Ser.*, 84, 73
- Dupuis, J., Fontaine, G., & Wesemael, F. 1993b, *Astrophys. J. Suppl. Ser.*, 87, 345
- Elson, J. M. & Bennett, J. M. 1979, *Optical Society of America Journal*, 69, 31
- Elson, J. M., Rahn, J. P., & Bennett, J. M. 1983, *AO*, 22, 3207
- Farihi, J., Becklin, E. E., & Zuckerman, B. 2003, in *IAU Symposium*, 289—+
- Fazio, G. G., Hora, J. L., Allen, L. E., Ashby, M. L. N., Barnby, P., Deutsch, L. K., Huang, J.-S., Kleiner, S., Marengo, M., Megeath, S. T., Melnick, G. J., Pahre, M. A., Patten, B. M., Polizotti, J., Smith, H. A., Taylor, R. S., Wang, Z., Willner, S. P., Hoffmann, W. F., Pipher, J. L., Forrest, W. J., McMurty, C. W., McCreight, C. R., McKelvey, M. E., McMurray, R. E., Koch, D. G., Moseley, S. H., Arendt, R. G., Mentzell, J. E., Marx, C. T., Losch, P., Mayman, P., Eichhorn, W., Krebs, D., Jhabvala, M., Gezari, D. Y., Fixsen, D. J., Flores, J., Shakoorzadeh, K., Jungo, R., Hakun, C., Workman, L., Karpati, G., Kichak, R., Whitley, R., Mann, S., Tollestrup, E. V., Eisenhardt, P., Stern, D., Gorjian, V., Bhattacharya, B., Carey, S., Nelson, B. O., Glaccum, W. J., Lacy, M., Lowrance, P. J., Laine, S., Reach, W. T., Stauffer, J. A., Surace, J. A., Wilson, G., Wright, E. L., Hoffman, A., Domingo, G., & Cohen, M. 2004, *ApJS*, 154, 10
- Finley, D. S., Koester, D., & Basri, G. 1997, *ApJ*, 488, 375
- Ford, E. B., Havlickova, M., & Rasio, F. A. 2001, *Icarus*, 150, 303
- Ford, K. E. S. & Neufeld, D. A. 2001, *ApJL*, 557, L113
- Forveille, T., Ségransan, D., Delorme, P., Martín, E. L., Delfosse, X., Acosta-Pulido, J. A., Beuzit, J.-L., Manchado, A., Mayor, M., Perrier, C., & Udry, S. 2004, *A&AS*, 427, L1
- Fraquelli, D. A., Schultz, A. B., Bushouse, H., Hart, H. M., & Vener, P. 2004, *Publ. Astron. Soc. Pac.*, 116, 55
- Friedrich, S., Zinnecker, H., Brandner, W., Correia, S., & McCaughrean, M. 2005, *ArXiv Astrophysics e-prints*
- Ge, J., Debes, J. H., Watson, A., & Chakraborty, A. 2002, in *Future Research Direction and Visions for Astronomy*. Edited by Dressler, Alan M. *Proceedings of the SPIE*, Volume 4835, pp. 87-97 (2002)., 87–97
- Ge, J. e. a. 2002, in *Future Research Direction and Visions for Astronomy*. Edited by Dressler, Alan M. *Proceedings of the SPIE*, Volume 4835, pp. 87-97 (2002)., 87–97

- Ge, J. e. a. 2003, in *Instrument Design and Performance for Optical/Infrared Ground-based Telescopes*. Edited by Iye, Masanori; Moorwood, Alan F. M. *Proceedings of the SPIE*, Volume 4841, pp. 1503-1514 (2003)., 1503–1514
- Gianninas, A., Dufour, P., & Bergeron, P. 2004, *ApJL*, 617, L57
- Gladman, B. 1993, *Icarus*, 106, 247
- Grady, C. A., Proffitt, C. R., Woodgate, B., Bowers, C. W., Heap, S. R., Kimble, R. A., Lindler, D., Plait, P., & Weinberger, A. 2003, *PASP*, 115, 1026
- Grady, C. A., Woodgate, B., Bruhweiler, F. C., Boggess, A., Plait, P., Lindler, D. J., Clampin, M., & Kalas, P. 1999, *ApJL*, 523, L151
- Graham, J. R., Matthews, K., Neugebauer, G., & Soifer, B. T. 1990, *ApJ*, 357, 216
- Green, P. J., Ali, B., & Napiwotzki, R. 2000, *ApJ*, 540, 992
- Griffin, R. E. M., David, M., & Verschueren, W. 2000, *A&ApS*, 147, 299
- Haas, M. & Leinert, C. 1990, *A&AS*, 230, 87
- Haisch, K. E., Lada, E. A., & Lada, C. J. 2001, *ApJL*, 553, L153
- Hansen, B. 2004, Personal Communication
- Hardy, J. W. 1998, *Adaptive optics for astronomical telescopes* (Oxford University Press)
- Hawley, S. L., Covey, K. R., Knapp, G. R., Golimowski, D. A., Fan, X., Anderson, S. F., Gunn, J. E., Harris, H. C., Ivezić, Ž., Long, G. M., Lupton, R. H., McGehee, P. M., Narayanan, V., Peng, E., Schlegel, D., Schneider, D. P., Spahn, E. Y., Strauss, M. A., Szkody, P., Tsvetanov, Z., Walkowicz, L. M., Brinkmann, J., Harvanek, M., Hennessy, G. S., Kleinman, S. J., Krzesinski, J., Long, D., Neilsen, E. H., Newman, P. R., Nitta, A., Snedden, S. A., & York, D. G. 2002, *AJ*, 123, 3409
- Henry, T. J., Kirkpatrick, J. D., & Simons, D. A. 1994, *AJ*, 108, 1437
- Hill, G. W. 1886, *Acta Mathematica*, 8, 1
- Holberg, J. B., Barstow, M. A., & Green, E. M. 1997, *ApJL*, 474, L127+
- Holberg, J. B., Bruhweiler, F. C., & Andersen, J. 1995, *ApJ*, 443, 753
- Holland, W. S., Greaves, J. S., Zuckerman, B., Webb, R. A., McCarthy, C., Coulson, I. M., Walther, D. M., Dent, W. R. F., Gear, W. K., & Robson, I. 1998, *Nature*, 392, 788
- Hutchings, J. B., Stoesz, J., Veran, J.-P., & Rigaut, F. 2004, *PASP*, 116, 154
- Ignace, R. 2001, *PASP*, 113, 1227
- Jacquinet, P. & Roizen-Dossier, B. 1964, *Progress in Optics*, 3, 31

- Jayawardhana, R., Fisher, S., Hartmann, L., Telesco, C., Pina, R., & Fazio, G. 1998, *ApJL*, 503, L79+
- Jeans, J. H. 1924, *MNRAS*, 85, 2
- Jones, H. R. A., Paul Butler, R., Marcy, G. W., Tinney, C. G., Penny, A. J., McCarthy, C., & Carter, B. D. 2002, *MNRAS*, 337, 1170
- Jura, M. 2003, *Astrophys. J.*, 584, L91
- Kalirai, J. S., Richer, H. B., Reitzel, D., Hansen, B. M. S., Rich, R. M., Fahlman, G. G., Gibson, B. K., & von Hippel, T. 2005, *ApJL*, 618, L123
- Kasdin, N. J., Vanderbei, R. J., Spergel, D. N., & Littman, M. G. 2003, *ApJ*, 582, 1147
- Kleinman, S. J., Nather, R. E., Winget, D. E., Clemens, J. C., Bradley, P. A., Kanaan, A., Provencal, J. L., Claver, C. F., Watson, T. K., Yanagida, K., Dixon, J. S., Wood, M. A., Sullivan, D. J., Meistas, E., Leibowitz, E. M., Moskalik, P., Zola, S., Pajdosz, G., Krzesinski, J., Solheim, J.-E., Bruvold, A., O'Donoghue, D., Katz, M., Vauclair, G., Dolez, N., Chevreton, M., Barstow, M. A., Kepler, S. O., Giovannini, O., Hansen, C. J., & Kawaler, S. D. 1994, *ApJ*, 436, 875
- Kleinman, S. J. e. a. 1998, *Astrophys. J.*, 495, 424
- Koester, D., Provencal, J., & Shipman, H. L. 1997, *A&AS*, 320, L57
- Kuchner, M. J., Koresko, C. D., & Brown, M. E. 1998, *ApJL*, 508, L81
- Kuchner, M. J. & Spergel, D. N. 2003a, in *ASP Conference Series 294, Scientific Frontiers In Research In Extrasolar Planets*, ed. D. Deming & S. Seager (2003)
- Kuchner, M. J. & Spergel, D. N. 2003b, *ApJ*, 594, 617
- . 2003c, *ApJ*, 594, 617
- Kuchner, M. J. & Traub, W. A. 2002, *ApJ*, 570, 900
- Lada, C. J. & Lada, E. A. 2003, *ARA&A*, 41, 57
- Lanning, H. H. 2000, *VizieR Online Data Catalog*, 2231, 0
- Laughlin, G. & Adams, F. C. 1999, *ApJ*, 526, 881
- Leggett, S. K., Allard, F., Geballe, T. R., Hauschildt, P. H., & Schweitzer, A. 2001, *ApJ*, 548, 908
- Lieber, M. D. e. a. 2003, in *Techniques and Instrumentation for Detection of Exoplanets*. Edited by Coulter, Daniel R. *Proceedings of the SPIE*, Volume 5170, pp. 66-78 (2003)., 66-78
- Liebert, J., Bergeron, P., & Holberg, J. B. 2004, *ArXiv Astrophysics e-prints*

- Lin, D. N. C. & Ida, S. 1997, *ApJ*, 477, 781+
- Livio, M., Pringle, J. E., & Saffer, R. A. 1992, *MNRAS*, 257, 15P
- Livio, M. & Soker, N. 1984, *MNRAS*, 208, 763
- Lyot, B. 1939, *MNRAS*, 99, 580
- Malbet, F. 1996, *A&ApS*, 115, 161
- Malbet, F., Yu, J. W., & Shao, M. 1995, *PASP*, 107, 386
- Marcy, G. W. & Butler, R. P. 2000, *PASP*, 112, 137
- McCarthy, C. & Zuckerman, B. 2004, *AJ*, 127, 2871
- McCarthy, D. W. e. a. 2001, *PASP*, 113, 353
- Melnick, G. J., Neufeld, D. A., Ford, K. E. S., Hollenbach, D. J., & Ashby, M. L. N. 2001, *Nature*, 412, 160
- Mohanty, S., Jayawardhana, R., & Basri, G. 2004, *ApJ*, 609, 885
- Murray, N. & Holman, M. 2001, *Nature*, 410, 773
- Murray, N., Paskowitz, M., & Holman, M. 2002, *ApJ*, 565, 608
- Nisenson, P. & Papaliolios, C. 2001, *ApJL*, 548, L201
- Oort, J. H. 1950, *BAIN*, 11, 91
- Paquette, C., Pelletier, C., Fontaine, G., & Michaud, G. 1986, *Astrophys. J. Suppl. Ser.*, 61, 197
- Parriott, J. & Alcock, C. 1998, *Astrophys. J.*, 501, 357
- Patterson, J., Zuckerman, B., Becklin, E. E., Tholen, D. J., & Hawarden, T. 1991, *ApJ*, 374, 330
- Pauli, E.-M., Napiwotzki, R., Altmann, M., Heber, U., Odenkirchen, M., & Kerber, F. 2003, *A&AS*, 400, 877
- Perryman, M. A. C., Lindegren, L., Kovalevsky, J., Hoeg, E., Bastian, U., Bernacca, P. L., Crézé, M., Donati, F., Grenon, M., van Leeuwen, F., van der Marel, H., Mignard, F., Murray, C. A., Le Poole, R. S., Schrijver, H., Turon, C., Arenou, F., Froeschlé, M., & Petersen, C. S. 1997, *A&AS*, 323, L49
- Pollack, J. B., Hubickyj, O., Bodenheimer, P., Lissauer, J. J., Podolak, M., & Greenzweig, Y. 1996, *Icarus*, 124, 62
- Press, W. H., Teukolsky, S. A., Vetterling, W. T., & Flannery, B. 1992, *Numerical Recipes in Fortran*, 2nd edn. (New York, New York: Cambridge University Press)

- Probst, R. G. & Oconnell, R. W. 1982, *ApJL*, 252, L69
- Quinlan, G. D. 1992, in *IAU Symp. 152: Chaos, Resonance, and Collective Dynamical Phenomena in the Solar System*, 25–+
- Rasio, F. A. & Ford, E. B. 1996, *Science*, 274, 954
- Rasio, F. A., Tout, C. A., Lubow, S. H., & Livio, M. 1996, *ApJ*, 470, 1187
- Riaud, P., Boccaletti, A., Rouan, D., Lemarquis, F., & Labeyrie, A. 2001, *PASP*, 113, 1145
- Rigaut, F., Salmon, D., Arsenault, R., Thomas, J., Lai, O., Rouan, D., Véran, J. P., Gigan, P., Crampton, D., Fletcher, J. M., Stilburn, J., Boyer, C., & Jagourel, P. 1998, *PASP*, 110, 152
- Rivera, E. J. & Lissauer, J. J. 2000, *ApJ*, 530, 454
- Roberts, L. C. & Neyman, C. R. 2002, *PASP*, 114, 1260
- Rouan, D., Riaud, P., Boccaletti, A., Clénet, Y., & Labeyrie, A. 2000, *PASP*, 112, 1479
- Sackmann, I.-J., Boothroyd, A. I., & Kraemer, K. E. 1993, *ApJ*, 418, 457
- Sato, B., Ando, H., Kambe, E., Takeda, Y., Izumiura, H., Masuda, S., Watanabe, E., Noguchi, K., Wada, S., Okada, N., Koyano, H., Maehara, H., Norimoto, Y., Okada, T., Shimizu, Y., Uruguchi, F., Yanagisawa, K., & Yoshida, M. 2003, *ApJL*, 597, L157
- Schneider, G. & Silverstone, M. D. 2003a, in *High-Contrast Imaging for Exo-Planet Detection*. Edited by Alfred B. Schultz. *Proceedings of the SPIE*, Volume 4860, pp. 1-9 (2003)., 1–9
- Schneider, G. & Silverstone, M. D. 2003b, in *High-Contrast Imaging for Exo-Planet Detection*. Edited by Alfred B. Schultz. *Proceedings of the SPIE*, Volume 4860, pp. 1-9 (2003)., 1–9
- Schröder, K. ., Winters, J. M., & Sedlmayr, E. 1999, *A&AS*, 349, 898
- Shu, F. H., Adams, F. C., & Lizano, S. 1987, *ARA&A*, 25, 23
- Siess, L. & Livio, M. 1999a, *MNRAS*, 304, 925
- . 1999b, *MNRAS*, 308, 1133
- Sigurdsson, S., Richer, H. B., Hansen, B. M., Stairs, I. H., & Thorsett, S. E. 2003, *Science*, 301, 193
- Sivaramakrishnan, A., Koresko, C. D., Makidon, R. B., Berkefeld, T., & Kuchner, M. J. 2001, *ApJ*, 552, 397
- Snellgrove, M. D., Papaloizou, J. C. B., & Nelson, R. P. 2001, *A&AS*, 374, 1092

- Soker, N. 2001, MNRAS, 324, 699
- Soker, N., Livio, M., & Harpaz, A. 1984, MNRAS, 210, 189
- Soummer, R., Aime, C., & Falloon, P. E. 2003a, A&AS, 397, 1161
- Soummer, R., Dohlen, K., & Aime, C. 2003b, A&AS, 403, 369
- Spergel, D. N. 2001, astro-ph/0101142
- Spergel, D. N., Verde, L., Peiris, H. V., Komatsu, E., Nolta, M. R., Bennett, C. L., Halpern, M., Hinshaw, G., Jarosik, N., Kogut, A., Limon, M., Meyer, S. S., Page, L., Tucker, G. S., Weiland, J. L., Wollack, E., & Wright, E. L. 2003, Astrophys. J. Suppl. Ser., 148, 175
- Stephens, D. C. & Leggett, S. K. 2004, PASP, 116, 9
- Stern, S. A., Shull, J. M., & Brandt, J. C. 1990, Nature, 345, 305
- Stoer, J. & Bulirsch, R. 1980, Introduction to Numerical Analysis (New York:Springer)
- Telesco, C. M., Joy, M., & Sisk, C. 1990, ApJL, 358, L17
- Tokunaga, A. T., Becklin, E. E., & Zuckerman, B. 1990, ApJL, 358, L21
- Tokunaga, A. T., Hodapp, K.-W., Becklin, E. E., Cruikshank, D. P., Rigler, M., Toomey, D., Brown, R. H., & Zuckerman, B. 1988, ApJL, 332, L71
- Tremaine, S. 1993, in ASP Conf. Ser. 36: Planets Around Pulsars, 335–344
- Trujillo, C. 2004, Personal communication
- van Altena, W. F., Lee, J. T., & Hoffleit, E. D. 2001, VizieR Online Data Catalog, 1238, 0
- Vanderbei, R. J., Spergel, D. N., & Kasdin, N. J. 2003, ApJ, 590, 593
- Vassiliadis, E. & Wood, P. R. 1993, ApJ, 413, 641
- Wachter, S., Hoard, D. W., Hansen, K. H., Wilcox, R. E., Taylor, H. M., & Finkelstein, S. L. 2003, ApJ, 586, 1356
- Weidemann, V. 2000, Astron. Astrophys., 363, 647
- Weidenschilling, S. J. & Marzari, F. 1996, Nature, 384, 619
- Weinberger, A. J., Becklin, E. E., Schneider, G., Smith, B. A., Lowrance, P. J., Silverstone, M. D., Zuckerman, B., & Terrile, R. J. 1999, ApJL, 525, L53
- Weissman, P. R. 1999, Space Science Reviews, 90, 301
- Wisdom, J. 1980, AJ, 85, 1122

- Wolszczan, A. & Frail, D. A. 1992, *Nature*, 355, 145
- Wood, M. A. 1992, *Astrophys. J.*, 386, 539
- Zhang, B. & Sigurdsson, S. 2003, *ApJL*, 596, L95
- Zuckerman, B. & Becklin, E. E. 1987, *Nature*, 330, 138
- . 1992, *ApJ*, 386, 260
- Zuckerman, B., Koester, D., Reid, I. N., & Hüensch, M. 2003, *Astrophys. J.*, 596, 477
- Zuckerman, B. & Reid, I. N. 1998, *ApJL*, 505, L143

Vita

John H. Debes, IV

Pennsylvania State University
Department of Astronomy & Astrophysics
525 Davey Lab
University Park, PA 16802
(814)865-8484
debes@astro.psu.edu

Education:

Ph. D. Astronomy, Pennsylvania State University, expected August 2005 Thesis *Digging in the Stellar Graveyard for Substellar Objects* Advisor: Prof. Steinn Sigurdsson
B.A., Physics with Honors, Johns Hopkins University, 1999

Proposals and Awards:

PI, Spitzer Cycle 1 Program 3655, Award amount: \$38,000
PI, HST Cycle 12 Program 9834, Award amount: \$54,642
PI, NOAO Gemini Program GN-2005A-Q-69
PI, NOAO Gemini Program GN-2004B-DD-9
PI, HET Programs PSU03-3-038, PSU04-2-010
Co-I, CFHT Programs 2003B-H42A, 2004A-H59A, 2004B-H53A
SPIE Scholarship Award, Award amount: \$2,500 2003-2004
NASA Graduate Student Research Program fellow 2001-2004

Refereed Papers:

Debes, J. H., Sigurdsson, S., & Woodgate, B., Limits to Extrasolar Planets Around Nearby DAZ White Dwarfs, AJ, in press
Debes, J. H., Sigurdsson, S., & Woodgate, B., Limits to Extrasolar Planets Around G 29-38, submitted to ApJ
Debes, J. H. & Ge, J., High-Contrast Imaging with Gaussian Aperture Pupil Masks, 2004 PASP 116 674
Debes, J. H., Ge, J., Kuchner, M., Rogosky, M., Using Notch-Filter Masks for High Contrast Imaging of Extrasolar Planets, 2004 ApJ 608 1095
Chakraborty, A., Ge, J. & Debes, J. H., Nature of Companions of G Type Stars Using Adaptive Optics 2002 AJ 124 1127
Debes, J. H., Ge, J. & Chakraborty, A., First High Contrast Imaging Using a Gaussian Aperture Pupil Mask, 2002 ApJ 572 L165
Debes, J. H. & Sigurdsson, S., Are There Unstable Planetary Systems Around White Dwarfs?, 2002 ApJ 572 556